

UNIVERSITY OF OKLAHOMA
GRADUATE COLLEGE

FLOW OF POWER-LAW FLUID IN A PARTIALLY BLOCKED ECCENTRIC
ANNULUS

A THESIS
SUBMITTED TO THE GRADUATE FACULTY
in partial fulfillment of the requirements for the
Degree of
MASTER OF SCIENCE IN NATURAL GAS ENGINEERING AND
MANAGEMENT

By
SILVIA CAROLINA ROJAS TINEO
Norman, Oklahoma
2016

FLOW OF POWER-LAW FLUID IN A PARTIALLY BLOCKED ECCENTRIC
ANNULUS

A THESIS APPROVED FOR THE
MEWBOURNE SCHOOL OF PETROLEUM AND GEOLOGICAL ENGINEERING

BY

Dr. Ramadan Ahmed, Chair

Dr. Catalin Teodoriu

Dr. Maysam Pournik

© Copyright by SILVIA CAROLINA ROJAS TINEO 2016
All Rights Reserved.

The present thesis is dedicated to my parents Francisco Rojas and Petra Tineo for their love, understanding and unconditional support. Also, it is dedicated to my aunt Olga Rojas, my siblings Judith and Francisco, my cousin Cecilia Rojas, the rest of my family and my closest friends who accompanied me through this experience.

To God, with him, everything is possible...

Acknowledgements

I would like to express my gratitude to my advisor, Dr. Ramadan Ahmed, for his support, patience, encouragement and guidance to successfully complete this work. Special thanks to Dr. Catalin Teodoriu and Dr. Maysam Pournik, for their advice and for being part of my thesis committee.

I also would like to express my sincere thanks to Dr. Ming Tang for his guidance and his technical support during the simulation studies.

Special thanks to the Director of the Natural Gas Engineering and Management program, Dr. Suresh Sharma for his guidance throughout my study in the program.

Table of Contents

Acknowledgements	iv
Table of Contents	v
List of Tables	ix
List of Figures.....	x
Abstract.....	xvii
Chapter 1. Introduction.....	1
1.1 Overview	1
1.2 Problem Description.....	3
1.3 Objectives	5
1.4 Scope of Work and Methodology.....	5
1.5 Outline	6
Chapter 2. Literature Review	7
2.1 Concentric Annulus	7
2.2 Eccentric Annulus	9
2.2.1 Analytical Studies.....	11
2.2.2 Numerical Studies	14
2.2.3 Modeling Studies.....	15

2.2.4 Experimental Studies	17
2.3 Partial Blocked Annulus	17
2.3.1 Numerical studies	18
2.3.2 Experimental Studies	19
2.4 Computational Fluid Dynamics (CFD)	19
Chapter 3. Basic Theory of Laminar Flow	22
3.1 Rheological Models and Relevant Hydraulic Parameters	22
3.2 Pipe Flow	27
3.3 Concentric Annular Flow	29
3.4 Eccentric Annular Flow	31
3.5 Flow in Partially Blocked Annulus	34
Chapter 4. Computational Fluid Dynamics (CFD).....	36
4.1 Governing Equations	37
4.2 Grid System and Sensitivity	39
4.3 CFD Simulation.....	44
4.3.1 Set up and Post-Processing.....	44
4.3.2 Matrix	47
4.3.3 CFD Verification	48
4.3.4 Hydraulic and Geometric Parameters Sensitivity Analysis.....	50
Chapter 5. Results and Discussion	55

5.1 Numerical Verification	55
5.1.1 Comparison of CFD Simulation with Experimental Data.....	55
5.1.2 Comparison of CFD Model with Analytical and Numerical Solutions	56
5.2 Effect of Cutting Build Up within the Annulus.....	59
5.2.1 Annular Frictional Pressure Loss	60
5.2.2 Axial Velocity Profiles	62
5.2.3 Hydraulic Parameter fRe	64
5.2.4 Wall Shear Stress.....	69
5.2.5 Bed Shear Stress	71
5.3 Development of New Correlations.....	78
5.3.1 Hydraulic Parameter fRe	79
5.3.2 Bed Shear Stress	87
Chapter 6. Conclusions and Recommendations	89
6.1 Conclusions	89
6.2 Recommendations	90
References	91
Appendix A: Nomenclature.....	100
Appendix B: Additional Derivations.....	106
Appendix C: Additional Simulation Matrices	109

Appendix D: Hydraulic Diameter Calculation and Existing Correlation Model for PL Fluid in Concentric Annulus with Cuttings Bed	110
Appendix E: Bed Shear Stress and Velocity Profiles.....	114

List of Tables

Table 2.1 Hydraulic parameter (fRe) for power-law fluids (Fang et al., 1999).....	15
Table 2.2 Coefficients used in Eq. (3-16) (Ahmed et al., 2006)	17
Table 4.1. Input parameters for grid size sensitivity analysis	41
Table 4.2 Mesh metrics for unstructured meshes (100% H_{bed} and $\kappa =0.5$).....	44
Table 4.3 Results obtained using unstructured cutcell meshing.....	44
Table 4.4 Matrix simulation. Diameter ratio 0.75	47
Table 4.5 Volumetric flow rate and stationary bed height	49
Table 4.6 Modified non-Newtonian power law density and rheological parameters.....	49
Table 4.7 Input parameters used in sensitivity analysis	50
Table 5.1 Regression coefficient parameters developed ($e=0.9$)	82
Table 5.2 Numerical validation based on pressure drop values ($e=0.9$)	83
Table B.1 Regression coefficient parameters (Aworunse, 2012).....	108
Table C.1 Matrix simulation. Diameter ratio 0.75	109
Table C.2 Matrix simulation. Diameter ratio 0.25	109

List of Figures

Figure 1.1 Concentric and eccentric annular geometries	2
Figure 1.2 Partially eccentric annulus	3
Figure 1.3 Partially blocked eccentric annulus.....	4
Figure 2.1 Slot equivalent of: (a) concentric; and (b) eccentric annuli (Haciislamoglu, 1989).....	9
Figure 2.2 Eccentric annulus in bipolar coordinates (Haciislamoglu, 1989)	13
Figure 2.3 Wellbore cross section with cuttings bed.....	19
Figure 3.1 Time-independent non-Newtonian fluid types (redrawn from Nguyen et al., 2012).....	23
Figure 3.2 Viscosity of Newtonian, shear thinning and shear thickening as a function of shear rate. (Willenbacher and Georgieva, 2013)	24
Figure 3.3 Laminar vs. turbulent flow in pipe flow. (Schlichting, 2000).....	25
Figure 3.4 Laminar velocity profile in a circular pipe flow	27
Figure 3.5 Velocity and wall shear stress profile for laminar flow- narrow slot-power - law fluids (Bourgoyne et al., 1986)	30
Figure 3.6 Velocity profile of Newtonian laminar flow in concentric annulus (Bourgoyne et al., 1986).....	30
Figure 3.7 Velocity profile for laminar flow in eccentric annulus flow (Ebrahim et al., 2013).....	32
Figure 3.8 Shape factor vs. $1/n$ for eccentric annulus with diameter ratio of 0.2 (Ahmed et al., 2006)	33
Figure 3.9 Eccentric annulus with cuttings bed geometry	34

Figure 4.1 Hexahedral mesh: (a) $\kappa=0.75$; (b) $\kappa=0.5$; and (c) $\kappa=0.25$ ($e=0.9$, $H_{bed}=10\%$)	40
Figure 4.2 Unstructured meshes: (a) tetrahedral with boundary layers; and (b) cutcells ($\kappa=0.5$, $e=0.9$)	40
Figure 4.3 Grid size independency of pressure drop. Structured mesh	42
Figure 4.4 Grid size independency of fRe . Structured mesh	42
Figure 4.5 Grid size independency of Π_{bed} . Structured mesh	43
Figure 4.6 Pressure gradient and axial velocity along a partially blocked eccentric annulus ($e=0.9$, $\kappa=0.5$, $n=1$, $H_{bed}=10\%$, $Q = 5 \times 10^{-5} \text{ m}^3/\text{s}$)	46
Figure 4.7 X and Y dimensionless coordinates	48
Figure 4.8 fRe vs. fluid consistency index ($H_{bed} = 10\%$, $Q=1 \times 10^{-4} \text{ m}^3/\text{s}$)	51
Figure 4.9 Π_{bed} vs. fluid consistency index ($H_{bed}=10\%$, $Q=1 \times 10^{-4} \text{ m}^3/\text{s}$)	52
Figure 4.10 Hydraulic parameters: (a) fRe vs. avg. velocity; (b) fRe vs. Re ; (c) Π_{bed} vs. avg. velocity; and (d) Π_{bed} vs. Re	54
Figure 5.1 Measured and CFD predicted pressure gradients vs. flowrate (SBM Fluid, data from George 2012)	56
Figure 5.2 Comparison of predictions of CFD simulation and analytical model for dimensionless eccentricity of 0.9 ($Q = 5 \times 10^{-5} \text{ m}^3/\text{s}$)	57
Figure 5.3 Hydraulic parameter fRe vs. n for $\kappa=0.75$, $e=0.9$, and $Q = 5 \times 10^{-5} \text{ m}^3/\text{s}$	58
Figure 5.4 Hydraulic parameter fRe vs. n for $\kappa=0.50$, $e=0.9$, and $Q = 5 \times 10^{-5} \text{ m}^3/\text{s}$	58
Figure 5.5 Hydraulic parameter fRe vs. n for $\kappa=0.25$, $e=0.9$, and $Q = 5 \times 10^{-5} \text{ m}^3/\text{s}$	59
Figure 5.6 Pressure loss vs. % dimensionless bed height ($\kappa=0.75$, $e=0.9$ and $Q = 5 \times 10^{-5} \text{ m}^3/\text{s}$)	60

Figure 5.7 Pressure loss vs. % dimensionless bed height ($\kappa=0.50$, $e=0.9$ and $Q = 5 \times 10^{-5}$ m^3/s).....	61
Figure 5.8 Pressure loss vs. % dimensionless bed height ($\kappa=0.25$, $e=0.9$ and $Q = 5 \times 10^{-5}$ m^3/s).....	61
Figure 5.9 Velocity distributions in partially blocked annuli ($n=1$, $\kappa=0.50$, $e=0.9$ and $Q = 5 \times 10^{-5}$ m^3/s): (a) $H_{bed}=0\%$; (b) $H_{bed}=30\%$; (c) $H_{bed}=70\%$; and (d) $H_{bed}=100\%$	63
Figure 5.10 Velocity profile vs. Y ($H_{bed}=30\%$, $\kappa=0.75$, $e=0.9$ and $Q = 5 \times 10^{-5}$ m^3/s)	64
Figure 5.11 fRe vs. % bed height ($e=0.9$, $\kappa = 0.75$ and $Q = 5 \times 10^{-5}$ m^3/s)	66
Figure 5.12 fRe vs. % bed height ($e=0.9$, $\kappa = 0.5$ and $Q = 5 \times 10^{-5}$ m^3/s)	66
Figure 5.13 fRe vs. % bed height ($e=0.9$, $\kappa = 0.25$ and $Q = 5 \times 10^{-5}$ m^3/s)	67
Figure 5.14 Axial velocity profiles vs. Y ($\kappa = 0.25$, $e=0.9$ and $Q = 5 \times 10^{-5}$ m^3/s): (a) 0% H_{bed} ; and (b) $10\% H_{bed}$	68
Figure 5.15 fRe vs. % H_{bed} : $Q_1= 1 \times 10^{-5}$ m^3/s ; $Q_2= 1 \times 10^{-4}$ m^3/s ($e=0.9$, and $\kappa = 0.5$)....	69
Figure 5.16 τ_w vs. % H_{bed} ($e=0.9$, $\kappa = 0.75$, $Q= 1 \times 10^{-5}$ m^3/s).....	70
Figure 5.17 τ_w vs. % H_{bed} ($e=0.9$, $\kappa = 0.5$, $Q= 1 \times 10^{-5}$ m^3/s).....	70
Figure 5.18 τ_w vs. % H_{bed} ($e=0.9$, $\kappa = 0.25$, $Q= 1 \times 10^{-5}$ m^3/s).....	71
Figure 5.19 τ_{bed} vs. X ($e=0.9$, $\kappa=0.5$ and $Q= 5 \times 10^{-5}$ m^3/s): (a) $H_{bed} = 10\%$; and (b) $H_{bed}=100\%$	72
Figure 5.20 Shear stress distribution on cuttings bed surface, $H_{bed}= 50\%$ ($e = 0.9$, $\kappa = 0.5$, and $Q = 5 \times 10^{-5}$ m^3/s).....	73
Figure 5.21 τ_{bed} vs. % H_{bed} ($e=0.9$, $\kappa=0.75$ and $Q = 5 \times 10^{-5}$ m^3/s).....	74
Figure 5.22 τ_{bed} vs. % H_{bed} ($e=0.9$, $\kappa = 0.50$ and $Q = 5 \times 10^{-5}$ m^3/s).....	74
Figure 5.23 τ_{bed} vs. % H_{bed} ($e=0.9$, $\kappa = 0.25$ and $Q = 5 \times 10^{-5}$ m^3/s).....	75

Figure 5.24 Π_{bed} vs. % H_{bed} ($e=0.9$, $\kappa=0.75$ and $Q = 5 \times 10^{-5} \text{ m}^3/\text{s}$)	76
Figure 5.25 Π_{bed} vs. % H_{bed} ($e=0.9$, $\kappa=0.5$ and $Q = 5 \times 10^{-5} \text{ m}^3/\text{s}$)	76
Figure 5.26 Π_{bed} vs. % H_{bed} ($e=0.9$, $\kappa=0.25$ and $Q = 5 \times 10^{-5} \text{ m}^3/\text{s}$)	77
Figure 5.27 Π_{bed} vs. % H_{bed} : a) $Q_1= 1 \times 10^{-5} \text{ m}^3/\text{s}$; b) $Q_2= 1 \times 10^{-4} \text{ m}^3/\text{s}$ ($e=0.9$, $\kappa=0.5$) ..	78
Figure 5.28 Shape Factor vs. $1/n$ ($e=0.9$). Trendline for different bed heights ($\kappa=0.5$)	79
Figure 5.29 Parameter “ a ” vs. dimensionless bed height ($e=0.9$) for different κ values	80
Figure 5.30 Parameter “ b ” vs. dimensionless bed height ($e=0.9$) for different κ values	81
Figure 5.31 fRe Correlation vs. fRe CFD ($e=0.9$)	82
Figure 5.32 fRe Exlog Solution (Chen, 2005) vs. fRe CFD	84
Figure 5.33 fRe Exlog solution modified 1 (Chen 2005; correction factor by Hacıislamoglu and Langlinais, 1990) vs. fRe CFD	85
Figure 5.34 fRe Exlog Solution modified 2 (Chen, 2005; correction factor by Ahmed et al., 2006) vs. fRe CFD	86
Figure 5.35 fRe Aworunse’s model (Aworunse, 2012) vs. fRe CFD	87
Figure 5.36 Π_{bed} computed from correlation and CFD data	88
Figure D.1 Geometrical analysis (Chen, 2005)	110
Figure E.1 τ_{bed} vs. X . a) $H_{bed}=10\%$; b) $H_{bed} = 30\%$; c) $H_{bed} = 50\%$; d) $H_{bed} = 70\%$; e) $H_{bed}= 90\%$; f) $H_{bed} =100\%$ ($e=0.9$, $\kappa=0.25$)	114
Figure E.2 τ_{bed} vs. X . a) $H_{bed}=10\%$; b) $H_{bed} = 30\%$; c) $H_{bed} = 50\%$; d) $H_{bed} = 70\%$; e) $H_{bed}= 90\%$; f) $H_{bed} =100\%$ ($e=0.9$, $\kappa=0.50$)	115
Figure E.3 τ_{bed} vs. X . a) $H_{bed}=10\%$; b) $H_{bed} = 30\%$; c) $H_{bed} = 50\%$; d) $H_{bed} = 70\%$; e) $H_{bed}= 90\%$; f) $H_{bed} =100\%$ ($e=0.9$, $\kappa=0.75$)	116
Figure E.4 Axial velocity vs. Y . a) $H_{bed}= 0\%$ ($e=0.90$, $\kappa=0.25$)	117

Figure E.5 Axial velocity vs. Y . a) $H_{bed} = 10\%$ ($e=0.9, \kappa=0.25$)	117
Figure E.6 Axial velocity vs. Y . a) $H_{bed} = 30\%$; b) $H_{bed} = 50\%$; c) $H_{bed} = 70\%$; d) $H_{bed} = 90\%$; e) $H_{bed} = 100\%$ ($e=0.9, \kappa=0.25$)	118
Figure E.7 Axial velocity vs. Y . a) $H_{bed} = 0$ ($e=0.9, \kappa=0.50$)	119
Figure E.8 Axial velocity vs. Y . a) $H_{bed} = 10\%$; b) $H_{bed} = 30\%$; c) $H_{bed} = 50\%$; d) $H_{bed} = 70\%$; e) $H_{bed} = 90\%$; f) $H_{bed} = 100\%$ ($e=0.9, \kappa=0.50$)	120
Figure E.9 Axial velocity vs. Y . a) $H_{bed} = 0\%$ ($e=0.9, \kappa=0.75$)	121
Figure E.10 Axial velocity vs. Y . a) $H_{bed} = 10\%$; b) $H_{bed} = 30\%$; c) $H_{bed} = 50\%$; d) $H_{bed} = 70\%$; e) $H_{bed} = 90\%$; f) $H_{bed} = 100\%$ ($e=0.9, \kappa=0.75$)	122
Figure E.11 Velocity Contour: a) $n=1$; b) $n=0.8$; c) $n=0.6$; d) $n=0.4$; e) $n=0.2$ ($e=0.9, H_{bed}=0\%$, $\kappa=0.25$)	123
Figure E.12 Velocity contour: a) $H_{bed} = 10\%$; b) $H_{bed} = 30\%$; c) $H_{bed} = 50\%$; d) $H_{bed} = 70\%$; e) $H_{bed} = 90\%$; f) $H_{bed} = 100\%$ ($e=0.9, n=1, \kappa=0.25$)	124
Figure E.13 Velocity contour: a) $H_{bed}=10\%$; b) $H_{bed}= 30\%$; c) $H_{bed} = 50\%$; d) $H_{bed} = 70\%$; e) $H_{bed} = 90\%$; f) $H_{bed} = 100\%$ ($e=0.9, n=0.8, \kappa=0.25$)	125
Figure E.14 Velocity contour: a) $H_{bed}=10\%$; b) $H_{bed}= 30\%$; c) $H_{bed} = 50\%$; d) $H_{bed}= 70\%$; e) $H_{bed} = 90\%$; f) $H_{bed}=100\%$ ($e=0.9, n=0.6, \kappa=0.25$)	126
Figure E.15 Velocity contour: a) $H_{bed} = 10\%$; b) $H_{bed}= 30\%$; c) $H_{bed} = 50\%$; d) $H_{bed} = 70\%$; e) $H_{bed}= 90\%$; f) $H_{bed} = 100\%$ ($e=0.9, n=0.4, \kappa=0.25$)	127
Figure E.16 Velocity contour: a) $H_{bed} = 10\%$; b) $H_{bed}= 30\%$; c) $H_{bed} = 50\%$; d) $H_{bed} = 70\%$; e) $H_{bed} = 90\%$; f) $H_{bed} = 100\%$ ($e=0.9, n=0.2, \kappa=0.25$)	128
Figure E.17 Velocity Contour: a) $n=1$; b) $n=0.8$; c) $n=0.6$; d) $n=0.4$; e) $n=0.2$ ($e=0.9, H_{bed} = 0\%$, $\kappa=0.5$)	129

Figure E.18 Velocity Contour: a) $H_{bed}=10\%$; b) $H_{bed} = 30\%$; c) $H_{bed} = 50\%$; d) $H_{bed} = 70\%$; e) $H_{bed}= 90\%$; f) $H_{bed} =100\%$ ($e=0.9, n=1, \kappa=0.5$).....	130
Figure E.19 Velocity Contour: a) $H_{bed} =10\%$; b) $H_{bed} = 30\%$; c) $H_{bed} = 50\%$; d) $H_{bed} = 70\%$; e) $H_{bed}= 90\%$; f) $H_{bed} =100\%$ ($e=0.9, n=0.8, \kappa=0.5$).....	131
Figure E.20 Velocity Contour: a) $H_{bed} =10\%$; b) $H_{bed} = 30\%$; c) $H_{bed} = 50\%$; d) $H_{bed} = 70\%$; e) $H_{bed} = 90\%$; f) $H_{bed} =100\%$ ($e=0.9, n=0.6, \kappa=0.5$).....	132
Figure E.21 Velocity Contour: a) $H_{bed} =10\%$; b) $H_{bed} = 30\%$; c) $H_{bed}= 50\%$; d) $H_{bed} = 70\%$; e) $H_{bed} = 90\%$; f) $H_{bed} =100\%$ ($e=0.9, n=0.4, \kappa=0.5$).....	133
Figure E.22 Velocity Contour: a) $H_{bed}=10\%$; b) $H_{bed} = 30\%$; c) $H_{bed} = 50\%$; d) $H_{bed} = 70\%$; e) $H_{bed} = 90\%$; f) $H_{bed} =100\%$ ($e=0.9, n=0.2, \kappa=0.5$).....	134
Figure E.23 Velocity Contour: a) $n=1$; b) $n =0.8$; c) $n =0.6$; d) $n=0.4$; e) $n=0.2$ ($e=0.9, H_{bed} = 0\%$, $\kappa =0.75$)	135
Figure E.24 Velocity Contour: a) $H_{bed} =10\%$; b) $H_{bed} = 30\%$; c) $H_{bed} = 50\%$; d) $H_{bed} = 70\%$; e) $H_{bed} = 90\%$; f) $H_{bed} =100\%$ ($e=0.9, n=1, \kappa =0.75$).....	136
Figure E.25 Velocity Contour: a) $H_{bed} =10\%$; b) $H_{bed} = 30\%$; c) $H_{bed} = 50\%$; d) $H_{bed} = 70\%$; e) $H_{bed}= 90\%$; f) $H_{bed} =100\%$ ($e=0.9, n=0.8, \kappa =0.75$).....	137
Figure E.26 Velocity Contour: a) $H_{bed} =10\%$; b) $H_{bed} = 30\%$; c) $H_{bed} = 50\%$; d) $H_{bed} = 70\%$; e) $H_{bed} = 90\%$; f) $H_{bed} =100\%$ ($e=0.9, n=0.6, \kappa =0.75$).....	138
Figure E.27 Velocity Contour: a) $H_{bed} =10\%$; b) $H_{bed} = 30\%$; c) $H_{bed} = 50\%$; d) $H_{bed} = 70\%$; e) $H_{bed} = 90\%$; f) $H_{bed} =100\%$ ($e=0.9, n=0.4, \kappa =0.75$).....	139
Figure E.28 Velocity Contour: a)) $H_{bed} =10\%$; b) $H_{bed} = 30\%$; c) $H_{bed} = 50\%$; d) $H_{bed}= 70\%$; e) $H_{bed}= 90\%$; f) $H_{bed} =100\%$ ($e=0.9, n=0.2, \kappa =0.75$).....	140
Figure E.29 Shape Factor vs. $1/n$ ($e=0.9$) for different bed heights ($\kappa=0.75$)	141

Figure E.30 Shape Factor vs. $1/n$ ($e=0.9$) for different bed heights ($\kappa=0.25$) 142

Abstract

Directional drilling has been increased recently due to its multiple benefits when compared to conventional drilling. Among several advantages, the increase in the production of oil and gas through the use of multiple wells from a single vertical wellbore is the most significant one. However, there is a tendency of the drill pipe to rest on the low-side of the annulus due to gravity. Moreover, vertical component of annular fluid velocity is reduced resulting in accumulation of cuttings on the low side of the wellbore. With reduced vertical component, suspended cuttings in the annulus can settle and ultimately form a uniform cuttings bed, which partially blocks the flow and creates hydraulic resistance. Consequently, bottom hole pressure is affected by this phenomenon and drilling operation performance can be significantly reduced.

Numerous wellbore hydraulic studies (Haciislamoglu and Langlinais, 1989; Fang et al., 1999; and Escudier et al., 2002) have been conducted to predict annular pressure loss in eccentric annulus. However, very limited studies (Hussain and Sharif, 1998; and Azouz et al., 1993) have been conducted on fluid flow in partially blocked annular geometries. The aim of this research is to perform numerical simulation-based investigation to analyze the effect of cuttings bed formation on annular pressure loss in a partially blocked eccentric annulus under laminar flow condition. A Computational Fluid Dynamics (CFD) software (ANSYS FLUENT) is used to conduct numerical simulation studies through the use of a finite element algorithm for solving the governing equations of motion in such complex annular geometries with blockage. The simulation studies were conducted for power law fluid flowing in highly eccentric annulus (i.e. 90% eccentricity). Effects of fluid rheological properties (fluid behavior index and

consistency index) and flow geometry (diameter ratio, and cuttings bed height) on velocity profile, frictional pressure loss and bed and wall shear stresses are investigated. Due to the presence of tool joints and wellbore irregularities, drillstring is expected to have approximately 90% eccentricity. In addition, for eccentricity more than 90%, simulation studies become very difficult and computationally intensive due to numerical instability.

Pressure losses predicted using CFD were evaluated by comparing them with results of published studies and experimental measurements obtained from a partially blocked eccentric annulus. A good agreement is obtained with CFD predictions and results of published studies and experimental measurements. For Newtonian fluids, CFD results for cases without cutting beds were validated using analytical solution.

After proper validation, simulation results were used to develop approximate correlations for friction factor and bed shear stress. The new friction factor correlation provides reasonable prediction with a maximum discrepancy of $\pm 5\%$. The new bed shear stress correlation exhibits slightly higher discrepancy ($\pm 10\%$). As anticipated, the annular frictional pressure loss increased with cuttings bed at a constant flowrate. It was also observed that with greater shear thinning behavior, the lower is the impact of cuttings bed on the annular pressure loss.

Chapter 1. Introduction

1.1 Overview

Accurate frictional pressure drop predictions and proper analysis of fluid flow in a wellbore are important for optimization of drilling operation. Moreover, the models developed in this study can be applied to other industrial applications such as chemical, petrochemical, and food processing industries.

During drilling operations, the bottomhole pressure of a well is maintained slightly above the pore pressure to prevent flow of formation fluid influx into the wellbore. Inaccurate predictions of friction pressure loss can cause inappropriate engineering decisions, which may produce further drilling problems, such as: loss of circulation fluid, kicks, and stuck-pipe. Therefore, a study on the wellbore hydraulic becomes crucial to analyze fluid flow in the wellbore and accurately predict bottom hole pressure and equivalent circulation density (ECD).

In addition to rheological properties of drilling fluid (i.e. pseudoplastic, thixotropic, and viscoelastic effects), different wellbore parameters such as well geometry (diameter ratio and eccentricity), drill pipe rotation speed, axial fluid velocity, and concentration of cuttings, influence the flow behavior in the wellbore. Theoretical, numerical, and experimental studies have been extensively conducted on annular fluid flow. Early studies assumed Newtonian fluid in concentric annular geometry between drill pipe and hole. However, wellbores can exhibit eccentric geometry, especially in inclined wells, where there is a strong tendency for the inner pipe to settle down to the low-side of the wellbore (Figure 1.1). It has been observed through experiments and

numerical simulation studies that eccentricity can significantly decrease (up to 50%) annular pressure loss (Mitsubishi and Aoyagi, 1973; Silva and Shah, 2000; and Zamora et al., 2005).

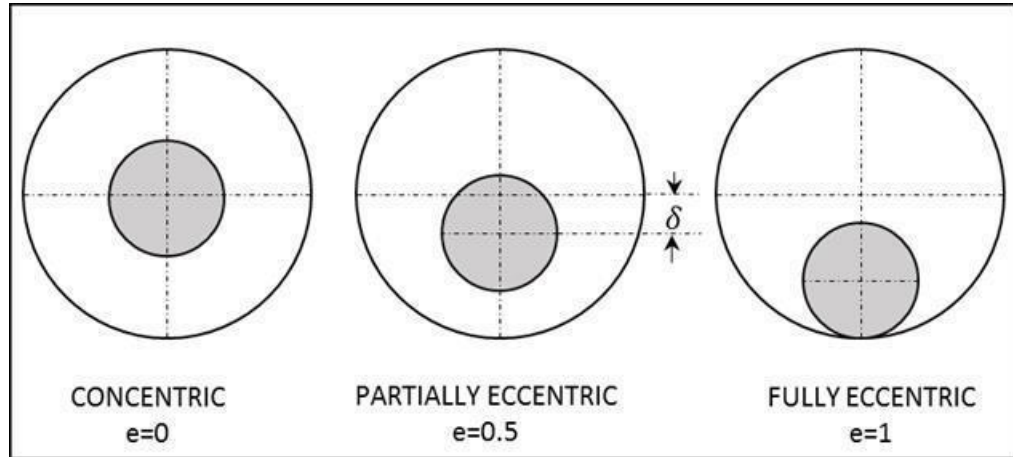


Figure 1.1 Concentric and eccentric annular geometries

The annular eccentricity is of great importance for hydraulic analysis. It is often defined in dimensionless form as:

$$e = \frac{\delta}{(R_o - R_i)} \quad (1-1)$$

where R_o and R_i correspond to outer and inner radii, respectively (Fig. 1.2), while δ is the center-to-center distance between the two cylinders. The dimensionless eccentricity is zero for a concentric annulus, and it is one for a fully eccentric annulus. Typical diameter ratio of wellbores ranges from 0.3 to 0.7. However, for special drilling applications, such as slim-hole drilling, casing drilling, and coiled tubing operations, diameter ratios can be out of this range.

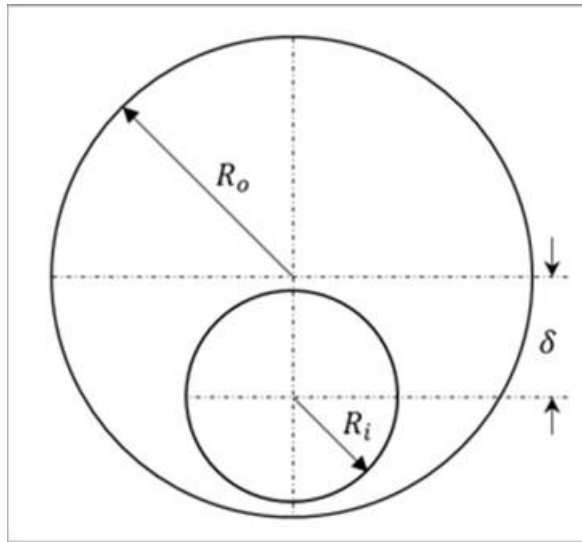


Figure 1.2 Partially eccentric annulus

1.2 Problem Description

During directional drilling operations, rock cuttings that accumulate on the low side of the annulus due to the gravity are always difficult to remove. Poor hole cleaning may cause a number of drilling problems such as increase in drillstring torque and drag, fluid loss, lost circulation and stuck pipe. These problems often result in loss of productive time and subsequently increase the operational cost.

Fluid velocity and rheology are controllable parameters to achieve satisfactory wellbore cleaning. The velocity of the fluid has a significant effect on hole cleaning due to its positive relationship with cuttings bed shear stress. However, excessive annular fluid velocity, results in high ECD and borehole erosion. Since rock cuttings generated at the drill bit must be removed from the bottom hole, a proper management of the wellbore hydraulic is required in order to guarantee an efficient hole cleaning.

A number of studies (George, 2012; Elgaddafi, 2010; George et al., 2014) showed that cuttings bed formation in directional wells is the most common operational problem confronting drillers in. When the critical state of clogging of the well is reached, a flow restriction within the annulus occurs (Figure 1.3) which affects the friction factor and results in increased annular pressure loss. Thus, the study of the annular flow becomes very important in a partially obstructed annulus.

Very limited studies (Aworunse 2012; Tang et al. 2016; and Bicalho et al. 2016) have been conducted on the effect of blockage on annular pressure loss. The formation of cuttings bed in the annulus complicates flow geometry; as a result, analytical solution cannot be obtained. Thus, numerical methods are often applied to predict pressure loss and bed shear stress in a partially blocked annulus. Previous studies (Azouz et al., 1993; Hussain et al., 1998) developed extensive and time consuming numerical procedures to predict pressure loss in a partially blocked annulus. Currently, with the use of Computational Fluid Dynamic (CFD) software, it is possible to develop very efficient numerical models for complex flow problems.

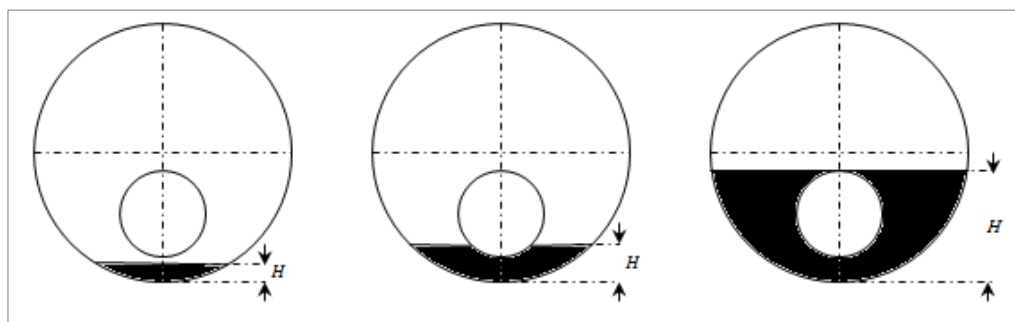


Figure 1.3 Partially blocked eccentric annulus

1.3 Objectives

The main objective of this study is to better understand non-Newtonian fluid flow in partially blocked annulus, that take place in horizontal or inclined wellbores. The study is conducted using commercial CFD software (ANSYS FLUENT). The analysis was carried out for laminar flow of power law fluid in a partially blocked highly eccentric annulus. Hence, this study is aimed at:

- Investigating the effect of cuttings bed build up on the annular friction pressure loss, and hydraulic parameters such as dimensionless hydraulic resistance (fRe) and wall shear stress.
- Studying effects of rheological fluid properties (power law index), diameter ratio and cuttings bed height on annular pressure loss and bed shear stress.
- Developing simple and approximate models to predict the friction pressure loss and bed shear stress.

1.4 Scope of Work and Methodology

This research involves CFD-based investigation, theoretical study, and correlations development. In the CFD study, horizontal annular section of a wellbore is simulated considering laminar flow conditions. Extensive CFD simulations were carried out considering power-law fluids. Effects of cuttings bed height, diameter ratio, and power law exponent (n) on pressure loss and bed shear stress were investigated. Moreover, to verify the accuracy of CFD model predictions, simulation results were validated using existing experimental measurements. For unblocked annulus, validation was conducted using published numerical results and analytical solutions (only for

Newtonian fluids). Based on CFD simulation results, simplified dimensionless correlations have been developed to predict annular pressure loss and bed shear stress.

1.5 Outline

This thesis consists of six chapters. Chapter 1 describes statement of the problem, objectives and research methodologies. Chapter 2 presents a comprehensive review of theoretical and experimental studies on annular flow of power-law fluids. In addition, it presents review of most recent CFD based studies conducted on non-Newtonian flows in partially blocked annuli. Chapter 3 covers basic theory of pipe and annular flows, which are necessary for analyzing and interpreting CFD simulation results and developing dimensionless correlations. Chapter 4 describes CFD modeling technique used to simulate the flow field for a steady, isothermal, fully developed laminar flow of power law fluids. Detailed description of the CFD procedure and assumptions implemented during the simulation are included in this chapter. CFD simulated results are presented in Chapter 5, demonstrating the effect of cuttings bed height on annular pressure loss and bed shear stress. Moreover, it presents a thorough comparison of CFD simulation results with published analytical and numerical studies as well as available experimental results. Chapter 6 summarizes major outcomes and findings of this investigation and recommendations to carry out future studies.

Chapter 2. Literature Review

Annular flow of non-Newtonian fluid encounters in many industrial applications such as flow in double pipe heat exchangers and extruders (Escudier et al., 2002). In the oil and gas industry, drilling fluid with complex rheological properties is circulated in the wellbore that has annular geometry. In the oil industry, accurate prediction of pressure loss and other hydraulic parameters such as bed shear stress are required in order to design an efficient hydraulic program and minimize costly operations. Fluid flow through annular space has been investigated for many decades (Lamb, 1945; Frederickson and Bird, 1958; Iyoho and Azar, 1981; Hacıislamoglu, 1989; Escudier et al., 2002; and Bicalho et al., 2016) considering the effects of various parameters such as flow rate, fluid properties and wellbore geometry on the bottomhole pressure. Laminar flow of non-Newtonian fluid in concentric annulus has been analyzed exhaustively and well understood. Nowadays, deviated wells are becoming more common. There is strong need for understanding fluid flow in these wells, which is often represented by partially blocked eccentric annular flow.

This section presents a review of the literature on flow of Newtonian and non-Newtonian fluids in concentric, eccentric, and partially blocked annuli. The review summarizes previous theoretical, computational and experimental studies.

2.1 Concentric Annulus

As mentioned before, a number of studies have been conducted to investigate concentric annular fluid flow due to its extensive application in many industrial operations. Generally, the studies can be grouped in two basic categories: analytical and numerical methods. In analytical methods, the governing system of equations (the

continuity and equations of motion) are solved to generate the velocity distribution across the flow field. Furthermore, in order to determine the volumetric flowrate, the obtained velocity profile is integrated over the flow cross sectional area. For concentric annular flow of Newtonian fluid, the governing equations can be solved analytically. For non-Newtonian fluids, analytical solution of the velocity profile cannot be obtained without applying some form of numerical procedures. For non-Newtonian fluids, a number of studies (Volarovich and Gutkin, 1946; and Fredrickson and Bird, 1958; Kozicki et al., 1966) have developed approximate models based on the Hagen-Poiseuille equation (1840), which relates pressure loss in cylindrical pipe to the flow rate. Its applicability and simplicity have served to develop approximate fluid flow models for concentric, eccentric and partially blocked annuli. A number of approximate models (Volarovich and Gutkin, 1946; and Fredrickson and Bird, 1958) have been developed for concentric annulus. An approximate analytical solution for Bingham plastic fluid was proposed by Volarovitch and Gutkin (1946); whereas Fredrickson and Bird (1958) presented simplified models for Bingham plastic and power law fluids. For annuli with small clearance ($\frac{R_i}{R_o} > 0.3$), the narrow slot approximate model (Bourgoyne et al., 1986) is used for a concentric annulus defining the width (W) and height (h) of an equivalent slot (Fig. 2.1a) as:

$$A = \pi(R_o^2 - R_i^2) = Wh \quad (2-1)$$

where

$$h = R_o - R_i \quad (2-2)$$

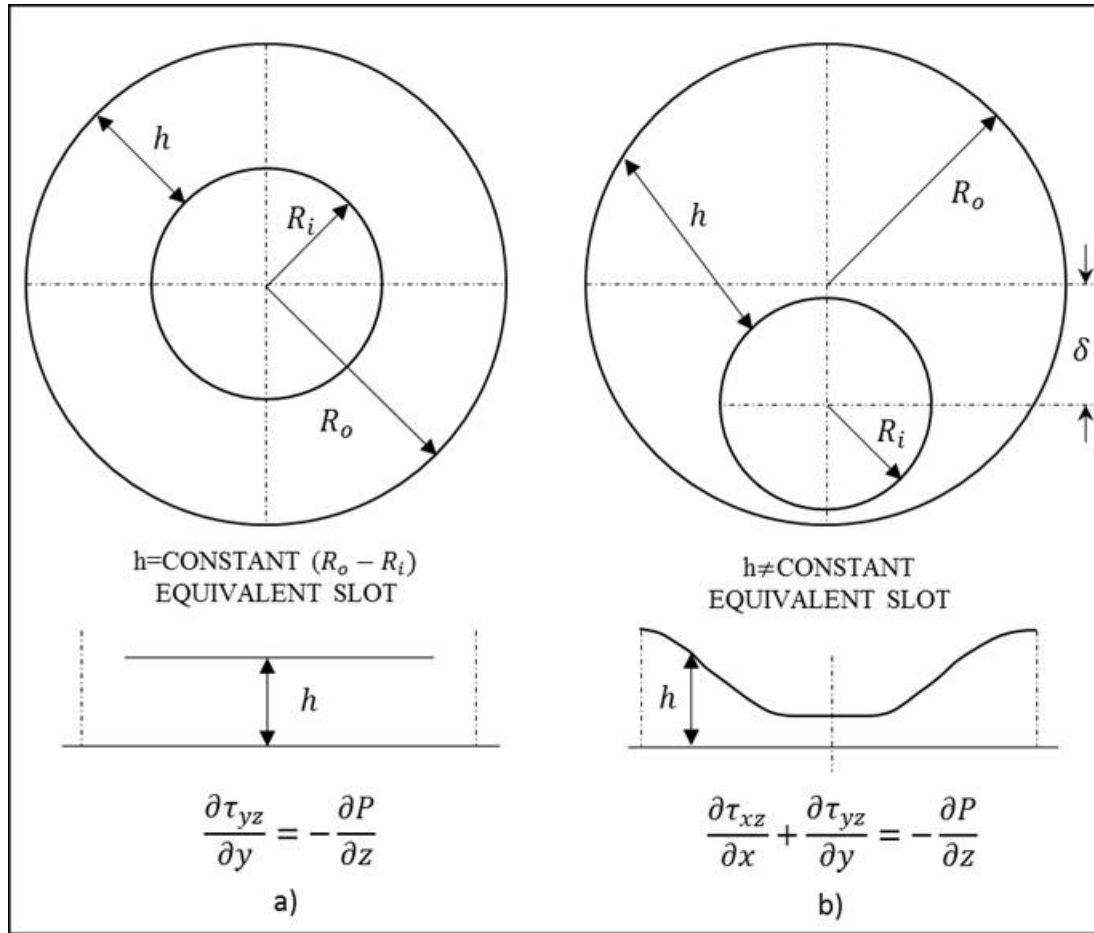


Figure 2.1 Slot equivalent of: (a) concentric; and (b) eccentric annuli (Haciislamoglu, 1989)

2.2 Eccentric Annulus

In inclined wells, the annular geometry possesses some level of eccentricity. Researchers have found that eccentricity substantially affects the predictions of various mathematical models that are currently used in drilling hydraulics. Experimental studies (Mitsuishi and Aoyagi, 1973; Nouri et al., 1993) confirmed reduction of pressure drop with eccentricity.

The governing equation of motion for fully developed laminar flow viscous fluid is expressed as:

$$-\frac{\partial p}{\partial z} + \frac{\partial}{\partial x} \left[\mu(\dot{\gamma}) \frac{\partial u}{\partial x} \right] + \frac{\partial}{\partial y} \left[\mu(\dot{\gamma}) \frac{\partial u}{\partial y} \right] = 0 \quad (2-3)$$

The above equation is valid for isothermal steady state flow of incompressible fluid, where z is oriented in the axial direction, u is the local axial velocity, and $\frac{\partial p}{\partial z}$ is the constant axial pressure gradient, which can be expressed as $\frac{\Delta P_f}{\Delta L}$. For Newtonian fluids, $\mu(\dot{\gamma})$ is the constant and molecular viscosity of the fluid. However, for non-Newtonian fluids, $\mu(\dot{\gamma})$ is the apparent viscosity, which is a function of shear rate ($\dot{\gamma}$).

For Newtonian fluids, an early study (Piercy et al., 1933) investigated the fluid flow through eccentric annulus (Fig. 2.1b) and derived an analytical solution applying bipolar coordinate transformation. The expression developed by Piercy et al. (1933) has become an enormous contribution of fluid flow analysis and widely used in industry, due to its accuracy in predicting strong influence of eccentricity on pressure loss.

$$Q = \frac{\pi}{8\mu} \left(-\frac{dp}{dz} \right) \left[R_o^4 - R_i^4 - \frac{4\delta^2 M^2}{\beta - \alpha} - 8\delta^2 M^2 \sum_{m=1}^{\infty} \frac{m e^{-m(\beta + \alpha)}}{\sinh(m\beta - m\alpha)} \right] \quad (2-4)$$

where:

$$M = (F^2 - R_o^2)^{1/2} \quad (2-5)$$

$$F = \frac{R_o^2 - R_i^2 + \delta^2}{2\delta} \quad (2-6)$$

$$\alpha = \frac{1}{2} \ln \frac{F+M}{F-M} \quad (2-7)$$

$$\beta = \frac{1}{2} \ln \frac{F-\delta+M}{F-\delta-M} \quad (2-8)$$

where δ corresponds to the offset distance between the centers of the pipe and the borehole (Eqn. 1.1).

For non-Newtonian fluids, the asymmetric nature of the eccentric annulus (Fig. 2.1b) makes analytical solution very complicated and difficult to obtain without approximation, which reduces accuracy. As a result, there is no exact analytical solution developed to date. Various approximate models and theoretical solutions encountered in the literature are presented in this section.

2.2.1 Analytical Studies

A number of studies transformed the eccentric annular geometry using bipolar coordinate transformation. Heyda (1959) obtained analytical solution for velocity profile of Newtonian fluid in eccentric annulus. The solution is presented in the form of an infinite series utilizing bipolar coordinates. The results demonstrated how the velocity profile changes with eccentricity. Later, Redberger and Charles (1962) used bipolar coordinates coupled with a conformal transformation to solve equation of motion for Newtonian fluids in eccentric annuli. Their results showed good agreement with Heyda's solution. Considering wide ranges of eccentricity ($0.1 \leq e \leq 0.9$) and diameter ratio ($0.5 < D_i/D_o < 0.8$), Snyder and Goldstein (1965) extended the work of Heyda (1955) and developed analytical expressions for velocity distribution, friction factor and local shear stress.

Applying bipolar coordinate transformation technique, Guckes (1975) predicted the relationship between flowrate and frictional pressure for non-Newtonian fluids (Bingham plastic and power-law fluids) in eccentric annulus. The relationship between volumetric flowrates and frictional pressure loss was developed numerically integrating the velocity profile. However, the computational model exhibited numerical instability at large eccentricities (Haciislamoglu and Langlinais, 1990). In general, bipolar

coordinate transformation consists of two orthogonal families of circles, ε and η , which represent the walls of an eccentric annulus as it is illustrated in Fig. 2.2. A modified and more simplified form of the equation of motion in bipolar coordinates has been developed by Sijun (1994) and Hacıislamoglu (1989). In bipolar transformation method, the equation of motion is transformed from Cartesian coordinates to bipolar coordinates as (Spiegel, 1968):

$$x = \frac{a^* \sinh \varepsilon}{\cosh \varepsilon - \cos \eta} \quad (2-9)$$

$$y = \frac{a^* \sin \varepsilon}{\cosh \varepsilon - \cos \eta} \quad (2-10)$$

and

$$L = L \quad (2-11)$$

where L is the third axis which is perpendicular to ε and η , and a^* is defined as: $a^* = R_i \sinh \varepsilon_i = R_o \sinh \varepsilon_o$, for: $0 \leq \eta \leq 2\pi$ and $-\infty \leq \varepsilon \leq +\infty$ and $-\infty \leq L \leq +\infty$. ε_i and ε_o are determined from (Guckes, 1974):

$$\varepsilon_i = \cosh^{-1} \left[\frac{(1+\kappa) - e^2(1-\kappa)}{a^* e \kappa} \right] \quad (2-12)$$

$$\varepsilon_o = \cosh^{-1} \left[\frac{(1+\kappa) - e^2(1-\kappa)}{a^* e} \right] \quad (2-13)$$

where e and κ are the relative eccentricity and diameter ratio, respectively.

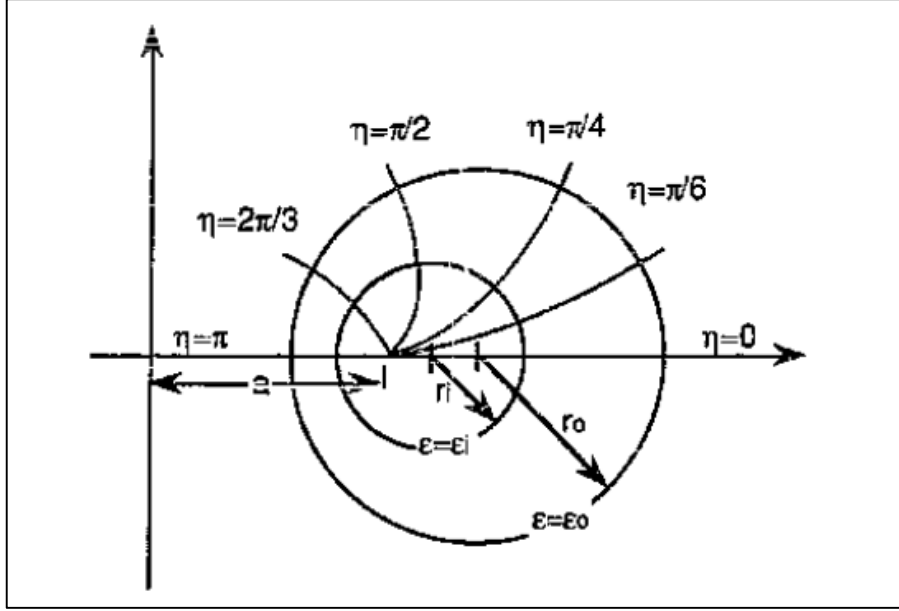


Figure 2.2 Eccentric annulus in bipolar coordinates (Haciislamoglu, 1989)

Consequently, the transformed equation of motion in the bipolar coordinates system is expressed as (Haciislamoglu, 1989):

$$\left(\frac{\alpha}{\psi}\right)^2 \frac{\Delta P_f}{\Delta L} + \frac{\partial}{\partial \varepsilon} \left(\mu \frac{\partial v}{\partial \varepsilon} \right) + \frac{\partial}{\partial \eta} \left(\mu \frac{\partial v}{\partial \eta} \right) = 0 \quad (2-14)$$

where:

$$\psi = \cosh \varepsilon - \cos \eta \quad (2-15)$$

for $\varepsilon_o \leq \varepsilon \leq \varepsilon_i$ and $0 \leq \eta \leq 2\pi$, where μ is apparent viscosity and it depends upon the rheological model selected.

Theoretically, the bipolar coordinate transformation technique provides exact solution. However, it requires computationally intensive procedures. Haciislamoglu and Langlais (1990) developed a numerical scheme to solve the equation for power-law fluids, for a wide range of eccentricities ($0 \leq e \leq 0.95$), where their results agreed reasonably well with the experimental data of Mitsubishi and Aoyagi (1973).

2.2.2 Numerical Studies

After applying the bipolar transformation, Redberger and Charles (1962) used a finite different technique to obtain the velocity profile for Newtonian fluids in eccentric annuli. As mentioned earlier, the velocity profile is integrated numerically to provide a relationship between flowrate and pressure drop for different eccentricities. Later, Guckes (1975) presented procedures for calculating volumetric flowrate for power-law and Bingham plastic fluids, using finite difference technique after applying the bipolar transformation. Hacıislamoglu and Langlinais (1990) also used the bipolar transformation to developed a simplified correlation for relating the ratio of frictional pressure losses in an eccentric annulus to that of concentric annulus considering wide ranges of eccentricity ($0 \leq e \leq 0.95$), diameter ratio ($0.3 < D_i/D_o < 0.9$), and fluid behavior index ($0.4 < n < 1.0$) (Appendix D). A more recent numerical study (Fang et al., 1999) evaluated the effects of eccentricity on the product of friction factor and Reynolds number (fRe). For eccentric annulus, friction factor and Reynolds number are expressed as:

$$f = \frac{\left(-\frac{dp}{dz}\right)D_{hyd}}{2\rho U^2} \quad (2-16)$$

$$Re = \frac{\rho U^{2-n} D_{hyd}^n}{K} \quad (2-17)$$

Fanning friction factor is expressed in terms of pressure gradient and hydraulic diameter (D_{hyd}). Furthermore, Reynolds number is defined in terms of hydraulic diameter, mean velocity (U), density (ρ), and consistency index (K). Fang et al. (1999) demonstrated that the hydraulic parameter, fRe in eccentric annulus is a function of dimensionless eccentricity (e), radios ratio (κ) and fluid behavior index (n). Other numerical studies (Fang and Manglik, 2002; and Escudier et al., 2002) reported similar

findings. Table 2.1 presents the hydraulic parameter as a function of dimensionless eccentricity, power law index and diameter ratio obtained by Fang et al. (1999).

Table 2.1 Hydraulic parameter (fRe) for power-law fluids (Fang et al., 1999)

κ	e	n					
		0.2	0.4	0.5	0.6	0.8	1.0
0.2	0	3.6458	6.1481	7.7196	9.6670	14.987	23.100
				7.73 ^a	9.66 ^a	14.99 ^a	23.10 ^a
	0.05	3.7240	6.1517	7.7171	9.6464	14.953	23.028 (23.023) ^b
	0.1	3.7875	6.1319	7.6850	9.5994	14.848	22.837 (22.829)
	0.2	3.7768	6.0423	7.5423	9.3835	14.436	22.102 (22.093)
	0.3	3.7355	5.8823	7.3032	9.0484	13.806	20.993 (20.985)
	0.4	3.6401	5.6620	6.9931	8.6203	13.032	19.648 (19.641)
	0.5	3.5114	5.4071	6.6431	8.1462	12.192	18.202 (18.197)
	0.6	3.3687	5.1417	6.2840	7.6622	11.349	16.764 (16.760)
0.5	0.8	3.1137	4.6463	5.6103	6.7787	9.8195	14.182 (14.181)
	0	3.7684	6.3122	7.9395	9.9497	15.450	23.811
				7.95 ^a	9.95 ^a	15.45 ^a	23.81
	0.05	3.8336	6.3086	7.9293	9.9242	15.399	23.728 (23.729) ^b
	0.1	3.8168	6.2567	7.8600	9.8307	15.248	23.480 (23.481)
	0.2	3.7608	6.0610	7.5978	9.4904	14.675	22.542 (22.541)
	0.3	3.5989	5.7641	7.2066	8.9765	13.822	21.140 (21.139)
	0.4	3.4039	5.4141	6.7443	8.3734	12.804	19.459 (19.458)
	0.5	3.2093	5.0507	6.2610	7.7350	11.726	17.671 (17.671)
0.8	0.6	3.0216	4.6996	5.7909	7.1147	10.667	15.709 (15.909)
	0.8	2.7034	4.0776	4.9535	6.0022	8.7683	12.755 (12.755)
	0	3.8233	6.3488	7.9966	10.023	15.557	23.978
				8.00 ^a	10.01 ^a	15.56 ^a	23.98 ^a
	0.05	3.8345	6.3414	7.9758	9.9838	15.501	23.889 (23.891) ^b
	0.1	3.8280	6.2679	7.8880	9.8767	15.336	23.626 (23.627)
	0.2	3.6554	6.0146	7.5725	9.4819	14.711	22.630 (22.631)
	0.3	3.4315	5.6541	7.1173	8.9087	13.787	21.145 (21.145)
	0.4	3.1958	5.2474	6.5933	8.2342	12.691	19.367 (19.367)
0.5	2.9723	4.8379	6.0564	7.5387	11.536	17.480 (17.480)	
0.6	2.7684	4.4499	5.5415	6.8624	10.405	15.622 (15.622)	
0.8	2.4085	3.7733	4.6359	5.6679	8.3879	12.304 (12.304)	

^aResults of Capobianchi and Irvine (1992)

^bResults in parenthesis are from Piercy et al. (1933)

2.2.3 Modeling Studies

The narrow slot approximation model has been widely used to predict pressure loss in eccentric annulus. The model considers a variable slot height. Tao and Donovan (1955) treated eccentric annulus as a slot of variable height as shown in Fig. 2.1b and

develop a narrow slot model for Newtonian fluids. However, the mathematical expression for the slot height adopted was inaccurate, and the equation used in their study is applicable for narrow-clearance concentric annuli, limiting its use significantly. Later, Vaughn (1965) extended the work of Tao and Donovan (1955) for non-Newtonian fluids, but the equation for the slot height was still inaccurate. Later, accurate slot height models (Iyoho and Azar, 1980; Uner et al., 1989; and Luo and Peden, 1987) were developed. This has improved accuracy of slot method, even though the use of a model valid for narrow-clearance concentric annulus results in inaccuracy (Haciislamoglu, 1989).

Another approximate solution developed for eccentric annulus is an equivalent pipe model based on the method developed by Kozicki et al. (1966), which proposes a generalized model for determining pressure loss in ducts with arbitrary cross-sectional geometry. The model defines a hydraulic parameter (fRe), which is a function of two dimensionless geometric parameters (a and b). Re is the Reynolds number expressed as:

$$Re_{gen} = \frac{\rho U^{2-n} D_{hyd}^n}{8^{n-1} K \left(\frac{a+bn}{n}\right)^n} \quad (2-18)$$

For eccentric annulus, the geometric parameters, a and b are functions of eccentricity and diameter ratio. Based on published numerical results (Fang et al., 1999), Ahmed et al. (2006) developed correlations for the geometric parameters for PL fluids in eccentric annulus. The parameters are expressed in terms of dimensionless eccentricity as:

$$a = a_0 e^3 + a_1 e^2 + a_2 e + a_3 \quad (2-19a)$$

$$b = \alpha_0 e^3 + \alpha_1 e^2 + \alpha_2 e + \alpha_3 \quad (2-19b)$$

where $a_0, a_1, a_2, a_3, \alpha_0, \alpha_1, \alpha_2,$ and α_3 are coefficients of the correlations, which are defined in Table 2.2.

Table 2.2 Coefficients used in Eq. (3-16) (Ahmed et al., 2006)

$a_0 = -2.8711\kappa^2 - 0.1029\kappa + 2.6581$	$\alpha_0 = 3.0422\kappa^2 + 2.4094\kappa - 3.1931$
$a_1 = 2.8156\kappa^2 + 3.6114\kappa - 4.9072$	$\alpha_1 = -2.7817\kappa^2 - 7.9865\kappa + 5.8970$
$a_2 = 0.7444\kappa^2 - 4.8048\kappa + 2.2764$	$\alpha_2 = -0.3406\kappa^2 + 6.0164\kappa - 3.3614$
$a_3 = -0.3939\kappa^2 + 0.7211\kappa + 0.1503$	$\alpha_3 = 0.2500\kappa^2 - 0.5780\kappa + 1.3591$

2.2.4 Experimental Studies

An earlier experimental study (Mitsuishi and Aoyagi 1973), on fully developed laminar flow of non-Newtonian fluid confirmed the reduction of friction pressure due to inner pipe eccentricity. Moreover, fluids with a stronger non-Newtonian behavior (i.e. fluids with low n values) showed a lower pressure reduction with eccentricity than fluids with weak non-Newtonian behavior (fluids with higher n values). A number of recent studies (Hansen et al., 1999; Nouri et al., 1993; Nouri and Whitelaw, 1997; Wang et al., 2000; Ozbayoglu, 2002; and Silva and Shah, 2000) conducted on Newtonian and non-Newtonian fluids experimentally evaluated the reduction of frictional pressure loss due to eccentricity. Results confirmed frictional pressure loss reduction of up to 40% due to eccentricity.

2.3 Partial Blocked Annulus

In horizontal and highly inclined wells stationary cuttings beds form on the low side of the annulus due to low mud velocity, which is not sufficient to produce a good hole cleaning performance. Thus, blocked eccentric annular geometry (Fig. 2.3) is expected in directional wells. Due to complexity of the flow geometry, solutions to the governing equations are only obtained using numerical procedures.

2.3.1 Numerical studies

A study on block annular flow (Chin, 1992) presented velocity and apparent viscosity profiles for several annular geometries (including boreholes with cuttings bed). The study used boundary conforming natural coordinates to obtain numerical solution applying finite different method. Later, several numerical studies (Azouz et al., 1993; Azouz 1994; Hussain and Sharif, 1998; Aworunse, 2012) were conducted using non-orthogonal, curvilinear, and boundary fitted coordinate systems. These numerical studies investigated the relationship between flowrate and pressure gradient. The results were compared with results of previous theoretical and experimental studies and exhibited good agreement.

Based on curvilinear coordinate transformation, Aworunse (2012) developed a numerical model and generated simulation results to formulate correlations for the geometric parameters a and b in partially blocked annuli with 80% eccentricity. The parameters are expressed as a function of the eccentricity, diameter ratio, fluid behavior index, and bed height. The correlations help to predict the frictional pressure loss. Aworunse's correlations were developed following a procedure established by Ahmed et al. (2006) to present similar correlations for eccentric annulus (See Appendix B).

Recently, Tang et al. (2016) have developed a hydraulic model based on CFD simulation results. The model is applicable for flow of YPL fluids in a partially blocked concentric annulus. The model has shown better accuracy than an existing model which is proposed by Chen (2005), who formulated a semi-empirical model based on effective diameter concepts (Whitaker, 1985).

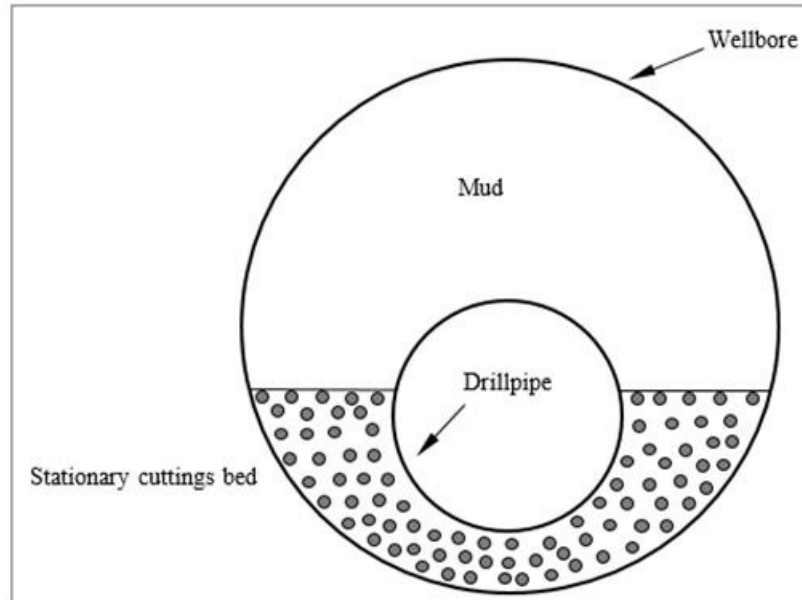


Figure 2.3 Wellbore cross section with cuttings bed

2.3.2 Experimental Studies

Very few experimental studies have performed to investigate laminar flow in partially obstructed annulus. Recently, Bicalho et al. (2016) presented results of experimental studies showing pressure drop and fluid velocity profile in partially obstructed annular space for yield-power law fluids. CFD simulation validation was also considered in this study. Other experiments have simulated equilibrium bed heights to evaluate wellbore cleaning performance of the fluid in a fully eccentric annular arrangement (Elgaddafi, 2011; and George, 2012). In these studies, for a given flow rate, the stationary cuttings bed height was measured along with the pressure drop.

2.4 Computational Fluid Dynamics (CFD)

Computational Fluid Dynamics (CFD) is a method used to solve numerically fluid dynamics equations to predict flow field in complicated geometries. It is often used to

model natural phenomena such as fluid flow, heat transfer, mass transfer and chemical reactions. Its applicability is extended to other engineering disciplines for analyzing flows in complex geometries. CFD provides relevant simulation data used in new product development and existing system troubleshooting or redesigning. In addition, CFD complements laboratory testing by providing simulation database that reduces required laboratory experiments, which can be expensive and time consuming.

In the oil industry, analysis of fluid flow in the wellbore is one of common fluid mechanics problems. CFD is becoming a major tool in solving many of wellbore related flow problems. Velocity profile, pressure loss and wall shear stress distribution can be determined using CFD. A number of CFD studies (Escudier et al., 2002; Fang et al., 1999; Ozbayoglu and Omurlu, 2006; and Pereira et al., 2007) reported hydraulic characteristics (pressure loss and velocity profiles) of non-Newtonian fluid flows in concentric and eccentric annuli. Some of these studies compared simulation results with existing measurements and theoretical results. Pereira et al. (2007) validated CFD simulation results with published measurements (Escudier et al., 2002).

Several studies were conducted using commercially available CFD software to analyze fluid flows in the wellbore. Ogugbue et al. (2011) studied fully developed laminar annular flow of Newtonian and power law fluids using commercial CFD software. Different annular eccentricities ($0 \leq e \leq 0.96$) and diameter ratios ($0.3 \leq \kappa \leq 0.8$) were considered in the investigation. Results were compared with published experimental and CFD database (Mitsubishi and Aoyagi, 1974; Hacıislamoglu and Langlinais, 1990; and Nouri and Whitelaw, 1994). Predictions obtained from CFD

simulation show good agreement with experimental measurements and theoretical results.

Recent studies (Bicalho et al., 2016; Tang et al., 2016) demonstrated the capability of commercial CFD software in analyzing flow in complex geometries such as partially obstructed annuli. The simulation results were validated with experimental data obtained by testing non-Newtonian fluids in concentric and eccentric annuli. Other effects such as inner pipe rotation and orbital motion have also been studied (Escudier, 2002; Fang et al., 1999; Pereira et al., 2007; Bicalho et al., 2016) using CFD.

Chapter 3. Basic Theory of Laminar Flow

In this chapter, basic theories and governing equations, which are utilized in theoretical analysis and CFD simulation of wellbore flow, are described in detail. The material presented in this chapter helps to better understand and interpret CFD simulation results, and develop simplified hydraulic models for annular pressure loss and bed shear stress distribution.

3.1 Rheological Models and Relevant Hydraulic Parameters

The rheological models used to represent fluid behavior are mostly classified as Newtonian and non-Newtonian. Newtonian fluids such as water and mineral oil exhibit a linear relationship between shear stress and shear rate under laminar flow conditions. Non-Newtonian fluids such as clay muds and polymeric suspensions display a non-linear relationship between shear stress and shear rate. Figure 3.1 presents rheological models, which are commonly used to describe time-independent fluids in the industry. The power-law model relates the shear stress with shear rate as:

$$\tau = K(\dot{\gamma})^n \quad (3-1)$$

where $\dot{\gamma}$ is the shear rate. K and n are two rheological parameters known as fluid consistency index and power law exponent (also known as fluid behavior index), respectively. Equation 3-1 can be re-written using apparent viscosity as (Bird et al., 1960):

$$\tau = \mu(\dot{\gamma})\dot{\gamma} \quad (3-2)$$

where $\mu(\dot{\gamma})$ is the apparent viscosity, which is a function of shear rate.

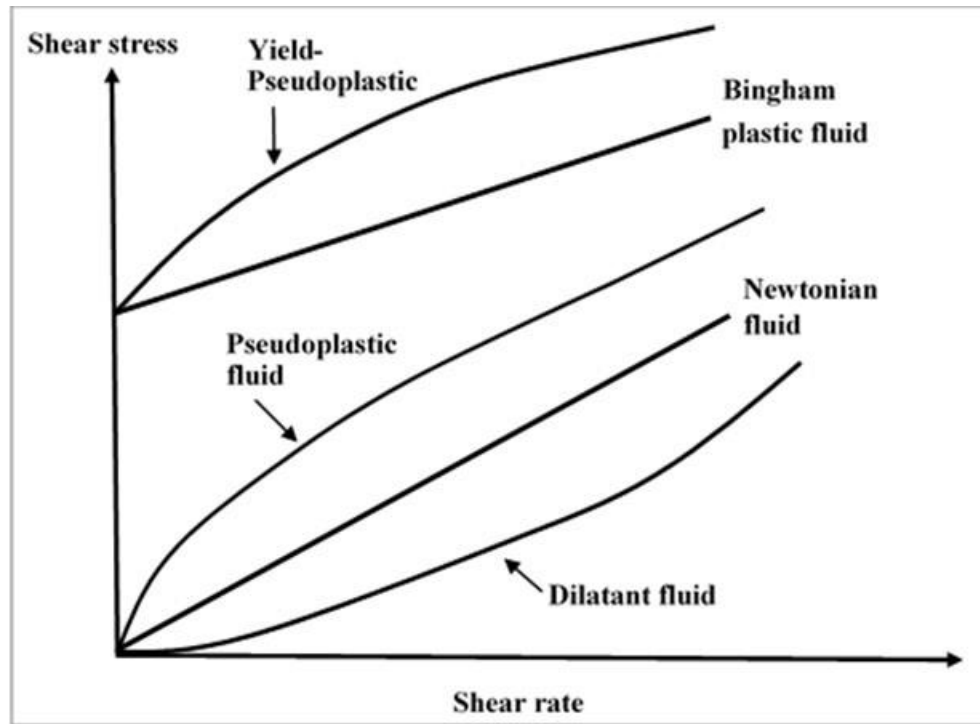


Figure 3.1 Time-independent non-Newtonian fluid types (redrawn from Nguyen et al., 2012)

$$\mu(\dot{\gamma}) = K\dot{\gamma}^{n-1} \quad (3-3)$$

In Eqns. 3.2 and 3.3, $\mu(\dot{\gamma})$ is the ratio of shear stress and shear rate, and it represents a measurement of the fluid's flow behavior. In Equations 3.1 and 3.3, if n is less than one, the fluid exhibits shear-thinning properties (or pseudo-plastic behavior); as a result, the apparent viscosity decreases with shear rate. For $n = 1$ the fluid shows the well-known Newtonian behavior. On the other hand, for n greater than one, the fluid shows a shear-thickening behavior (or dilatant fluid behavior), in which the apparent viscosity increases with shear rate. Figure 3.2 exemplifies the behavior of these three type of fluids in terms of apparent viscosity. Polymer melts and some drilling fluids best fit the power-law fluid model with shear- thinning behavior (Nguyen et al., 2012).

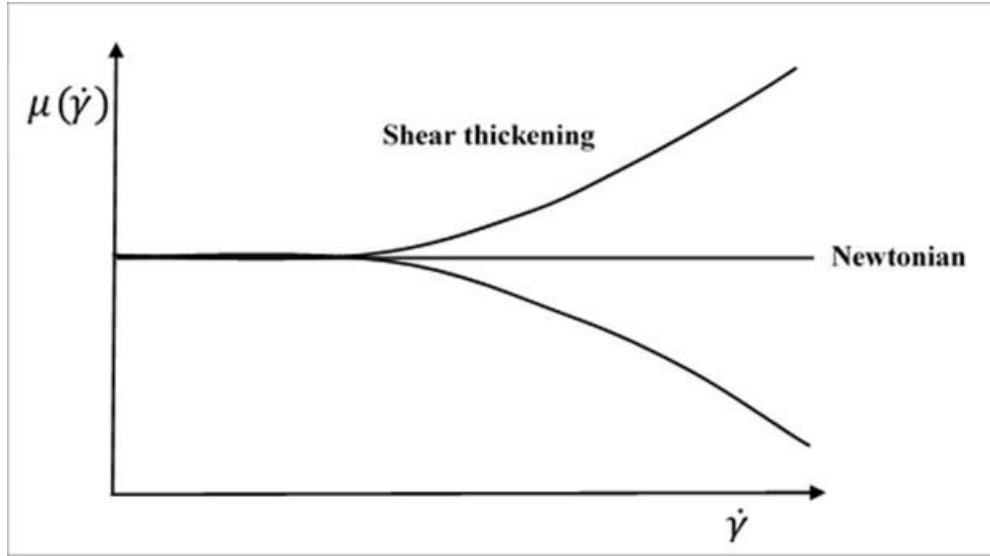


Figure 3.2 Viscosity of Newtonian, shear thinning and shear thickening as a function of shear rate. (Willenbacher and Georgieva, 2013)

The shear rate for flow between parallel plates (one stationary and another moving) is expressed as:

$$\dot{\gamma} = -\frac{dv}{dy} \quad (3-4)$$

In two dimensions, the definition of shear rate in a Cartesian coordinate system (Bird et al., 1960) is expressed as:

$$\dot{\gamma} = \left[\left[\left(\frac{\partial u}{\partial x} \right)^2 + \left(\frac{\partial u}{\partial y} \right)^2 \right]^{1/2} \right] \quad (3-5)$$

Volumetric Flow Rate and Annular Velocity

The volumetric flow rate is the volume of fluid that is passing through a given cross sectional area per unit time. Thus:

$$Q = \frac{\Delta V}{\Delta t} \quad (3-6)$$

where ΔV is the volume passing through a control volume and Δt is the change in time.

The annular velocity is the speed at which the fluid (i.e. drilling fluid or cement) travels in the annulus. Selection of appropriate annular fluid velocity, together with proper drilling fluid rheological properties help to keep the wellbore clean and prevent formation of cuttings bed.

Reynolds Number

Reynolds number (Re) is a dimensionless flow parameter defined as the ratio of the inertial force to viscous force under certain flow conditions.

$$Re = \frac{\text{Inertial forces}}{\text{viscous forces}} \quad (3-7)$$

The Reynolds number governs the transition from laminar to turbulent flow. The flow is considered laminar if the fluid flow is streamlined at low velocities and highly ordered motion (Fig. 3.2), and the magnitude of the Reynolds number is below the critical value, which is 2100 for circular pipe flow. Turbulent flow develops when laminar flow becomes unstable; resulting in velocity fluctuations and highly disordered fluid motion. The transition zone, which occurs in the Reynolds number range of 2100 to 4000 is a function of pipe roughness, flow velocity and fluid type.

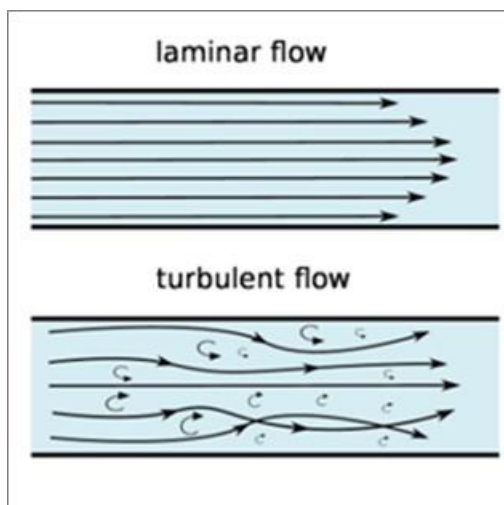


Figure 3.3 Laminar vs. turbulent flow in pipe flow. (Schlichting, 2000)

Hydraulic Diameter

The hydraulic diameter, D_{hyd} , is a parameter commonly used when handling flow in non-circular ducts. The hydraulic diameter transforms non-circular ducts into pipes of equivalent diameter such that the flow behavior in annulus is equivalent to that in a circular pipe. The hydraulic diameter for any duct/channel with uniform cross section is expressed as:

$$D_{hyd} = \frac{4 \cdot \text{cross-sectional-area of duct}}{\text{wetted perimeter of duct}} \quad (3-8)$$

Fanning Friction Factor

The fanning friction factor is the ratio of the average wall shear stress to the velocity head. The general form of the fanning friction for pipe flow is also described as:

$$f = \frac{\tau_w}{\rho \frac{U^2}{2}} \quad (3-9)$$

where U refers to the mean annular velocity, τ_w is the average wall shear stress, and ρ corresponds to fluid density. The product of the Fanning friction factor-Reynolds number, fRe is a very important hydraulic parameter, which describes hydraulic resistance of a duct.

Wall Shear Stress

Wall shear stress is defined as a parallel (to the wall) force per unit area that is exerted by the flowing fluid on the surface of a conduit. For laminar Newtonian duct flows, the magnitude of wall shear stress is proportional to the velocity gradient near the wall. In partially obstructed annulus, the presence of stationary cuttings bed changes shear stress distribution. The shear stress acting on the bed determine lift and drag forces acting on flow protruding bed particles (Ahmed et al., 2002; and Elgaddafi, 2011; George et al., 2014). Cuttings concentration in the annulus is strongly related to mean bed shear

stress. In fact, one way of evaluating the drag force acting on a solid particle during bed erosion is to use the pressure gradient across the channel and the average bed shear stress (Ahmed et al., 2002). Hence, bed shear stress modeling is an important part of the present study.

3.2 Pipe Flow

Fully developed laminar flow of Newtonian fluid in a cylindrical tube (i.e. no-slip boundary conditions) generates a parabolic velocity profile. Figure 3.4 shows the velocity profile in a tube with radius R , where the velocity is highest at the center ($r = R$) and zero at the tube walls ($r = 0$). The pipe flow is usually referred as the Hagen-Poiseuille flow, and the volumetric flow rate can be obtained from the following equation (detail is presented in Appendix B):

$$Q = \frac{R^4 \Delta P}{8\mu \Delta L} \quad (3-10)$$

where Q is the volumetric flow rate, μ is the dynamic viscosity, and $\frac{\Delta P}{\Delta L}$ is the axial pressure gradient.

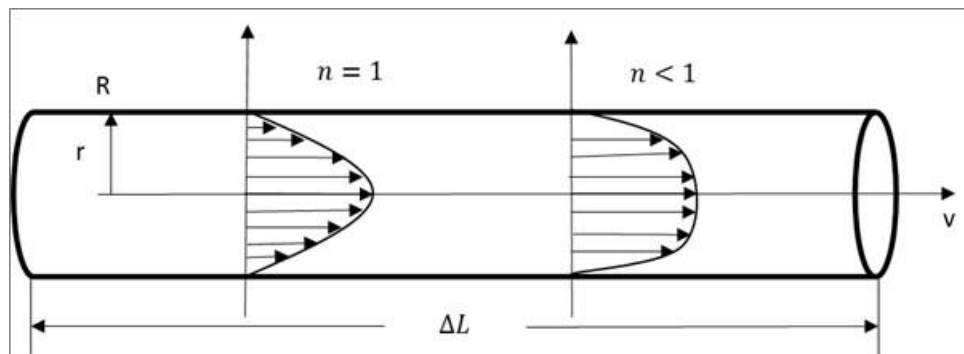


Figure 3.4 Laminar velocity profile in a circular pipe flow

It should be pointed out from Fig. 3.4 that the velocity profile for a power law fluid flattens as the flow behavior index of the fluid decreases. For a circular pipe, the shear stress distribution is linear and maximizes at the tube wall ($r = R$). It is zero at the tube axis ($r = 0$). The wall shear stress is defined as:

$$\tau_w = \frac{\Delta P D}{\Delta L 4} \quad (3-11)$$

where D is the diameter of the pipe. The above equation is valid for incompressible flow under steady state condition.

Theoretical analysis of pipe flow resulted in the development of the Rabinowitsch-Mooney equation, which expresses the relationship between flow rate and wall shear rate. A simplified form of the equation is expressed as:

$$\dot{\gamma}_w = \left(\frac{8U}{D}\right) \left[\frac{3}{4} + \frac{1}{4} \frac{d \ln(8U/D)}{d \ln \tau_w}\right] \quad (3-12)$$

where $\dot{\gamma}_w$ is the wall shear rate for generalized fluid. The term $\frac{8U}{D}$ in Eqn. 3.12 represents the flow characteristic and it is a unique function of the wall shear stress, τ_w . For Newtonian fluid, the wall shear rate is $\frac{8U}{D}$. Hence, the wall shear stress is expressed as:

$$\tau_w = \mu \frac{8U}{D} \quad (3-13)$$

Equation 3.12 demonstrates the relationship between wall shear rates of Newtonian and non-Newtonian fluids having the same flow rate in the same pipe. The quantity in the square brackets is often considered as a correction factor. For power-law fluids, $n = \frac{d \ln \tau_w}{d \ln(8U/D)}$. Applying Eqn. 3.1, wall shear stress for a power-law fluid can be expressed as:

$$\tau_w = K \left(\left(\frac{3n+1}{4n} \right) \frac{8U}{D} \right)^n \quad (3-14)$$

For Newtonian pipe flows, the Reynolds number is defined as:

$$Re = \frac{\rho UD}{\mu} \quad (3-15)$$

where ρ is the density of the fluid.

Combining Eqns. 3.15 and 3.9, the Fanning friction factor can be expressed in terms of the Reynolds number as:

$$f = 16/Re \quad (3-16)$$

The above equation is valid for laminar flow (i.e. when the Reynolds number is less than 2100). For power law fluids, the generalized Reynolds number is defined as:

$$Re_{gen} = \frac{D^n U^{2-n} \rho}{8^{n-1} K \left(\frac{3n+1}{4n} \right)} \quad (3-17)$$

3.3 Concentric Annular Flow

The velocity profile and shear stress distribution for a narrow slot flow are presented in Fig. 3.4. The simplified Rabinowitsch-Mooney (Eqn. 3.12) can be adopted for non-Newtonian fluid flowing in a thin slit of height h . For this, the definition of hydraulic diameter D_{hyd} for a slit is substituted in Eqn. 3.12. For a circular pipe $D = D_{hyd}$ and for the slit the hydraulic diameter $D_{hyd} = 2h$. Due to close similarity in wall shear stress expressions of both geometries, Kozicki et al. (1966) proposed a generalized wall shear stress formula, which is applicable for any arbitrarily shaped duct (generalized duct) that has a constant cross-section. Thus, for a power law fluid, the average wall shear stress is expressed in a general form as:

$$\bar{\tau}_w = K \left\{ \frac{8U}{D_{hyd}} \left(b + \frac{a}{n} \right) \right\}^n \quad (3-18)$$

where a and b are two geometric parameters characterizing the cross-section of the duct. For pipe flow: $a = 1/4$ and $b = 3/4$, whereas for slit flow: $a = 1/2$ and $b = 1$.

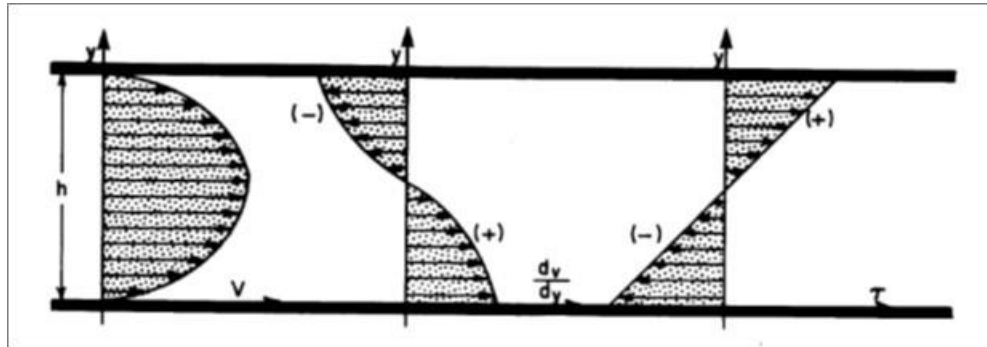


Figure 3.5 Velocity and wall shear stress profile for laminar flow- narrow slot-power-law fluids (Bourgoyne et al., 1986)

The wall shear stresses acting at the inner and outer pipe walls are not identical for concentric annulus because the velocity profile is not symmetric. Figure 3.6 shows Newtonian velocity distribution in a concentric annulus. For power law fluids, the velocity profile becomes flatter as the shear thinning behavior of the fluid increases.

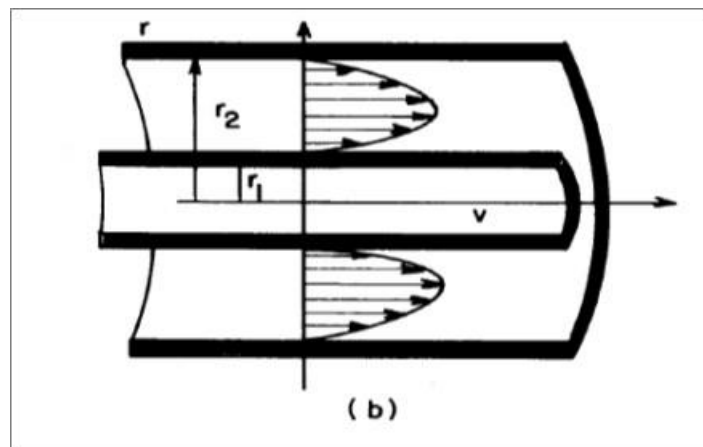


Figure 3.6 Velocity profile of Newtonian laminar flow in concentric annulus (Bourgoyne et al., 1986)

Applying momentum balance for slot approximated annular flow, the average wall shear stress $\bar{\tau}_w$ can be written as a function of pressure gradient:

$$\bar{\tau}_w = \frac{dp}{dz} \frac{D_{hyd}}{4} \quad (3-19)$$

Considering analogy to pipe flow, the Fanning friction factor for annular flow is expressed using hydraulic diameter as expressed in Eqn. 2.16 (Section 2.2.2).

In Eqn. 3.17, the generalized Reynolds number should be used for non-Newtonian fluids.

Thus, $f = 16/Re_{gen}$, where the generalized Reynolds number is expressed as a function of geometric parameters (a and b). Thus:

$$Re_{gen} = \frac{\rho U^{2-n} D_{hyd}^n}{8^{n-1} K \left(\frac{a+bn}{n}\right)^n} \quad (3-20)$$

For concentric annuli, the generalized duct geometric parameters are expressed as functions of diameter ratio, κ , (Kozicki et al., 1966):

$$a + b = \frac{(1-\kappa)^2}{1+\kappa^2 - \frac{1-\kappa^2}{\ln 1/\kappa}} \quad (3-21)$$

and

$$a = \frac{(1-\kappa)^2}{4 \left\{ 1 - \frac{1-\kappa^2}{2 \ln 1/\kappa} \left[1 - \ln \frac{1-\kappa^2}{2 \ln 1/\kappa} \right] \right\}} \quad (3-22)$$

3.4 Eccentric Annular Flow

For Newtonian fluids, Piercy et al. (1933) analytically determined the relationship between flowrate and pressure loss in eccentric annuli (Eqn. 2.4). As annular geometry becomes complex, approximate and simplified models are considered for drilling applications. Most common models used to predict pressure loss in eccentric annulus are: the narrow-slot model, numerical result based correlations (Haciislamoglu and

Langlinais, 1990), and generalized duct model (Kozicki et al. 1966). In this study, the last approach is applied to model partially blocked eccentric annulus.

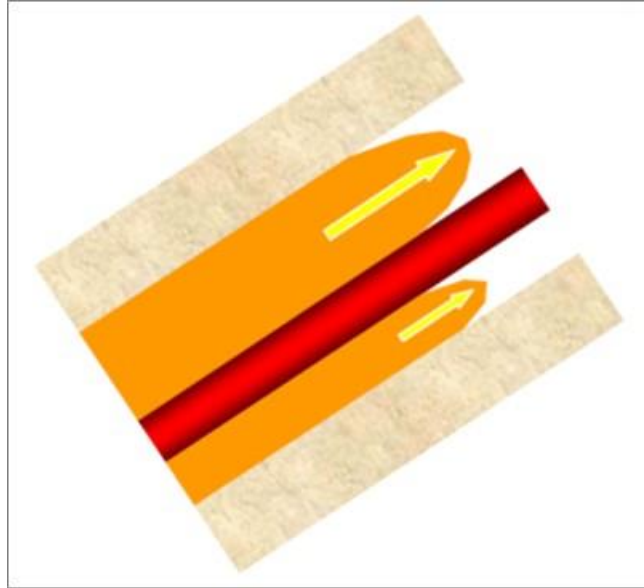


Figure 3.7 Velocity profile for laminar flow in eccentric annulus flow (Ebrahim et al., 2013)

The relationship between Fanning friction factor and the generalized Reynolds number ($f = 16/Re_{gen}$) can be combined with Eqn. 3.20 to yield the following expression:

$$\frac{fRe}{8^{n-1}} \left(\frac{n}{a+bn} \right)^n = 16 \quad (3-23)$$

The above expression is rearranged to determine the friction factor in terms of the geometric parameters:

$$f = \frac{2^{3n+1}}{Re} \left(\frac{a}{n} + b \right)^n \quad (3-24)$$

where Re a modified Reynolds number, which is defined in Eqn. 2.17 (Section 2.2):

Ahmed et al. (2006) developed a shape factor, $s(n, e, \kappa)$, by rearranging Eqn.

3.24:

$$s(n, e, \kappa) = \left(\frac{a}{n} + b\right) = \left(\frac{fRe}{2^{3n+1}}\right)^{1/n} \quad (3-25)$$

where the geometric parameters a and b are determined by plotting the shape factor (right side) as a function of $1/n$. Thus, the left side of Eqn. 3.25 represents the equation of a straight line. Adjusting the points to a linear trend line, a is obtained by the slope, and b is the intercept of the straight line as it can be observed in Fig. 3.8. This equation confirms that the shape factor is a function of geometric parameters and fluid behavior index.

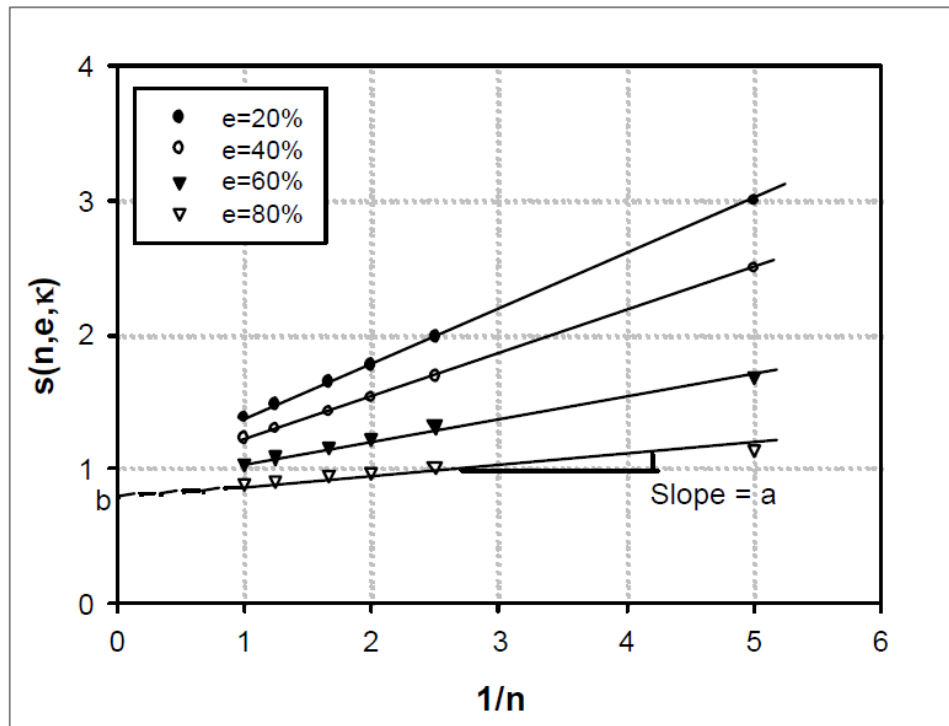


Figure 3.8 Shape factor vs. $1/n$ for eccentric annulus with diameter ratio of 0.2 (Ahmed et al., 2006)

3.5 Flow in Partially Blocked Annulus

Previous numerical models (Azouz et al., 1993; Azouz, 1994; Hussain and Sharif, 1998) described laminar velocity profile of Newtonian and non-Newtonian fluids in partially obstructed annulus. However, no correlation or approximated model was developed to estimate the pressure loss in partially blocked annulus until 2012. As mentioned earlier, Aworunse (2012) adapted the method developed by Ahmed et al. (2006) to estimate the geometric parameters a and b of partially blocked annuli.

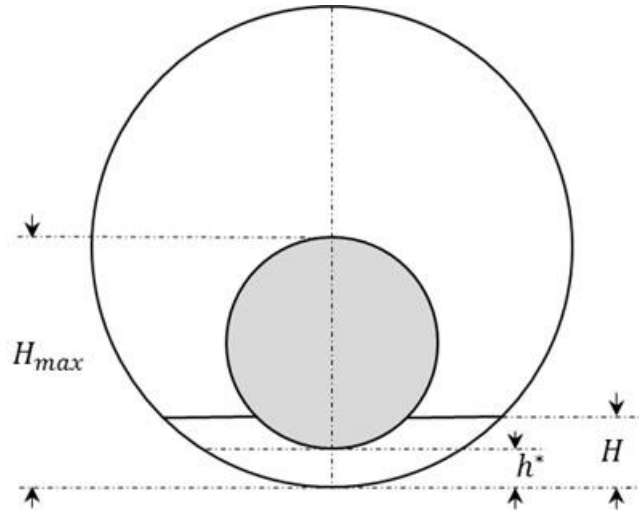


Figure 3.9 Eccentric annulus with cuttings bed geometry

According to Azouz et al. (1993), the distribution of the axial shear stress on cuttings bed surface is non-linear, which becomes flattened as n decreases from 1 to 0.6. Since there is no available model to estimate bed shear stress in partially blocked eccentric annulus, dimensionless bed shear stress (Π_{bed}), which compares average bed shear stress with the average wall shear stress is defined as:

$$\Pi_{bed} = \left(\frac{\bar{\tau}_{bed}}{\bar{\tau}_w} \right)^n \quad (3-26)$$

In this study, more focus is given to investigate dependency of dimensionless bed shear stress with other hydraulic parameters such as diameter ratio, bed height and power law index. Based on the method developed by Ahmed et al. (2006), Aworunse (2012) related the shape factor of partially blocked eccentric annulus to diameter ratio, bed height and power law index. Thus:

$$s(n, \kappa, H_{bed}) = \left(\frac{a}{n} + b \right) = \left(\frac{fRe}{2^{3n+1}} \right)^{1/n} \quad (3-27)$$

Appendix B shows correlations developed by Aworunse (2012) to predict geometric parameters. This technique is considered in the present study to develop new hydraulic model for partially blocked highly eccentric annuli. Performance of the new model has been compared with a modified existing model (Chen, 2005), which is developed based on effective diameter concepts (Whittaker, 1985) and adopted to predict pressure loss of power-law fluid in a partially blocked eccentric annulus (Appendix D).

Chapter 4. Computational Fluid Dynamics (CFD)

In this study, Computational Fluid Dynamics (CFD) analysis is used to investigate laminar flow of power law fluids in partially blocked eccentric annulus. Extensive CFD simulations have been performed using FLUENT version 17.1 software developed by ANSYS. Nowadays, FLUENT is widely used software packages for CFD modeling of fluid flow and heat transfer in complex geometries occurring in many industrial applications.

There are two solver options available in FLUENT: pressure-based and density-based. Due to its wide applicability, the pressure-based method, which is suitable for incompressible flow is used in this study. The pressure based-algorithm uses a combination of continuity and momentum equations to derive an equation for pressure (or pressure correction equation). Four types of algorithms are available in FLUENT when choosing pressure-based method: i) SIMPLE (Semi-Implicit Method for Pressure-Linked Equations) method developed by Patankar and Spalding (1972), ii) SIMPLEC (SIMPLE-Consistent) method, iii) PISO (Pressure-Implicit with Splitting of Operators) method, and iv) coupled method. For steady-state calculations, SIMPLE and SIMPLEC are generally used.

This chapter presents the governing equations and the methodology used to obtain numerical solutions. The mesh generation technique is also included. Moreover, the simulation cases are described and organized as matrices.

4.1 Governing Equations

Assumptions and Boundary Conditions

In this study, the following boundary conditions and assumptions are made to perform the CFD simulations:

- The inner pipe is stationary and non-rotating.
- The fluid is homogeneous and flowing under laminar and isothermal conditions.
- The fluid is incompressible and time-independent.
- The annulus is considered horizontal to eliminate the gravitation term in the governing equations.
- No-slip boundary conditions are assumed on solid surfaces within the annulus, i.e. velocities at the inner and outer pipe walls and cuttings bed are zero.
- A constant velocity is applied at the flow inlet (i.e. velocity inlet) and it is calculated from the flowrate and cross sectional area of the physical model.
- Cuttings beds are stationary cuttings and uniformly distributed along the plane.
- End effects are negligible.

Governing Equations

Computational fluid dynamics programs are developed based on the governing laws: i) The law of conservation of mass (continuity equation); ii) Newton's second law of motion (linear and angular momentum equations); and iii) the first law of thermodynamics (energy equation).

For an isothermal, incompressible and laminar flow of a non-Newtonian fluid in an annular space, the governing transport equations are simplified, and the mathematical modeling are performed based on the equations of mass conservation and the balance of

momentum, presented in Cartesian coordinates (without the gravitational effect). First, the simplified equation of the conservation of mass is expressed as:

$$\frac{\partial v_x}{\partial x} + \frac{\partial v_y}{\partial y} + \frac{\partial v_z}{\partial z} = 0 \quad (4-1)$$

Secondly, the momentum equation for each axis is simplified as (Eqns. 4.2 -4.4):

In x -axis:

$$\rho \left(\frac{\partial v_x}{\partial t} + v_x \frac{\partial v_x}{\partial x} + v_y \frac{\partial v_x}{\partial y} + v_z \frac{\partial v_x}{\partial z} \right) = -\frac{\partial p}{\partial x} - \left[\frac{\partial \tau_{xx}}{\partial x} + \frac{\partial \tau_{yx}}{\partial y} + \frac{\partial \tau_{zx}}{\partial z} \right] + \rho g_x \quad (4-2)$$

In y -axis:

$$\rho \left(\frac{\partial v_y}{\partial t} + v_x \frac{\partial v_y}{\partial x} + v_y \frac{\partial v_y}{\partial y} + v_z \frac{\partial v_y}{\partial z} \right) = -\frac{\partial p}{\partial y} - \left[\frac{\partial \tau_{xy}}{\partial x} + \frac{\partial \tau_{yy}}{\partial y} + \frac{\partial \tau_{zy}}{\partial z} \right] + \rho g_y \quad (4-3)$$

In z -axis:

$$\rho \left(\frac{\partial v_z}{\partial t} + v_x \frac{\partial v_z}{\partial x} + v_y \frac{\partial v_z}{\partial y} + v_z \frac{\partial v_z}{\partial z} \right) = -\frac{\partial p}{\partial z} - \left[\frac{\partial \tau_{xz}}{\partial x} + \frac{\partial \tau_{yz}}{\partial y} + \frac{\partial \tau_{zz}}{\partial z} \right] + \rho g_z \quad (4-4)$$

An additional relationship between the stress field and fluid velocity gradient is required, when the fluid is non-Newtonian fluids. Thus, the shear stress of non-Newtonian fluids is related to the shear rate using the power law model (Eqn. 3-2) presented in Section 3. Non-Newtonian fluids viscosity ($\mu(\dot{\gamma})$) is a function of the shear rate $\dot{\gamma}$. Generalized formula for shear rate is expressed as:

$$|\dot{\gamma}|^2 = 2 \left[\left(\frac{\partial v_x}{\partial x} \right)^2 + \left(\frac{\partial v_y}{\partial y} \right)^2 + \left(\frac{\partial v_z}{\partial z} \right)^2 \right] + \left(\frac{\partial v_x}{\partial y} + \frac{\partial v_y}{\partial x} \right)^2 + \left(\frac{\partial v_x}{\partial z} + \frac{\partial v_z}{\partial x} \right)^2 + \left(\frac{\partial v_y}{\partial z} + \frac{\partial v_z}{\partial y} \right)^2 \quad (4-5)$$

Equations from 4-1 through 4-5 are solved by the application of finite volume technique using FLUENT 17.1, which includes a mesh-generating module. Appropriate boundary conditions are applied to obtain numerical solutions to the governing equations.

4.2 Grid System and Sensitivity

Grid generation is the primary step in the CFD simulation process. Formation of cuttings bed in the wellbore makes the annular flow area complex, which complicates grid generation. Considering highly eccentric annulus (90%), computational grids have been generated for different diameter ratios (0.25, 0.5, and 0.75) and dimensionless cuttings bed heights (0, 0.1, 0.3, 0.5, 0.7, 0.9 and 1). Dimensionless bed height is a ratio of actual bed height to the maximum distance between the bottom of outer pipe and the top of the inner pipe, $H_{bed} = H/H_{max}$. Hence, H_{max} is bottom annular clearance plus inner pipe diameter (Fig. 3.9). In each case, the appropriate length (0.0 to 0.45 m.) has been chosen in order to achieve a fully developed laminar flow.

Researchers agree that the accuracy of a CFD simulation results is governed by the number of grids used in the computational model. Too many grids may result in very long computational run time and numerical instability, and very few grids may lead to inaccurate results. In CFD, two approaches are commonly used to effectively discretize complex geometries to solve the governing flow equations numerically. The first approach discretizes the flow domain to a structured mesh (in 3D corresponds to hexahedral or rectangular in 2D), where simple equally spaced Cartesian grids are used. In the second method, unstructured grid system is utilized to subdivide the flow domain (e.g. in 3D: tetrahedral, pyramid, wedge and hybrid cells).

Both structured and unstructured meshes (Figs. 4.1 and 4.2) were generated in this study. Simulation with hexahedral meshes is usually preferred (Fig. 4.1) because it aligns the flow with grids and makes the grids parallel to wall surfaces. However, for more complex geometries (i.e., buried pipe), hexahedral mesh becomes difficult to generate.

Therefore, unstructured grid method is often preferred. Among different types of unstructured meshing techniques, tetrahedral (with and without inflation layers) and hybrid (i.e., cutcell) meshing methods are used in ANSYS FLUENT. Different types of unstructured grid systems are shown in Fig. 4.2. Cutcell Cartesian meshing is a general meshing method used in ANSYS FLUENT. Cutcell meshing is suitable for a large range of applications. Due to the large fraction of hexahedral elements (about 90%) present in the mesh, the cutcell meshing often produces better and very quick results when compared to tetrahedral meshing. It is important to mention that due to the symmetrical nature of annular flows, each flow simulation has been carried out using only a half section of the model.

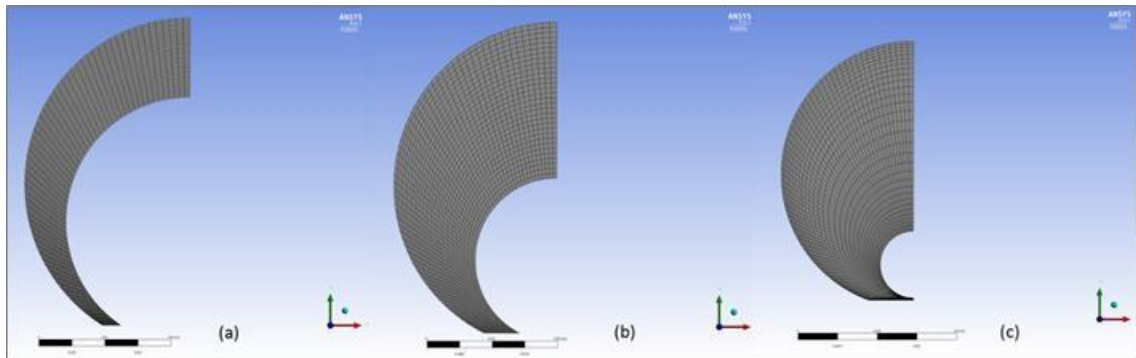


Figure 4.1 Hexahedral mesh: (a) $\kappa=0.75$; (b) $\kappa=0.5$; and (c) $\kappa=0.25$ ($e=0.9$, $H_{bed}=10\%$)

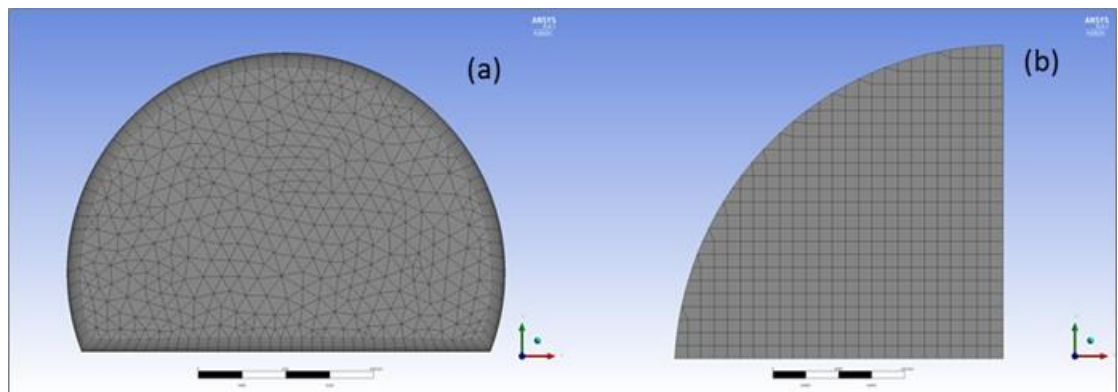


Figure 4.2 Unstructured meshes: (a) tetrahedral with boundary layers; and (b) cutcells ($\kappa=0.5$, $e=0.9$)

Grid Independency Study

In this study, grid sensitivity analysis has been conducted for partially blocked eccentric annuli. To illustrate the adequacy of mesh refinement in the grids, mesh dependency studies have been performed for two different meshing techniques (hexahedral and cutcell meshing methods). The 3D hexahedral meshes have been used to represent a partially blocked eccentric annulus with 30% bed height (Table 4.2).

Table 4.1. Input parameters for grid size sensitivity analysis

Parameter	Value
Drillpipe Diameter, D_i (m)	0.025
Casing Diameter, D_o (m)	0.05
Relative Eccentricity, e	0.9
Dimensionless Bed Height, (% H_{bed})	30
Fluid Density (kg/m^3)	1000
Consistency Index, ($\text{Pa}\cdot\text{s}^n$)	1
Fluid Behavior Index, n	1
Boundary Condition, Q (m^3/s)	5×10^{-5}

For grid independence test, different mesh sizes (21 x 13; 30 x 20; 40 x 20; 45 x 23; 61 x 31; and 79 x 31) have been considered. An element size of 0.002 m for the z -axis length is also adjusted in the meshes. Figures 4.3, 4.4, and 4.5 illustrate the pressure drop, hydraulic parameter fRe and dimensionless bed shear stress obtained from CFD as functions of number of grids used in computational procedure. Analyzing the results of the different cases, meshes with more than 1000 grids in the x - y plane provide reasonably accurate results with optimum computational time. As a result, in this study, grid size of 61 x 31 has been used to create grid structure in the annulus. Grid element length of 0.002

meter has been used in the z-axis, which result in generation of 425,476 grids to simulate the flow in the annulus. For this analysis, length of the annulus has been fixed to 0.45 m.

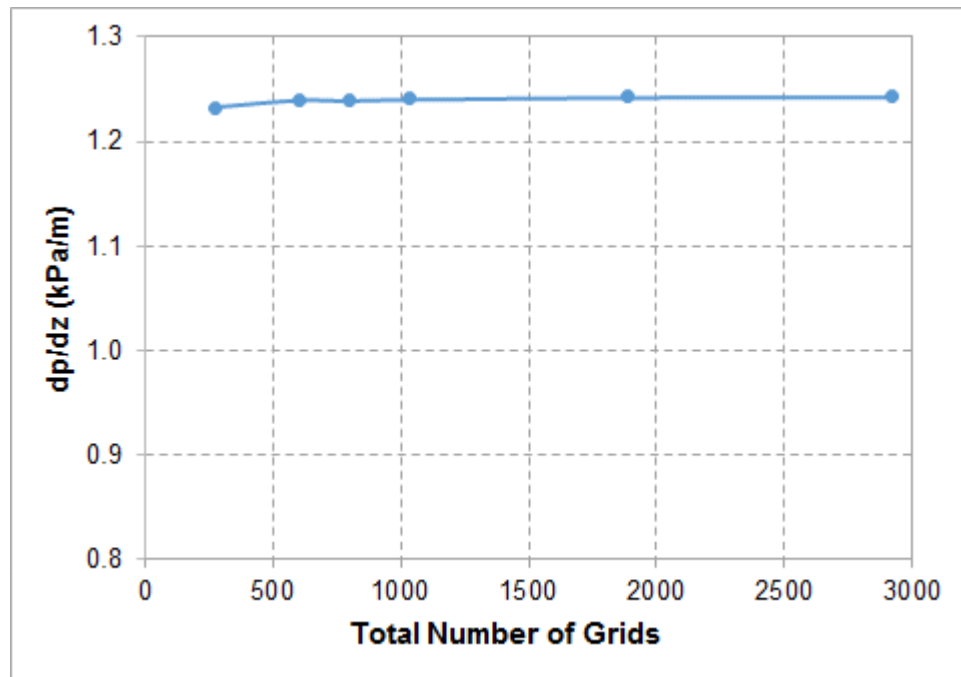


Figure 4.3 Grid size independency of pressure drop. Structured mesh

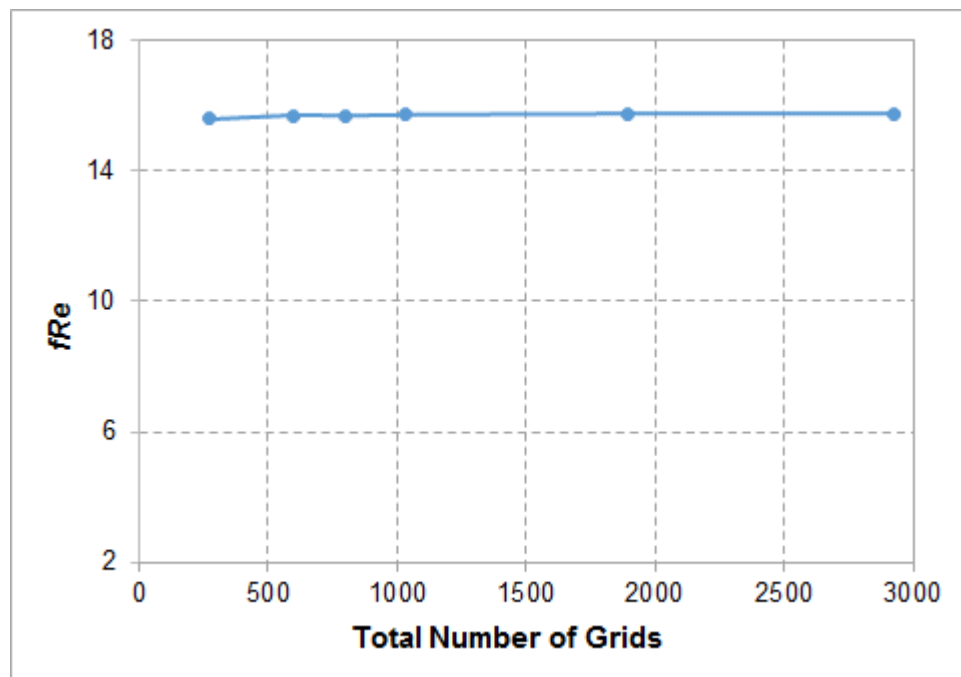


Figure 4.4 Grid size independency of fRe . Structured mesh

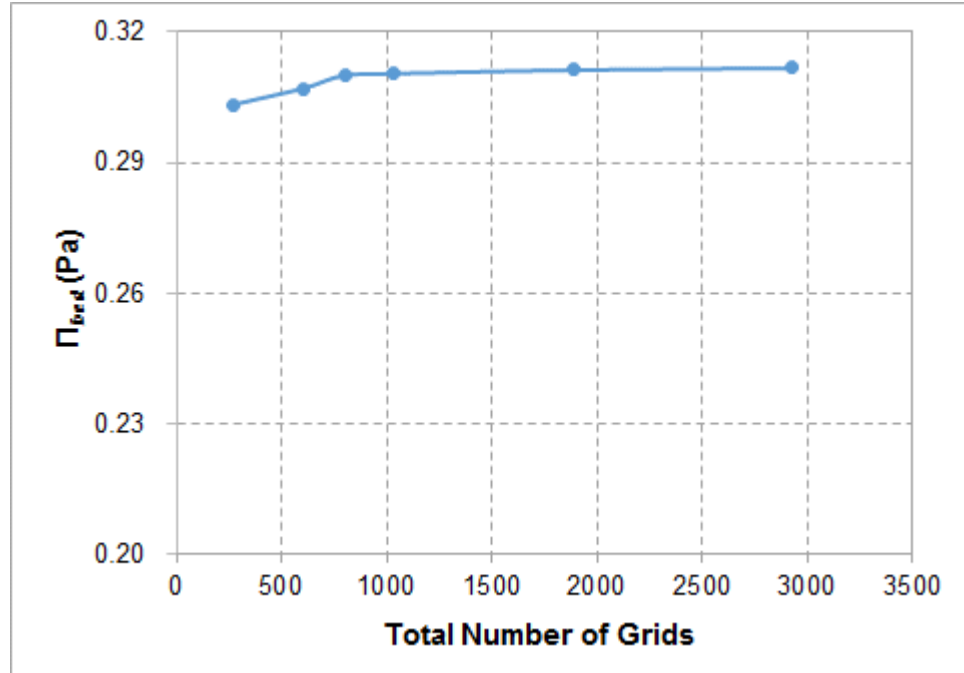


Figure 4.5 Grid size independency of Π_{bed} . Structured mesh

Before proceeding with the second sensitivity test, a comparison between the tetrahedral and cutcell unstructured meshes was made in terms of the mesh metrics. The results of the comparison have helped to select the most suitable option to perform the sensitivity test. The mesh metric values obtained from the mesh generation can be observed in Table 4.3. The cutcell mesh metrics values are closer to the recommended values (e.g. skewness = 0.02 for cutcell, whereas skewness = 0.23 for tetrahedral) when compared with tetrahedral meshing, providing a better mesh quality. Therefore, this indicates that cutcells with unstructured meshes are suitable to model irregular geometries, when hexahedral meshes are difficult to generate (i.e., when the pipe is fully buried).

Table 4.2 Mesh metrics for unstructured meshes (100% H_{bed} and $\kappa = 0.5$)

Mesh Metric (average)	Tetrahedral mesh (+inflation layers)	Cutcell Assembly Mesh	Recommended
Skewness	0.233	0.02	~0
Aspect Ratio	9.900	1.08	1-20
Element Quality	0.513	0.99	~1
Orthogonal Quality	0.870	0.99	~1

The second mesh sensitivity analysis has been performed with 3D cutcell meshing for the case the inner pipe is fully buried. The input parameters are similar to those summarized in Table 4.2, except the dimensionless bed height, which is set 100% in this case. For this analysis, three uniform grid sizes (0.0005, 0.001, and 0.002 m) have been adopted. Therefore, Table 4.4 presents the results for the hybrid mesh, where a size of 0.001 m provides reasonable results with optimum computational time.

Table 4.3 Results obtained using unstructured cutcell meshing

Mesh size (m)	Cells	Pressure Drop (pa/m)	Iterations for Convergence
0.0020	42,884	1,985.0	188
0.0010	304,612	2,006.1	516
0.0005	2,336,688	2,011.5	1557

4.3 CFD Simulation

4.3.1 Set up and Post-Processing

Following the grid sensitivity analysis, the physical model has been defined and boundary conditions have been specified to perform the simulations. Fixed fluid density (1000 kg/m³) has been used for the simulation. Base case simulations have been

performed for power-law fluid with consistency index of 1.0 pa.sⁿ. To avoid singularity problem in apparent viscosity function, critical shear rate ($\dot{\gamma}_c$) has been determined. The program uses a hybrid apparent viscosity function in which a low shear rate zone is defined as a region with shear rate value of less than a critical shear rate ($\dot{\gamma}_c$). The hybrid apparent viscosity function is expressed as (ANSYS FLUENT, 2015):

$$\mu = \frac{\tau_0}{\dot{\gamma}} + K \left(\frac{\dot{\gamma}}{\dot{\gamma}_c} \right)^{n-1} \quad \text{for } \dot{\gamma} > \dot{\gamma}_c \quad (4-6)$$

$$\mu = \tau_0 \frac{(2-\dot{\gamma}/\dot{\gamma}_c)}{\dot{\gamma}_c} + K \left((2-n) + (n+1) \frac{\dot{\gamma}}{\dot{\gamma}_c} \right) \quad \text{for } \dot{\gamma} \leq \dot{\gamma}_c \quad (4-7)$$

In this study, the critical shear rate has been selected based on the nominal Newtonian shear rate ($(8U/D_{hyd})$) in order to obtain accurate results. Therefore, sensitivity analysis has been conducted to obtain reasonable value of critical shear rate. According to the results, critical shear rate value of 1% of the nominal Newtonian shear rate is used. Simulation were performed at constant flow rate of $5 \times 10^{-5} \text{ m}^3/\text{s}$.

In this investigation, the simulations have been performed for laminar flow using Semi-Implicit Pressure Linked Equations (SIMPLE) scheme for pressure-velocity coupling. However, the second order scheme is employed for pressure discretization. SIMPLE algorithm is preferred because of its simplicity in resolving incompressible flow problems. For the discretization of the momentum equation components, second order discretization schemes would result in good accuracy. The convergence criteria for the z-velocity residuals was 1×10^{-7} and 10^{-3} for the continuity residual. Additionally, in order to reduce computational error (i.e. difference between successive solution), maximum iteration step value of 9000 has been used to ensure numerical convergence.

In the post-processing step, the converged solutions are examined visually and numerically to obtain information on key flow features, such as velocity, wall shear stress, and pressure drop profiles are smooth and consistent. For each case, the flow path was divided into two cross-sectional views (x - y planes), one view in the middle along the length, and another one close to the outlet in order to visualize velocity contours. Moreover, plots of axial velocity and pressure gradient on a streamline (along the z -axis) are generated to observe the length of the computational domain required to ensure full development of the velocity profile and establishment of the steady state flow condition. Thus, Fig. 4.6 illustrates establishment of constant velocity profile and pressure gradient along the axial direction, which indicates establishment of a fully developed steady state flow condition.

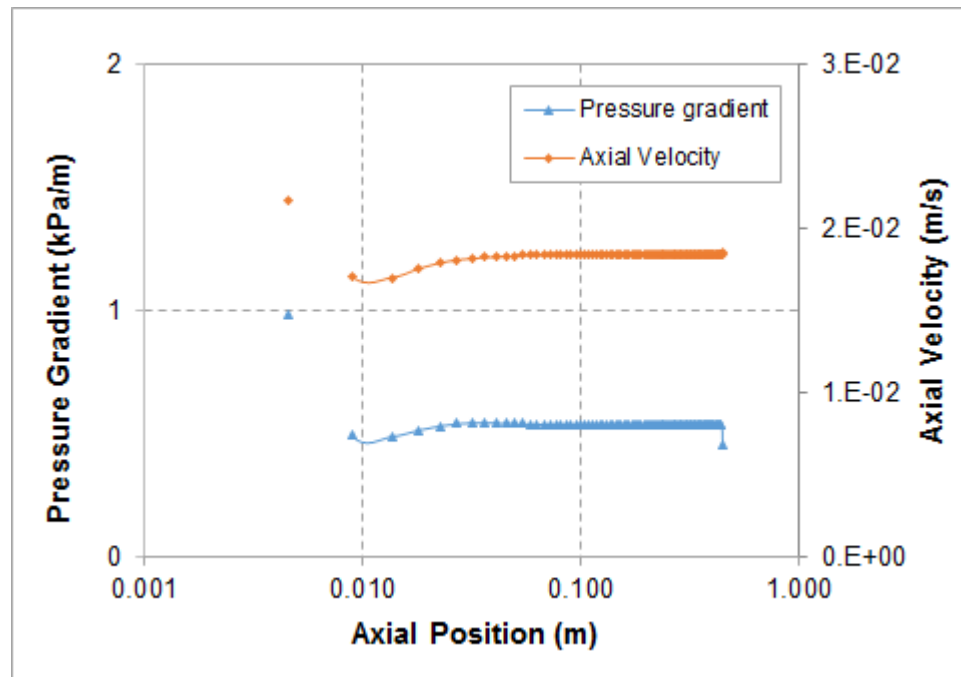


Figure 4.6 Pressure gradient and axial velocity along a partially blocked eccentric annulus

$$(e=0.9, \kappa=0.5, n=1, H_{bed}=10\%, Q = 5 \times 10^{-5} \text{ m}^3/\text{s})$$

4.3.2 Matrix

Matrices of simulation cases were developed to achieve the objectives described in Chapter 1. Table 4.5 shows that for a diameter ratio of 0.75, seven cases of dimensionless bed heights have been considered for each power law index. Due to the limitations of the program, 10% bed height is the minimum bed height adopted in this study to generate structured meshes with a dimensionless eccentricity of 90%. Since the power law index varies from 0.2 to 1, for one diameter ratio, 35 simulations have been performed. Similarly, other matrices have been created for diameter ratios of 0.5 and 0.25 (presented in Appendix C). Accordingly, 105 cases have been simulated in this study.

Table 4.4 Matrix simulation. Diameter ratio 0.75

$D_i/D_o = 0.75$					
n H/H_{max}	0.2	0.4	0.6	0.8	1
0	Sim 1	Sim 2	Sim 3	Sim 4	Sim 5
0.1	Sim 6	Sim 7	Sim 8	Sim 9	Sim 10
0.3	Sim 11	Sim 12	Sim 13	Sim 14	Sim 15
0.5	Sim 16	Sim 17	Sim 18	Sim 19	Sim 20
0.7	Sim 21	Sim 22	Sim 23	Sim 24	Sim 25
0.9	Sim 26	Sim 27	Sim 28	Sim 29	Sim 30
1.0	Sim 31	Sim 32	Sim 33	Sim 34	Sim 35

The numerical simulations were carried out on a super computer equipped with 2 GHz intel® Xeon ® CPU PC with 2 processors, 16 GB of RAM memory and 64-bit operating system executed on 16 computational cores. Each simulation case generates about 500,000 cells, equivalent to one GB of total memory (IBM, 2012). The run time, for an example, to reach 1500 iteration is about 30 min. However, the run time depends

on the size of the geometry and the type of fluid (shear thinning fluids take more time to converge).

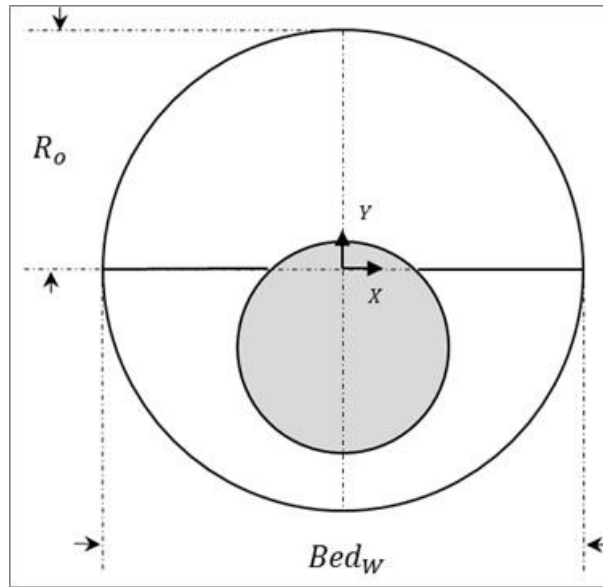


Figure 4.7 X and Y dimensionless coordinates

Velocity profile and bed shear stress distribution on x - y plots are represented through the use of the following dimensionless coordinates (X and Y):

$$X = \frac{x}{0.5Bed_w} \quad (4-8)$$

$$Y = \frac{y}{R_o} \quad (4-9)$$

x and y are x and y axis, respectively. Bed_w corresponds to bed width as it can be observed in Fig. 4.7.

4.3.3 CFD Verification

In order to verify the accuracy of CFD simulation, pressure drop and other hydraulic parameters are compared with available experimental data, and analytical and numerical solutions reported in the literature.

CFD simulation predictions were compared with measurements (George, 2012) obtained from large-scale flow loop experiments conducted to study hole cleaning performance of synthetic-based (SBM). The experiments provided equilibrium bed height and frictional pressure loss measurements in the annulus at different flow rates (Table 4.5). George (2012) performed experimental investigations in a fully eccentric annulus. The experimental setup has a horizontal 4”x 2” (101.6 mm x 50.8 mm) annular test section, which simulates cuttings transport in horizontal wellbore with 8/16 mesh sand particles. For different flowrates, equilibrium bed height and pressure loss measurements were obtained (Table 4.5). Power law parameters of test fluid are presented in Table 4.6.

Table 4.5 Volumetric flow rate and stationary bed height

Fluid: SBM		
Q (m³/s)	H(m)	H/D_o (%)
0.0006	0.069	67
0.0013	0.065	64
0.0019	0.062	61
0.0032	0.047	46
0.0038	0.039	39
0.0044	0.028	28

Table 4.6 Modified non-Newtonian power law density and rheological parameters

Fluid	Type	Density (kg/m³)	K,	n
			(Pa.sⁿ)	
SBM	PL	1240	2.38	0.34

In addition to the validation with experimental results, simulation results are compared with analytical (Piercy et al., 1933) and numerical (Fang et al., 1999) results for eccentric annuli reported in the literature. The results are presented in Section 5.

4.3.4 Hydraulic and Geometric Parameters Sensitivity Analysis

For power-law fluids, the product of Fanning friction factor Reynolds number (fRe) is a function of flow geometry (eccentricity and diameter ratio) and power law index (Fang et al., 1999). Moreover, dimensionless bed shear stress is found to be a function of flow geometry and power law index. To revalidate these observations, sensitivity analysis is performed in order to better understand the effect of rheological properties (consistency index and power law index) on the fRe , and the dimensionless bed shear stress in a partially blocked annulus. Furthermore, sensitivity tests are performed to evaluate the influence of fluid velocity and Reynolds number on these parameters.

Table 4.7 presents a summary of the input parameters used to perform the first batch of CFD simulations, at a constant flowrate varying consistency index from 0.001 to 20 $\text{pa}\cdot\text{s}^n$, and power law index from 0.2 to 1.

Table 4.7 Input parameters used in sensitivity analysis

Parameter	Value
Diameter ratio, κ	0.5
Relative Eccentricity, e	0.9
Dimensionless Bed Height, % H_{bed}	10
Fluid density (kg/m^3)	1000
Consistency Index, K ($\text{Pa}\cdot\text{s}^n$)	0.001 to 20
Fluid Behavior Index, n	0.2 to 1
Boundary Condition, Q (m^3/s)	1×10^{-4}

Figure 4.8 presents the parameter fRe as a function of the consistency index for different power law indices. As previously mentioned in the literature, the friction factor Reynolds number product remains constant as the consistency index increases. However, as the consistency index decreases below $0.1 \text{ Pa}\cdot\text{s}^n$, the fRe substantially increases. This is due to the inherent instability of the program at low consistency index values. Moreover, as the fluid becomes highly shear thinning, the parameter fRe decreases significantly.

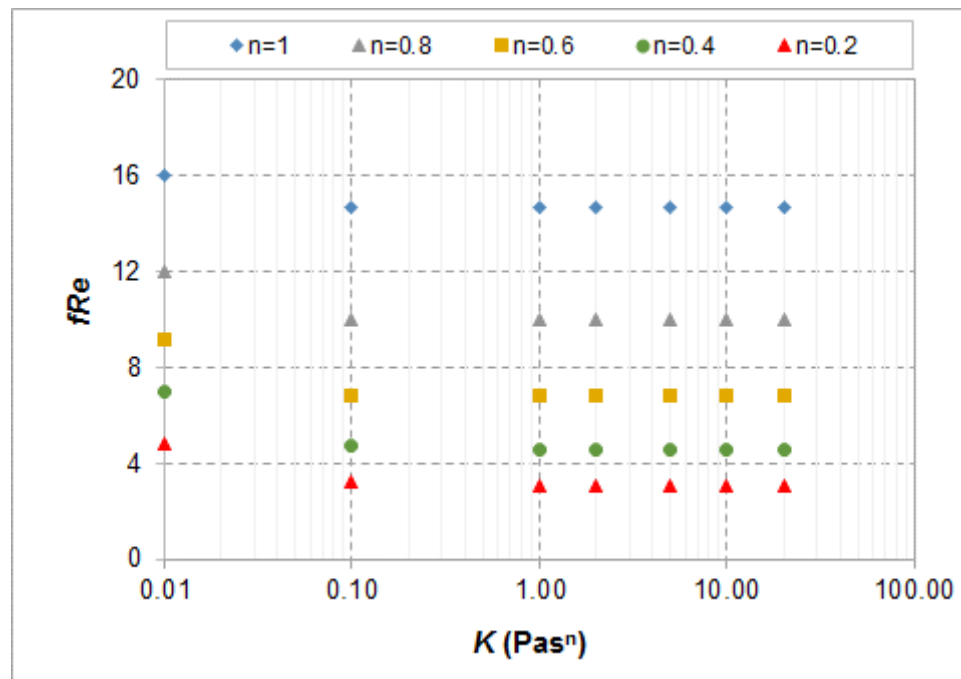


Figure 4.8 fRe vs. fluid consistency index ($H_{bed} = 10\%$, $Q = 1 \times 10^{-4} \text{ m}^3/\text{s}$)

Sensitivity results obtained in terms of the dimensionless bed shear stress parameter (Fig. 4.9) show similar trends when compared with Fig. 4.8. The parameter Π_{bed} remains constant when the consistency index increases from 0.1 to $20 \text{ Pa}\cdot\text{s}^n$.

However, when the consistency index decreases below 0.1 Pa·sⁿ, the dimensionless parameter increases due to numerical instability which causes inaccuracy. The effect of fluid shear thinning behavior on the parameter Π_{bed} is substantial. With increase in shear thinning, the parameter increases due to reduction in wall shear stress, which occurs because of shear thinning.

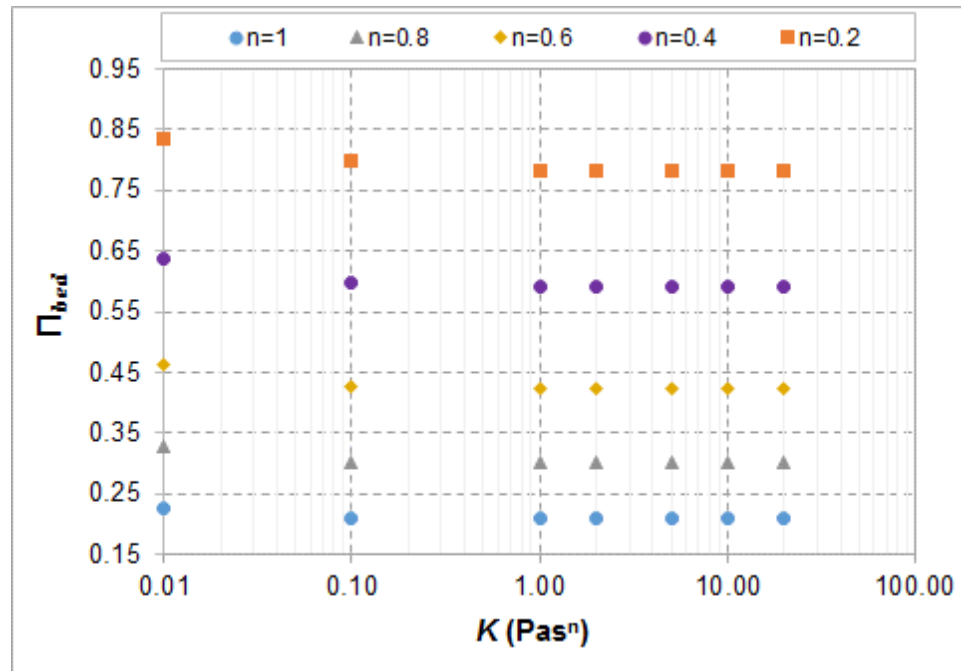
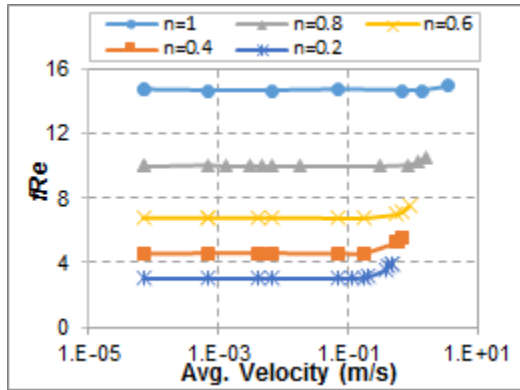


Figure 4.9 Π_{bed} vs. fluid consistency index ($H_{bed}=10\%$, $Q=1 \times 10^{-4} \text{ m}^3/\text{s}$)

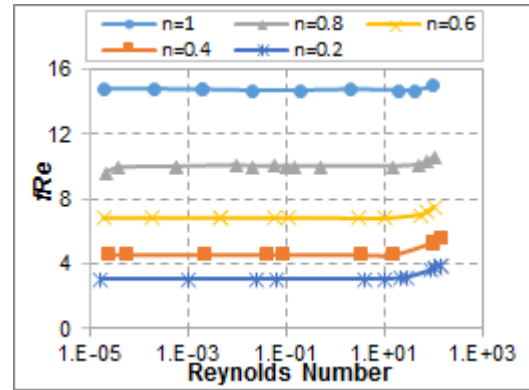
Furthermore, the effects of mean fluid velocity and Reynolds number on dimensionless parameters fRe and Π_{bed} are investigated considering the same flow rate in a partially obstructed annular section. Figure 4.10 presents results of CFD simulations conducted varying these two variables. According to Fig. 4.10 (a), Newtonian fluids reflect a wide range of velocity values (between $7 \times 10^{-5} \text{ m/s}$ and 1.5 m/s), where the parameter fRe remains constant; however, for shear thinning fluids ($n = 0.2$), the fRe is

constant for a narrow range of velocities due to numerical instability. The same pattern can be observed when Reynolds Number is varied, Fig. 4.10 (b), where for Newtonian fluids the Re range is between 0.002- 40, while for shear thinning fluids ($n=0.2$) the range is reduced (0.066-30.55).

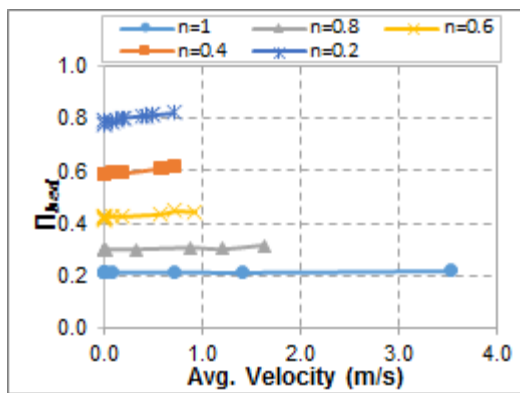
For Newtonian fluids, results (Fig. 4.10c) show constant Π_{bed} value for wide range of velocities and Reynolds numbers. However, as the shear thinning characteristic of the fluid increases (i.e. the value of n decreasing from 0.6 and 0.2), the dimensionless bed shear stress becomes constant for small average velocity ranges. For Reynolds numbers less than 100 (Fig. 4.10d), the dimensionless bed shear stress remains constant. It can be concluded that the simulation should be performed to small velocities (or small Reynolds numbers) in order to maintain numerical stability.



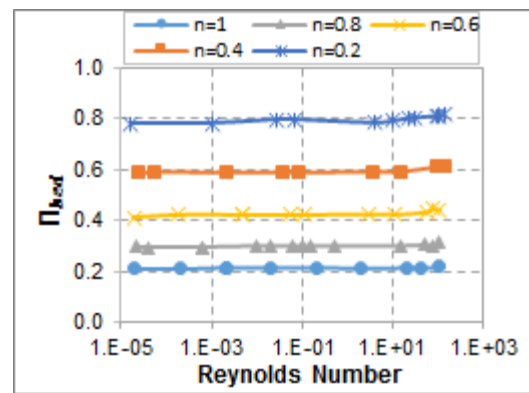
(a)



(b)



(c)



(d)

Figure 4.10 Hydraulic parameters: (a) fRe vs. avg. velocity; (b) fRe vs. Re ; (c) Π_{bed} vs. avg. velocity; and (d) Π_{bed} vs. Re

Chapter 5. Results and Discussion

This section presents results of validation studies and CFD simulations, Moreover, it shows analysis and interpretation of CFD simulation results demonstrating the effect of different hydraulic parameters on pressure loss, fRe , and wall shear stress in partially blocked annulus.

5.1 Numerical Verification

5.1.1 Comparison of CFD Simulation with Experimental Data

Figure 5.1 compares measured and CFD predicted pressure losses, for a SBM fluid, considering different bed heights and a fully developed laminar flow. As illustrated in Fig. 5.1, predictions show good agreement with experimental values for high flowrates (above $0.032 \text{ m}^3/\text{s}$), where the majority of the predictions are within $\pm 17\%$. On the other hand, a slightly higher discrepancy (within 28%) is observed at low flowrates. This is because the inner pipe is completely buried at low flowrates (less than $0.032 \text{ m}^3/\text{s}$), generating fine grids, and making the simulation more difficult to converge.

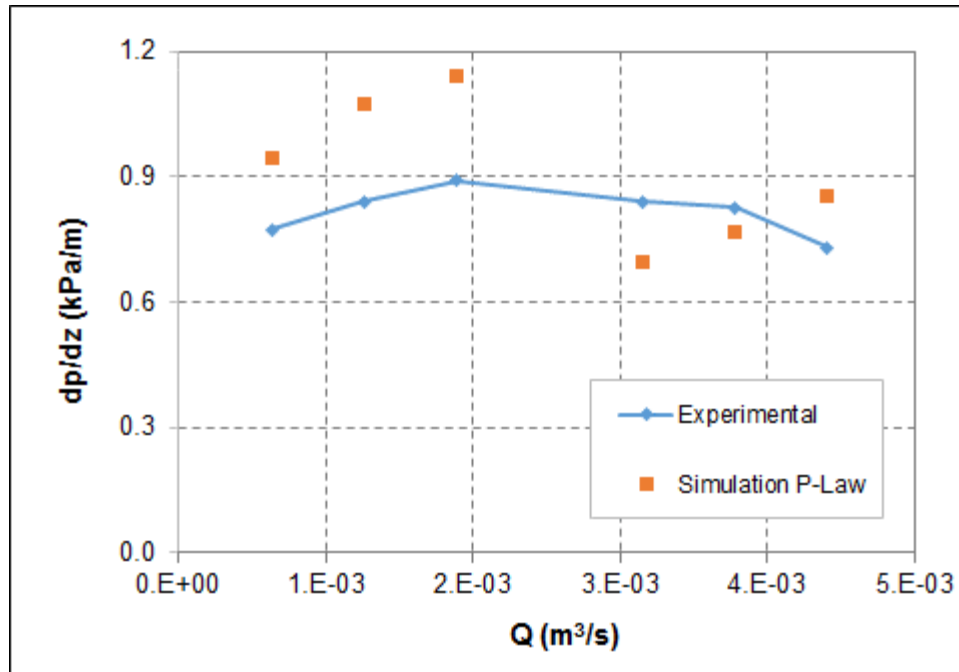


Figure 5.1 Measured and CFD predicted pressure gradients vs. flowrate (SBM Fluid, data from George 2012)

5.1.2 Comparison of CFD Model with Analytical and Numerical Solutions

In addition to experimental data, CFD simulation results are compared with the analytical solution (Eqn. 3.29) developed for Newtonian fluids (Piercy et al. 1933). Figure 5.2 compares analytical solution with CFD simulation results for different diameter ratios (0.25, 0.5 and 0.75). The simulation results demonstrate excellent agreement with the analytical solution. The maximum discrepancy is 1.2 %.

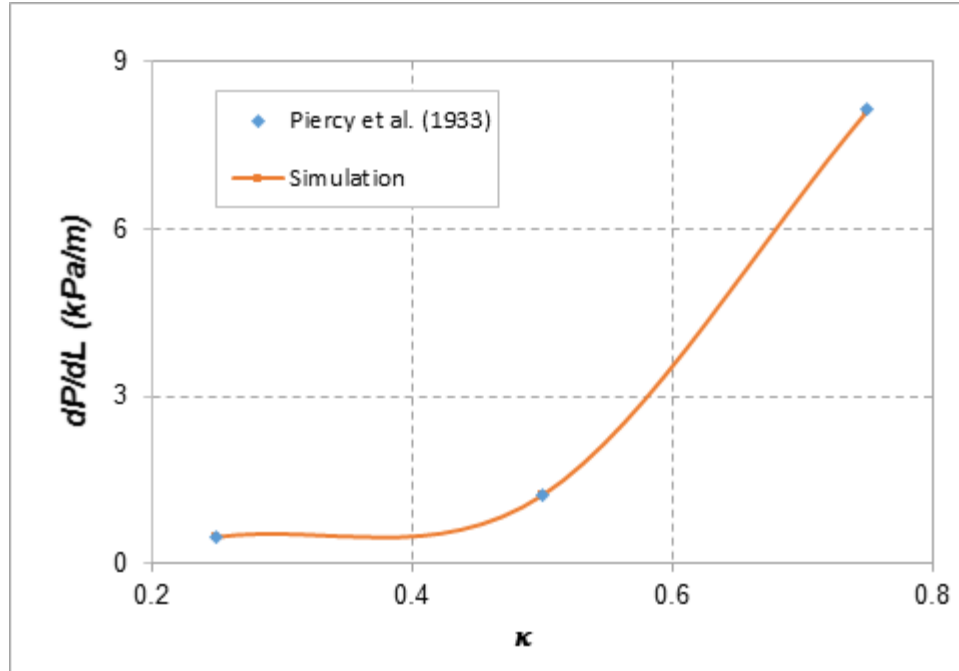


Figure 5.2 Comparison of predictions of CFD simulation and analytical model for dimensionless eccentricity of 0.9 ($Q = 5 \times 10^{-5} \text{ m}^3/\text{s}$)

The fRe values reported by Fang et al. (1999) for eccentric annulus are for diameter ratios of 0.2, 0.5 and 0.8, eccentricities from 0 to 0.8, and power-law fluids from $n = 0.2$ to 1 (Fig. 3.2). Since the present work modeled eccentric annulus with a dimensionless eccentricity of 0.9, and no exact analytical solution exists for non-Newtonian flow, hydraulic parameter fRe reported by Fang et al. (1999) is interpolated and used to validated CFD simulation results at different diameter ratios (0.25, 0.50 and 0.75) and power law indices (1, 0.8, 0.6, 0.4 and 0.2). Figures from 5.3 to 5.5 compare interpolated values with CFD simulation data. Results show good agreement between the simulated results and interpolated values. A maximum discrepancy of 7% is observed when $\kappa = 0.75$ and $n = 0.2$. It is important to mention that for Newtonian fluids ($n =$

1), better agreement is obtained with analytical solutions (Piercy et al., 1933) than the interpolated fRe values from Fang et al. (1999).

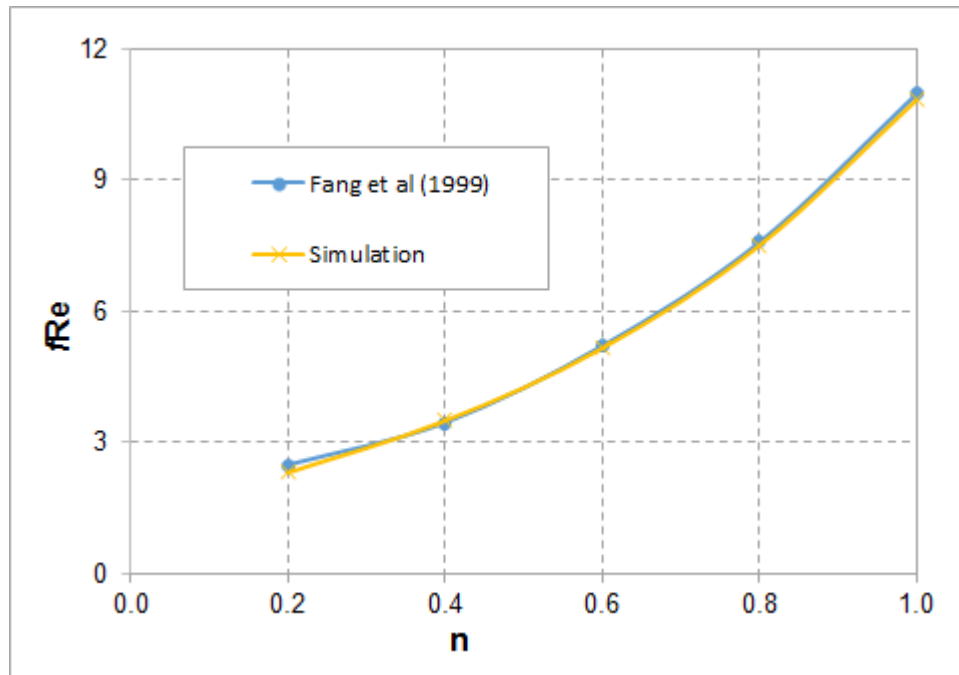


Figure 5.3 Hydraulic parameter fRe vs. n for $\kappa=0.75$, $e=0.9$, and $Q = 5 \times 10^{-5} \text{m}^3/\text{s}$

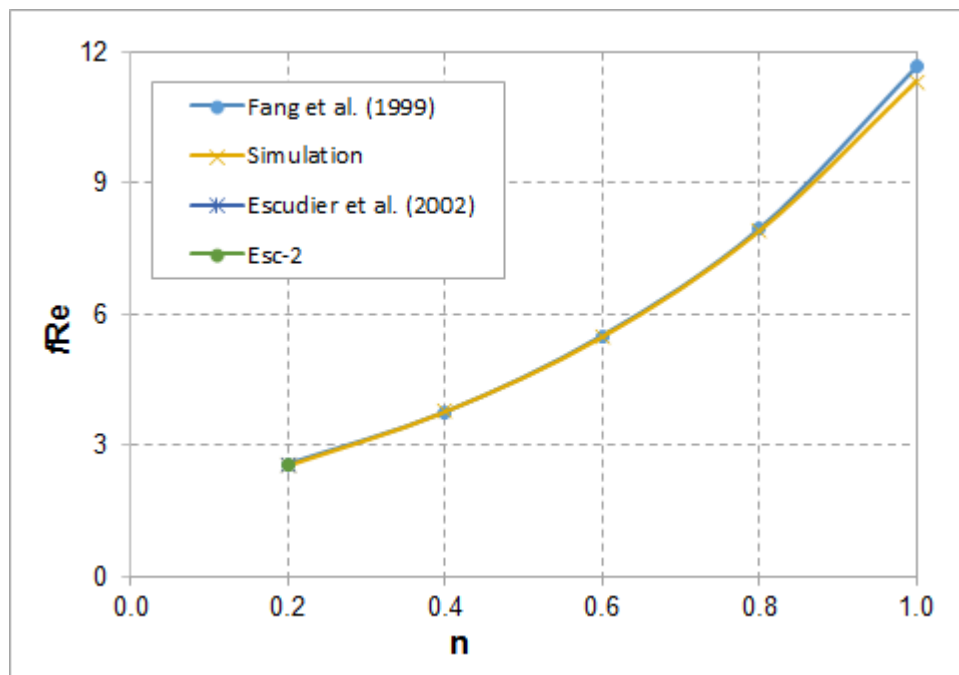


Figure 5.4 Hydraulic parameter fRe vs. n for $\kappa=0.50$, $e=0.9$, and $Q = 5 \times 10^{-5} \text{m}^3/\text{s}$

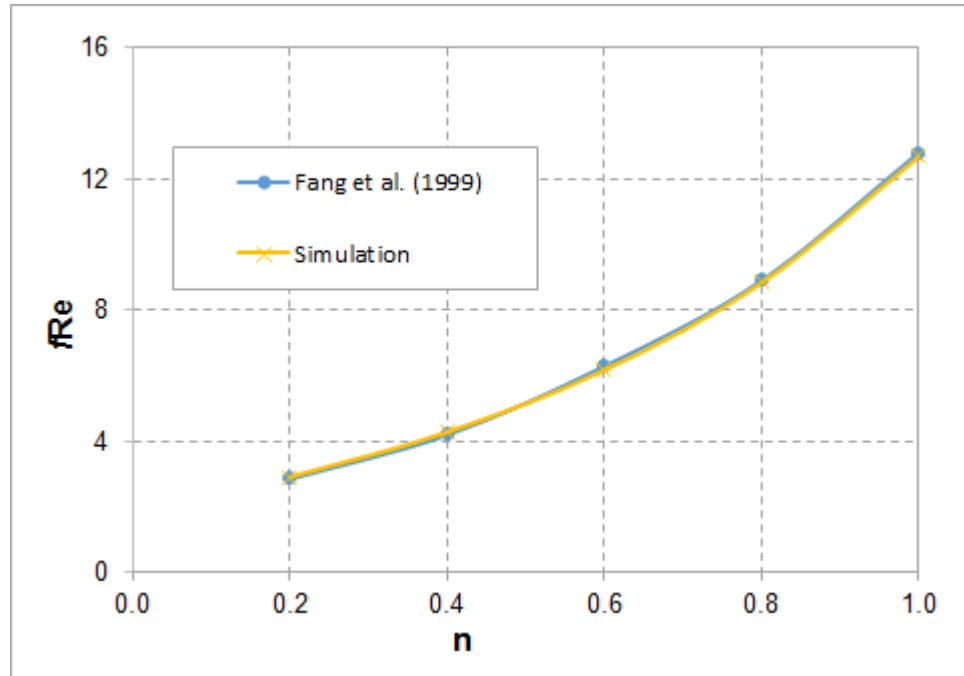


Figure 5.5 Hydraulic parameter fRe vs. n for $\kappa=0.25$, $e=0.9$, and $Q = 5 \times 10^{-5} \text{m}^3/\text{s}$

5.2 Effect of Cutting Build Up within the Annulus

In order to predict the effect of cuttings bed build on pressure loss, simulations have been carried out varying the dimensionless bed thickness from zero to 100% (i.e. bed height that can completely bury the drill pipe) for 90% eccentric annuli. The simulations have been performed for diameter ratios ranging from 0.25 to 0.75. A 0.05-m diameter hole is considered for this analysis. Rheological parameters and boundary conditions adopted are described in Section 4.3.1. The drillpipe radius is adjusted based on the annular diameter ratio. The effects of bed buildup on pressure drop and hydraulic parameters are presented as follows.

5.2.1 Annular Frictional Pressure Loss

The effect of cuttings bed builds up on annular pressure loss is examined maintaining a constant flow rate (Figs. 5.6 through 5.8). As expected, the pressure loss has increased with cuttings bed thickness. However, at low bed height (below 40% of bed height), the increase in pressure loss is minimal. Moreover, the effect of flow behavior index on pressure loss is more evident. As the shear thinning behavior of the fluid increases, the pressure loss substantially decreases. Furthermore, the Figs. illustrate that as the diameter ratio decreases, the pressure loss decreases substantially. The reason of this reduction is the increase in annular clearance, which increases flow area and makes the pressure loss to decrease considerably.

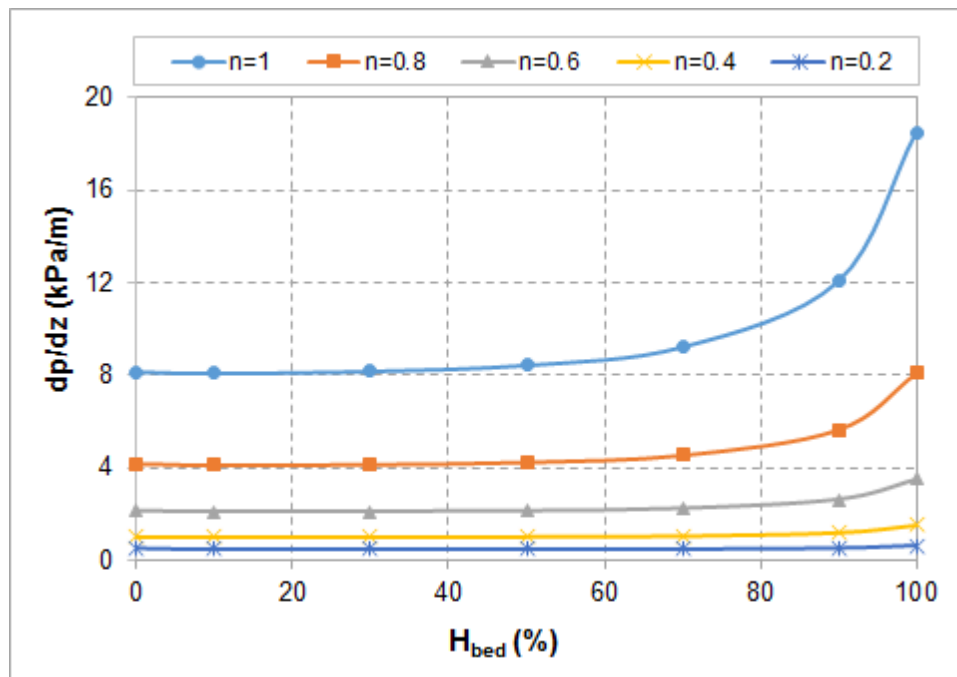


Figure 5.6 Pressure loss vs. % dimensionless bed height ($\kappa=0.75$, $e=0.9$ and $Q = 5 \times 10^{-5}$ m³/s)

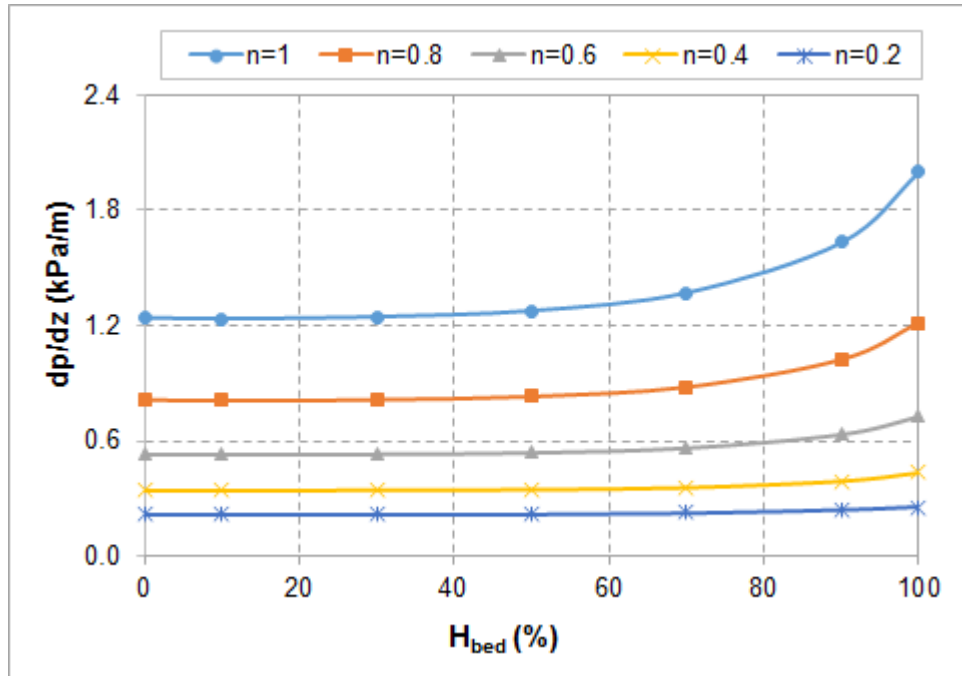


Figure 5.7 Pressure loss vs. % dimensionless bed height ($\kappa=0.50$, $e=0.9$ and $Q = 5 \times 10^{-5}$

m^3/s)

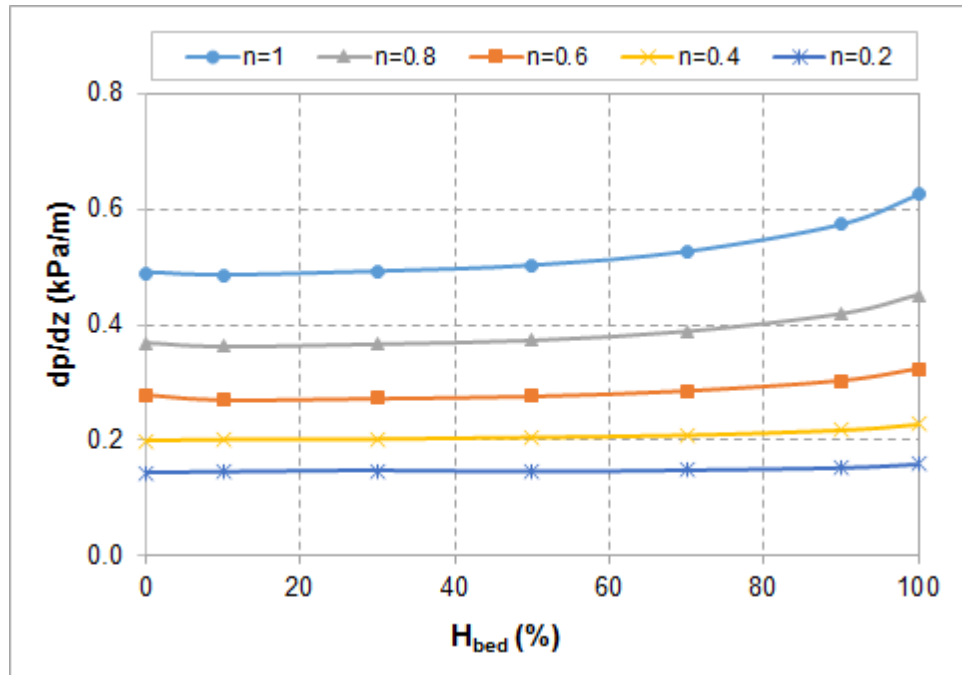


Figure 5.8 Pressure loss vs. % dimensionless bed height ($\kappa=0.25$, $e=0.9$ and $Q = 5 \times 10^{-5}$

m^3/s)

Increase in frictional pressure loss is expected as cuttings bed thickness increases. This is due to flow restriction caused by the bed, reducing the flow cross-sectional area. In drilling operations, if the friction pressure continuously increases due to bed development, the bottom hole pressure can increase excessively, resulting in drilling problems such as fluid loss, lost circulation and well control. Therefore, accurately predicting friction pressure loss can considerably avoid these problems.

5.2.2 Axial Velocity Profiles

Velocity contours in partially blocked 90%-eccentric annuli are presented in Fig. 5.9. Stagnant fluid zones are observed in the narrow parts of the annuli. With increasing the cuttings bed height, the velocities in the wide parts of the annuli increase, whereas the velocities in the narrow parts decrease significantly. Evidently, this behavior is expected since the flow resistance decreases in the wide part, resulting in high fluid velocity. In directional drilling operations, this situation favors formation of cuttings bed due to low fluid velocity in stagnant zones. The velocity contours for diameter ratios 0.25 and 0.75 are presented in Appendix E.

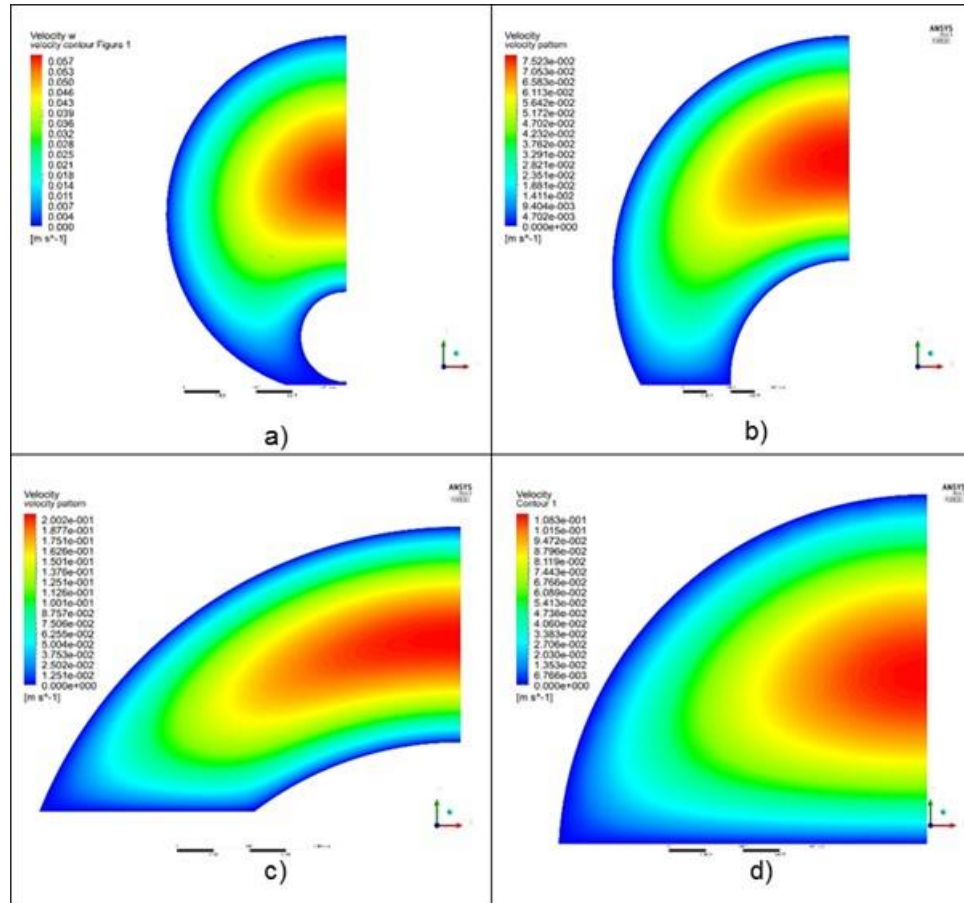


Figure 5.9 Velocity distributions in partially blocked annuli ($n=1$, $\kappa=0.50$, $e=0.9$ and $Q = 5 \times 10^{-5}$ m³/s): (a) $H_{bed}=0\%$; (b) $H_{bed}=30\%$; (c) $H_{bed}=70\%$; and (d) $H_{bed}=100\%$

Figure 5.10 shows effect of shear thinning on axial fluid velocity. for a partially blocked annulus ((30% H_{bed} , $\kappa = 0.75$). Y is the dimensionless vertical distance from the center, which is defined in Eqn. 4.7. As power-law index varies from 1 to 0.2 at a constant flowrate, the velocity profile gets flatter. Similar velocity profile patterns (Appendix E) have been observed with other diameter ratios (0.5 and 0.25).

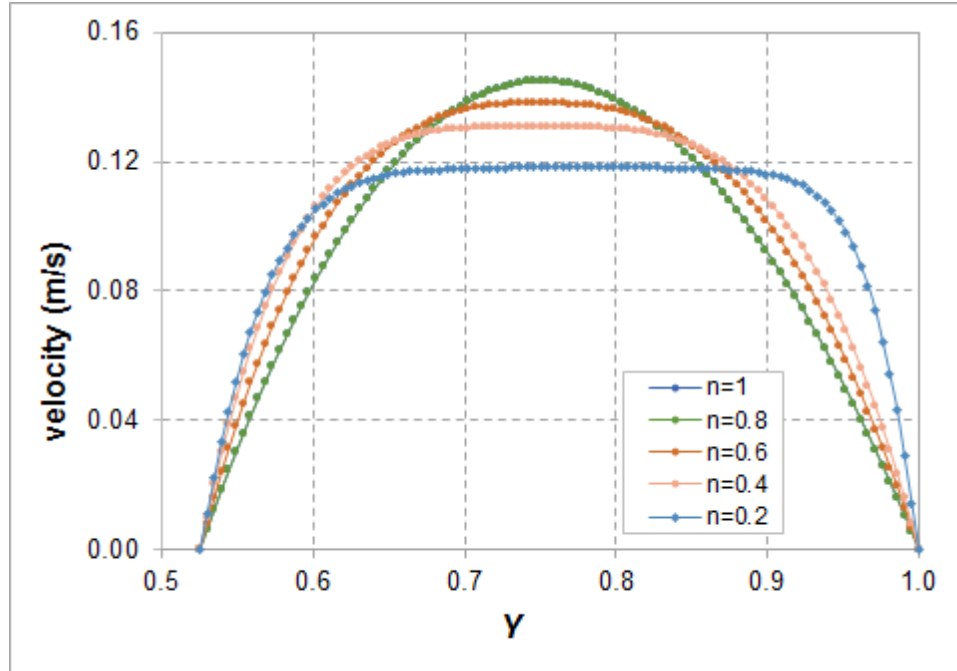


Figure 5.10 Velocity profile vs. Y ($H_{bed}=30\%$, $\kappa=0.75$, $e=0.9$ and $Q = 5 \times 10^{-5} \text{ m}^3/\text{s}$)

5.2.3 Hydraulic Parameter fRe

Figures 5.11 and 5.12 illustrate the fRe values obtained from CFD simulation of partially blocked annuli. Trends of the parameter fRe are very similar for diameter ratios of 50% and 75%. At low bed heights (approximately less than 60%), the parameter fRe increases with bed thickness. The increase in the parameter is more pronounced when the annular diameter ratio is high (i.e. 75%). At high bed heights (approximately greater than 40%), the fRe values show moderate reduction with bed height. The fRe trend with bed height is slightly different for low diameter ratio annulus (Fig. 5.13). At low bed heights (less than 10%), fRe displays slight reduction with bed height. This trend reverses when the bed height is approximately more than 10%. The parameter slightly increases with bed height up to 50% and then it stabilizes. One possible explanation for the trend reversal at 10% bed height could be the location of the bed height in relation to the inner

pipe. The fRe reaches its minimum when the bed approaches the bottom of the inner pipe. The velocity profiles in the y-direction for partially blocked eccentric annulus ($\kappa = 0.25$) is illustrated in Fig. 5.16, in order to demonstrate the fRe reduction for Newtonian and shearing fluids (i.e. $n = 1$ and $n = 0.2$). In addition, the figure compares the velocity profiles of two cases with different bed heights ($H_{bed} = 0\%$ and $H_{bed} = 10\%$). Even though the axial velocity profiles in the wide part of both cases are similar, the velocity profile in the narrow section is different. In the narrow gap, local velocities in blocked annulus are smaller than local velocities in unblocked annulus. The blocking effect enhances the flow velocity in the wide gap resulting in increased flow rate. As a result, the presence of the cuttings bed surface below the drill pipe makes the hydraulic parameter fRe to decrease.

The trend reversal is not observed with diameter ratios of 0.75 and 0.5 because the 10% bed height is not below the bottom of the inner pipe (Fig. 4.1). Furthermore, as the shear thinning behavior of the fluid improves, the parameter consistently decreases.

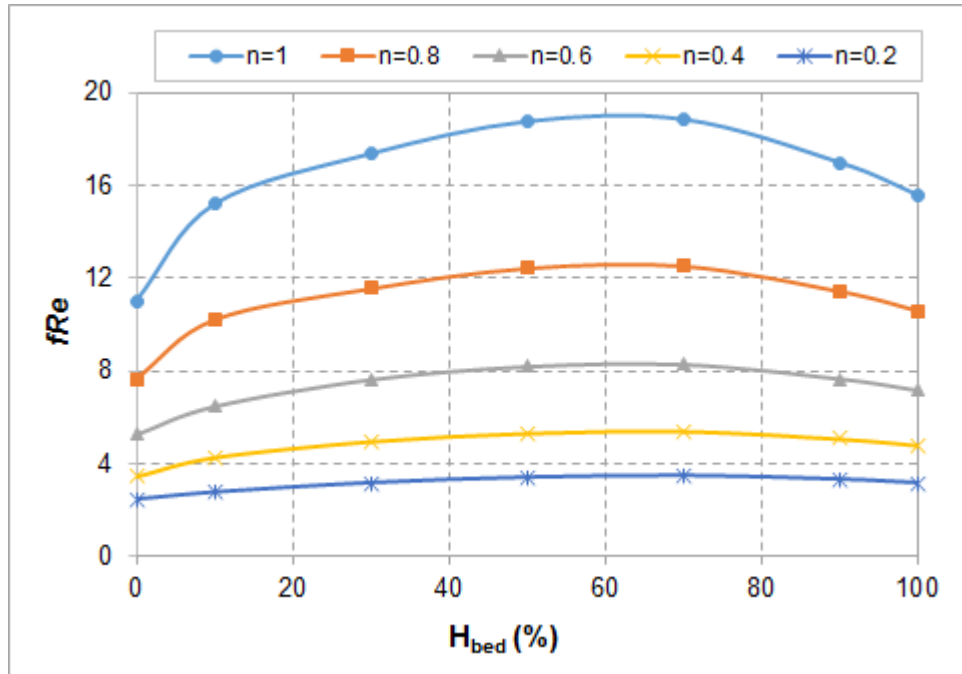


Figure 5.11 fRe vs. % bed height ($e=0.9$, $\kappa=0.75$ and $Q = 5 \times 10^{-5} \text{ m}^3/\text{s}$)

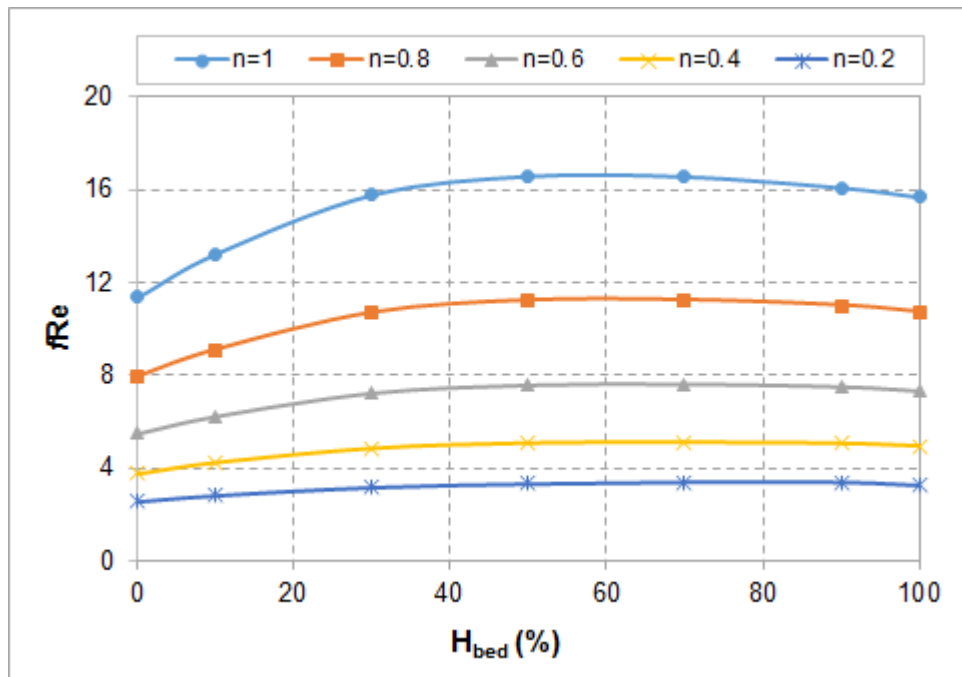


Figure 5.12 fRe vs. % bed height ($e=0.9$, $\kappa=0.5$ and $Q = 5 \times 10^{-5} \text{ m}^3/\text{s}$)

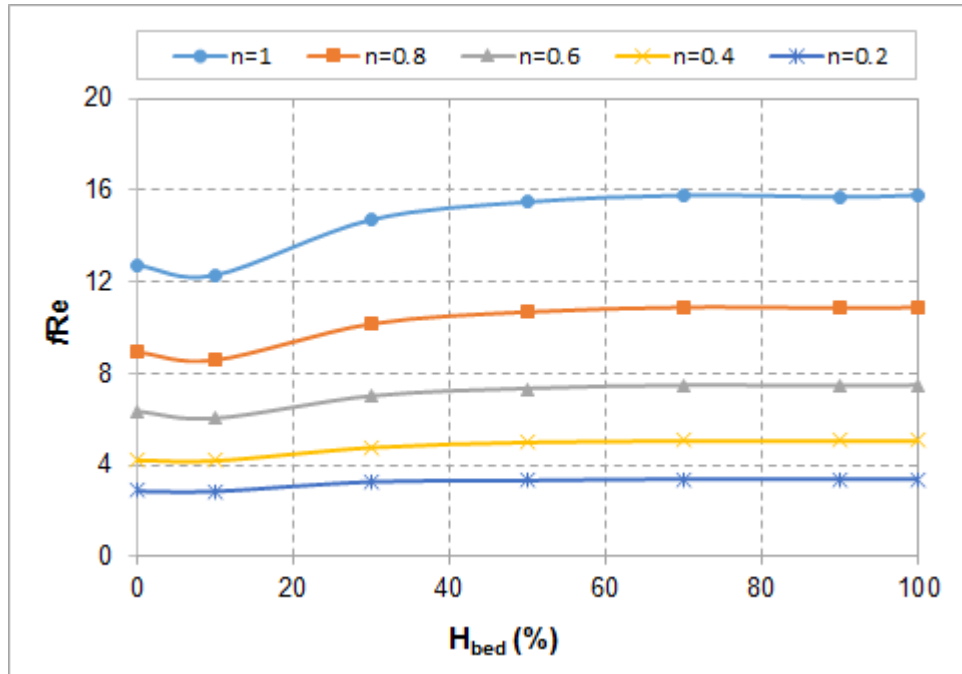
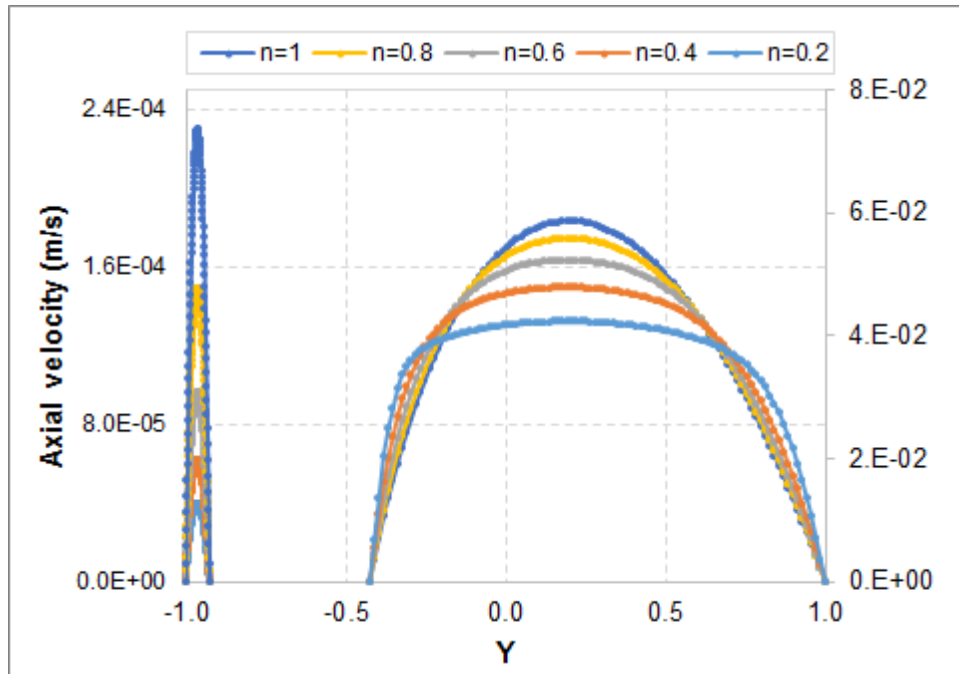
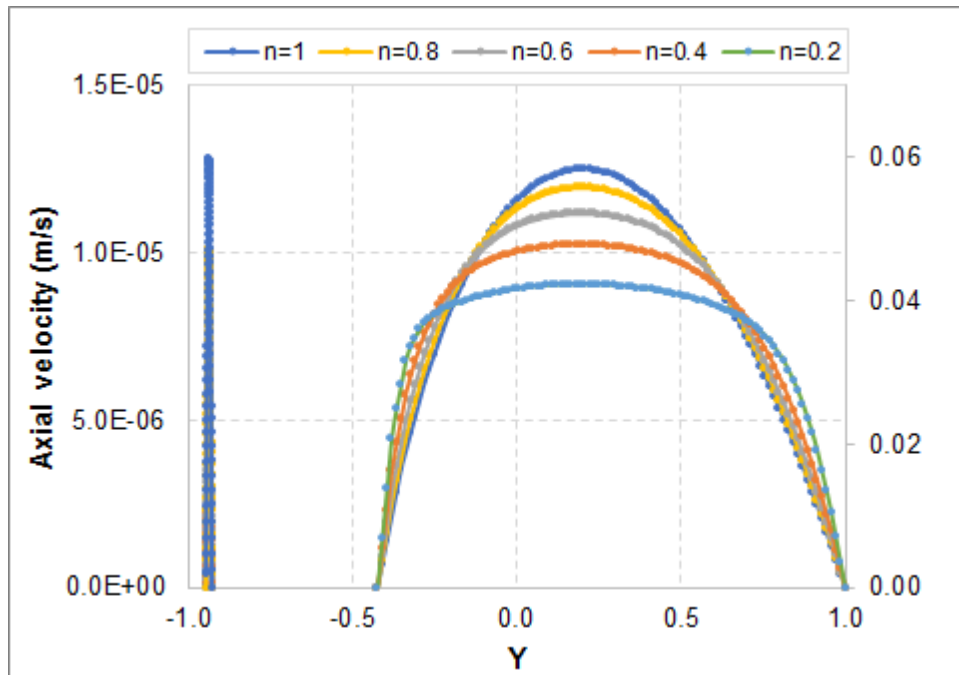


Figure 5.13 fRe vs. % bed height ($e=0.9$, $\kappa = 0.25$ and $Q = 5 \times 10^{-5} \text{ m}^3/\text{s}$)



(a)



(b)

Figure 5.14 Axial velocity profiles vs. Y ($\kappa = 0.25$, $e=0.9$ and $Q = 5 \times 10^{-5} \text{ m}^3/\text{s}$): (a) 0% H_{bed} ; and (b) 10% H_{bed}

Volume Flow Rate Variation Effect on fRe Parameter

The volume flowrate is increased to $1 \times 10^{-4} \text{ m}^3/\text{s}$, in order to evaluate its effect on the parameter fRe . Simulation results (Figs. 5.11 and 5.15) show that fRe is independent of the flow rate. It can be concluded that, at constant eccentricity, the hydraulic parameter fRe is a function of annular diameter ratio, power law index of the fluid and thickness of cuttings bed.

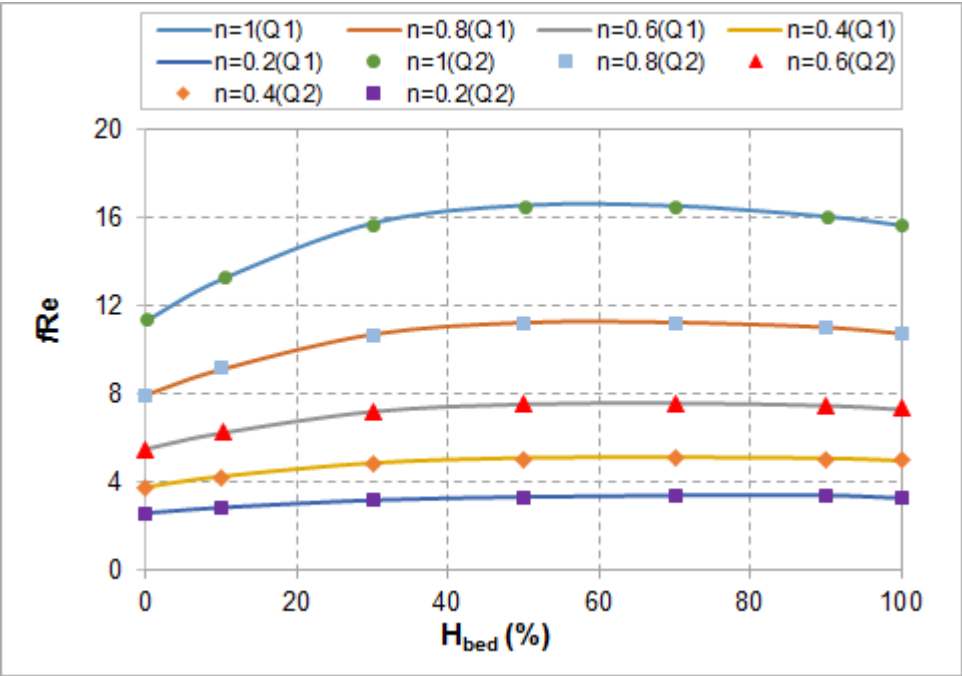


Figure 5.15 fRe vs. % H_{bed} : $Q1= 1 \times 10^{-5} \text{ m}^3/\text{s}$; $Q2= 1 \times 10^{-4} \text{ m}^3/\text{s}$ ($e=0.9$, and $\kappa=0.5$)

5.2.4 Wall Shear Stress

As mentioned before, in eccentric annuli, the shear stresses acting on the inner and outer walls vary significantly; thus, non-uniform shear stress distribution is expected. In addition, formation of cuttings bed has influenced the wall shear stress distribution. Therefore, for simplicity, average wall shear stress ($\bar{\tau}_w$) is often used in hydraulic analysis. Figures 5.16, 5.17 and 5.18 show $\bar{\tau}_w$ values obtained from CFD simulation. It

can be noted that the $\bar{\tau}_w$ increases with accumulation of cuttings in the wellbore. Evidently, low $\bar{\tau}_w$ values are associated with low axial velocities, thus low pressure loss.

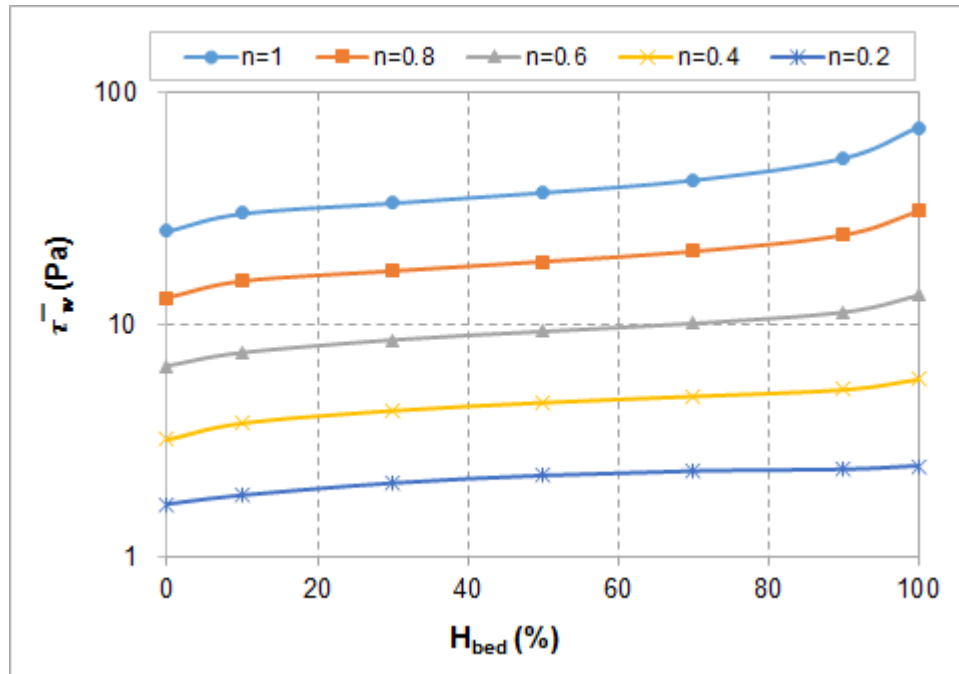


Figure 5.16 $\bar{\tau}_w$ vs. % H_{bed} ($e=0.9$, $\kappa=0.75$, $Q=1 \times 10^{-5} \text{ m}^3/\text{s}$)

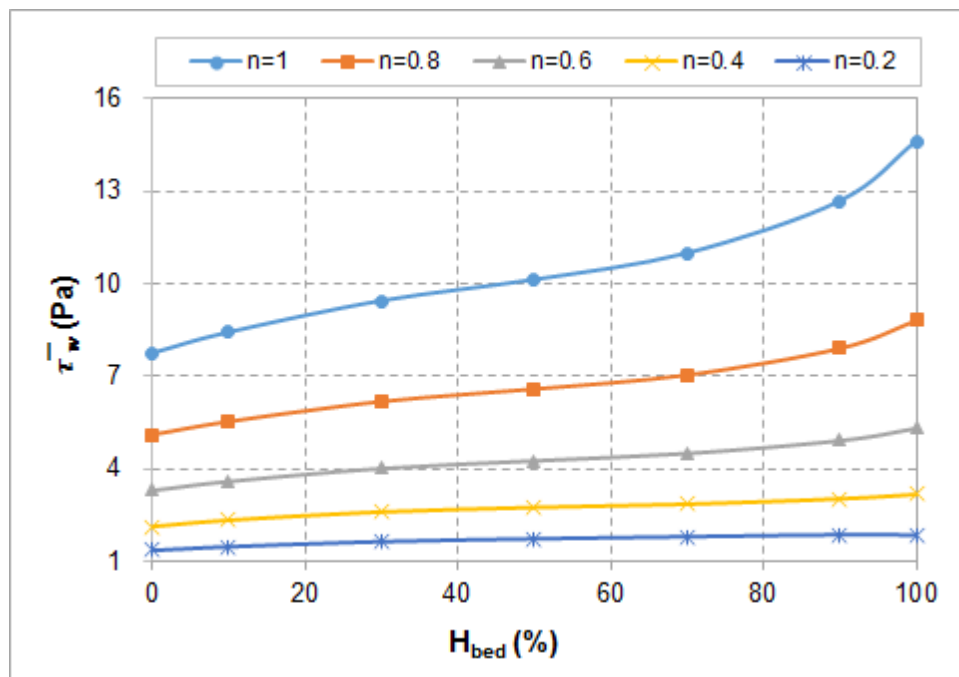


Figure 5.17 $\bar{\tau}_w$ vs. % H_{bed} ($e=0.9$, $\kappa=0.5$, $Q=1 \times 10^{-5} \text{ m}^3/\text{s}$)

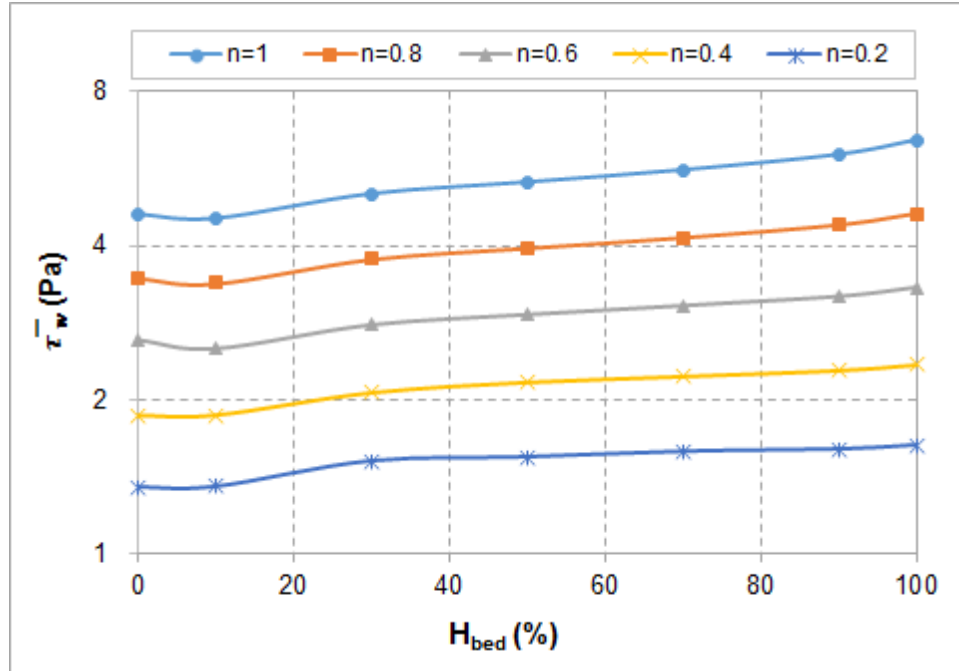


Figure 5.18 $\bar{\tau}_w$ vs. % H_{bed} ($e=0.9$, $\kappa=0.25$, $Q=1 \times 10^{-5} \text{ m}^3/\text{s}$)

The average wall shear stress is directly proportional to the pressure loss (Eqn. 3.21). Indeed, the average wall shear stress profiles (Figs. 5.16, 5.17 and 5.18) can be compared with the frictional pressure loss profiles obtained in Figs. 5.6, 5.7 and 5.8; as the cuttings bed height increases, the pressure drop increases; as a result, the mean wall shear stress increases as well. Moreover, as described in Section 5.2.3, the average wall shear stress slightly decreases due to the location of the bed (10% bed height) for a diameter ratio of $\kappa = 0.25$. Figure 5.18 shows similar trends of average wall shear stress profiles, which are observed in the pressure loss trend.

5.2.5 Bed Shear Stress

As stated before, low velocity profiles are associated with low wall shear stress profiles. This tendency can also be observed in the evaluation of the wall shear stress over

the surface of stationary cuttings bed presented in partially blocked annulus. It has been found that the bed shear stress increases as the cuttings bed height increases (Fig. 5.21).

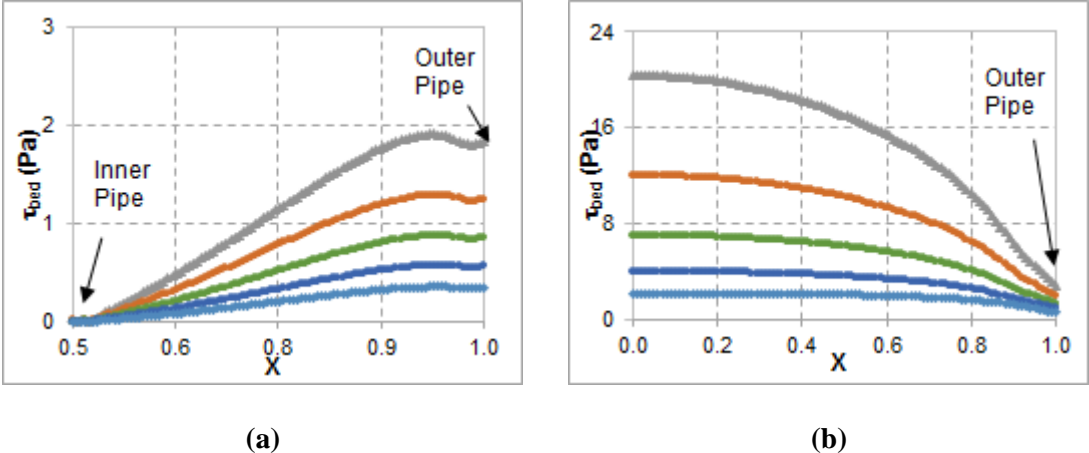


Figure 5.19 τ_{bed} vs. X ($e=0.9$, $\kappa=0.5$ and $Q= 5 \times 10^{-5} \text{ m}^3/\text{s}$): (a) $H_{bed} = 10\%$; and (b) $H_{bed}=100\%$

Furthermore, Fig. 5.19 presents the behavior of the bed shear stress along the dimensionless X - axis, as the cuttings bed builds up, for Newtonian and shear thinning fluids ($n = 1$ and $n = 0.2$). X corresponds to the dimensionless x -coordinate expressed in Eqn. 4.6. The positions $X = 0$ and $X = 1$ are located at the inner pipe and outer pipe walls, respectively. At low bed heights (10-30 %), the bed shear stress is higher close to the outer wall than close to the inner wall; however, as the cuttings bed thickness increases, higher bed shear stress is observed in the inner pipe side than the outer pipe side (Appendix E includes additional bed shear stress profiles for $\kappa = 0.25$ and $\kappa = 0.75$). Similar bed shear stress behavior is observed with highly shear thinning fluid, (i.e. $n = 0.2$).

Figure 5.19 demonstrates the effect of shear thinning on bed shear stress. As power law index increases, bed shear stress increases. Figure 5.20 illustrates bed shear

stress profile in annulus with 50% bed height and diameter ratio of 0.5. The maximum bed shear stress distribution corresponds to Newtonian fluid. Very low bed shear stress values are observed near the inner and outer walls due to flow stagnation.

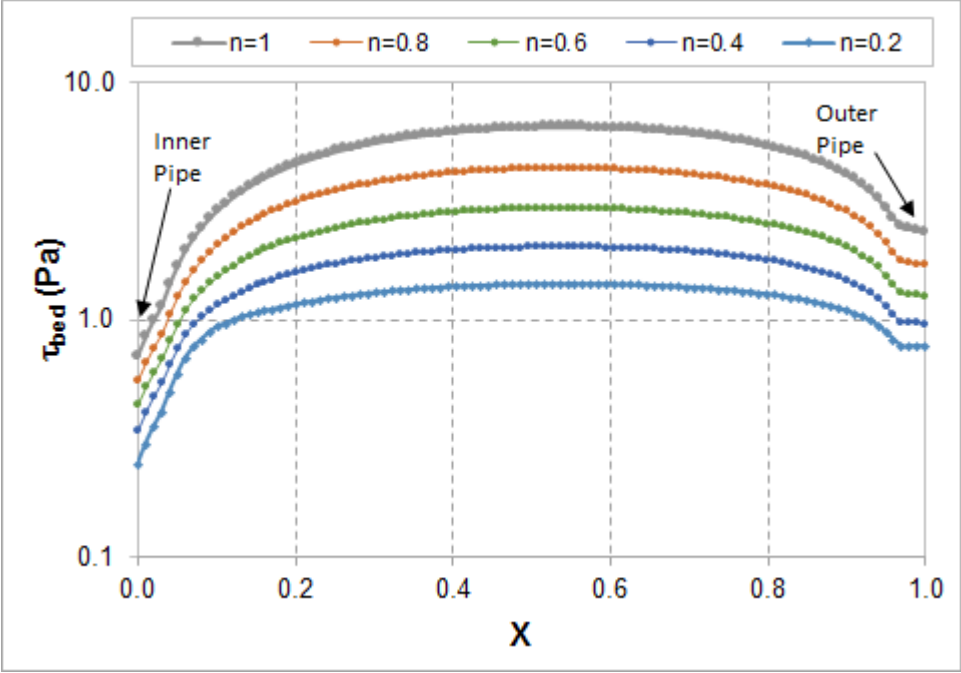


Figure 5.20 Shear stress distribution on cuttings bed surface, $H_{bed}= 50\%$ ($e =0.9$, $\kappa =0.5$, and $Q = 5 \times 10^{-5} \text{ m}^3/\text{s}$)

The average bed shear stress is often used in cuttings transport modeling, in determination of drag force on solid particles (Ahmed et al., 2002; Elgaddafi, 2011). Figures 5.21, 5.22 and 5.23 illustrate increase in average bed shear stress with cuttings bed height for a given flowrate. Effect of fluid behavior index on average bed shear stress is consistent with the trend observed with the overall wall shear stress. Average bed shear stress significantly increases with n .

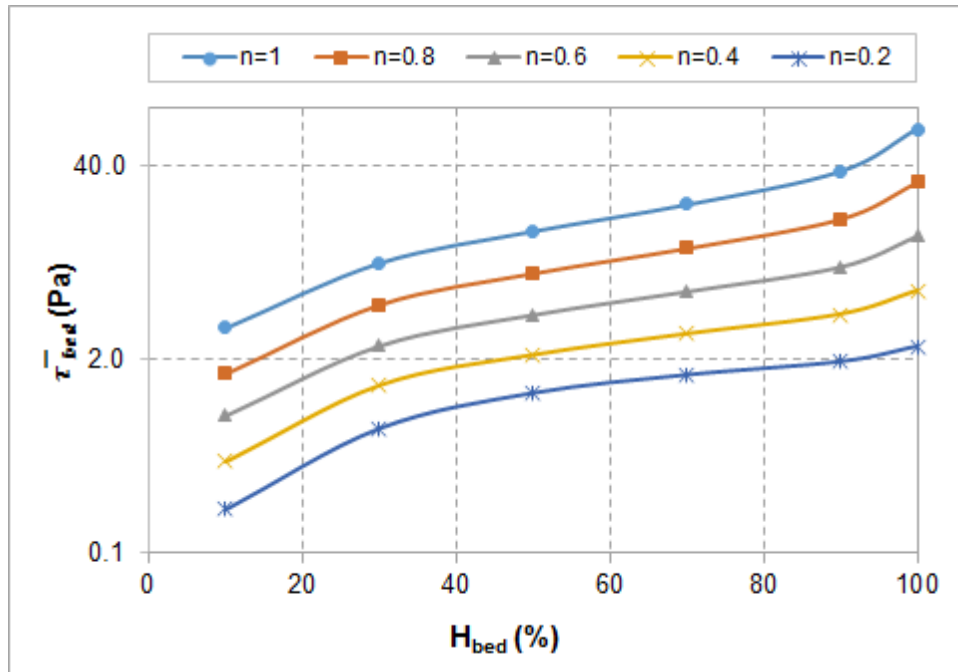


Figure 5.21 $\bar{\tau}_{bed}$ vs. % H_{bed} ($e=0.9$, $\kappa=0.75$ and $Q = 5 \times 10^{-5} \text{ m}^3/\text{s}$)

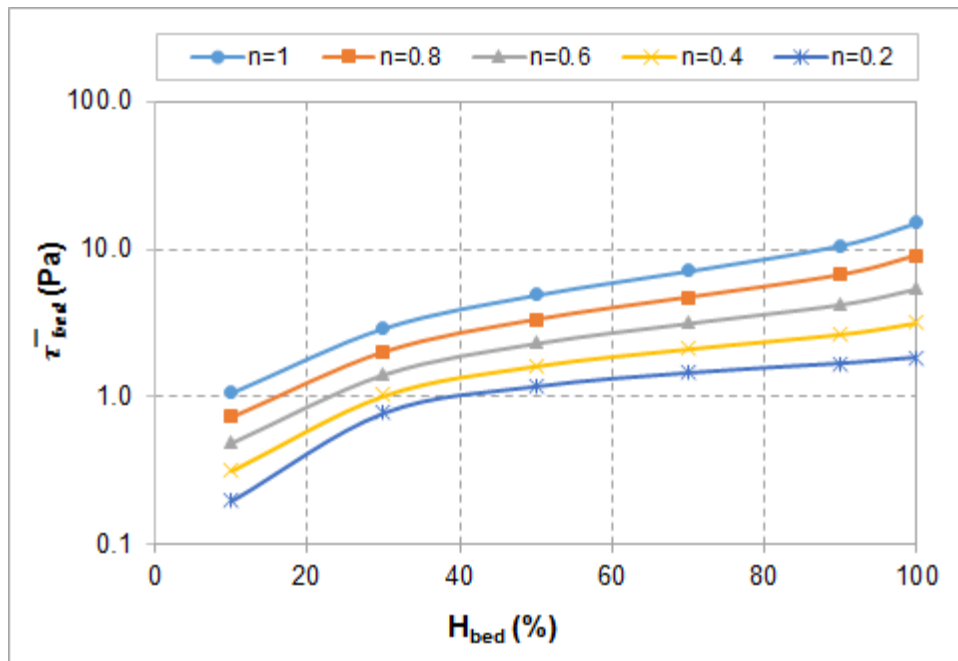


Figure 5.22 $\bar{\tau}_{bed}$ vs. % H_{bed} ($e=0.9$, $\kappa=0.50$ and $Q = 5 \times 10^{-5} \text{ m}^3/\text{s}$)

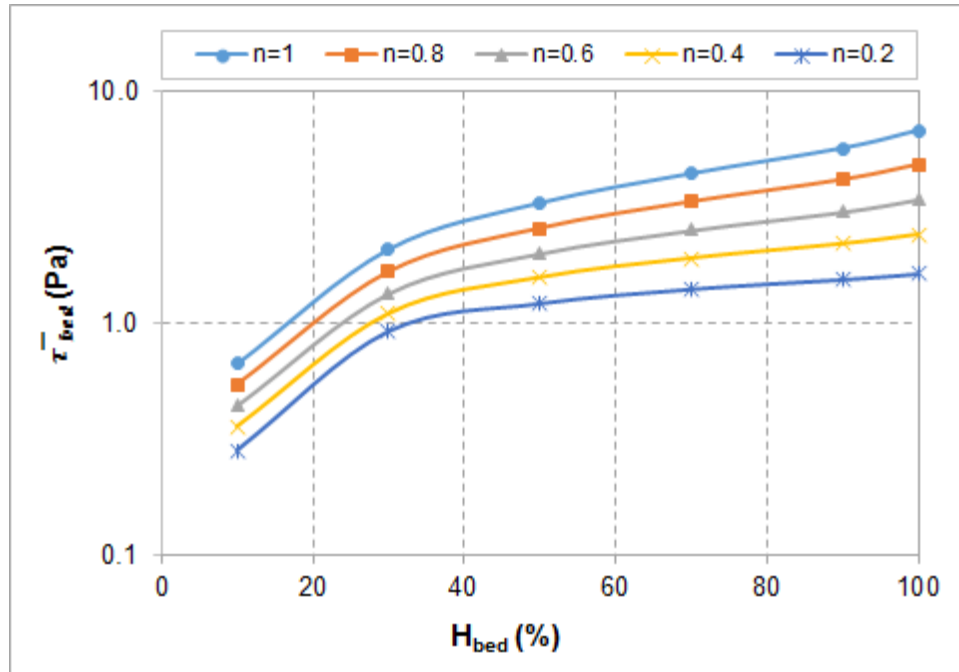


Figure 5.23 $\bar{\tau}_{bed}$ vs. % H_{bed} ($e=0.9$, $\kappa=0.25$ and $Q = 5 \times 10^{-5} \text{ m}^3/\text{s}$)

Effects of bed height on average bed shear stress is noticeable in Figs. 5.21 to 5.23. As the diameter ratio increases, bed shear stress increases at a constant flowrate. Moreover, axial fluid velocity influences the average bed shear stress.

Furthermore, one can observe that, as the dimensionless bed thickness varies from zero to 100%, magnitude of the average wall shear stress increases and approaches that of the overall wall shear stress. To compare these two shear stresses, dimensionless bed shear stress (the ratio of average bed shear stress to the overall wall shear stress is introduced). Figures 5.24, 5.25 and 5.26 show dimensionless bed shear stress as a function of bed height at different diameter ratios. Results demonstrate that the dimensionless bed shear stress increases with flow behavior index of the fluid (i.e. shear thinning behavior of the fluid). As the bed height approaches zero or 100%, the effect of n on dimensionless bed shear stress diminishes

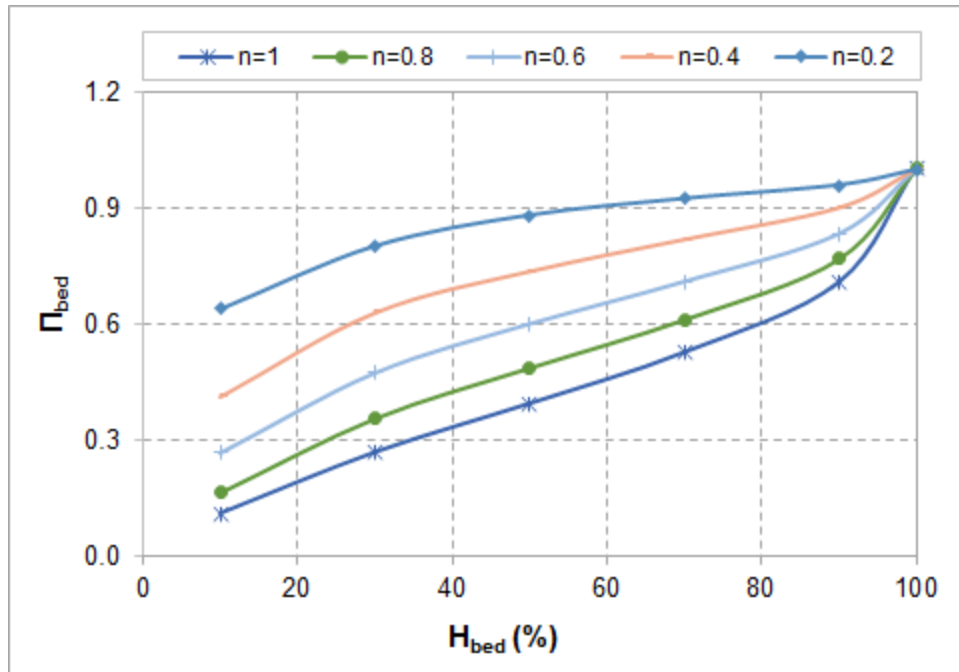


Figure 5.24 Π_{bed} vs. % H_{bed} ($e=0.9$, $\kappa=0.75$ and $Q = 5 \times 10^{-5} \text{ m}^3/\text{s}$)

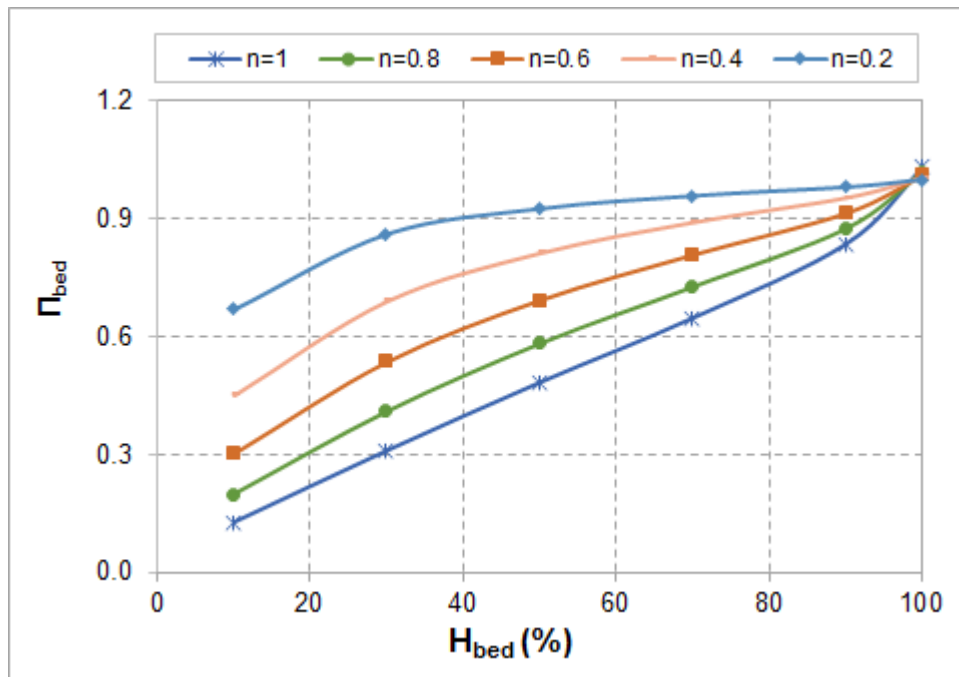


Figure 5.25 Π_{bed} vs. % H_{bed} ($e=0.9$, $\kappa=0.5$ and $Q = 5 \times 10^{-5} \text{ m}^3/\text{s}$)

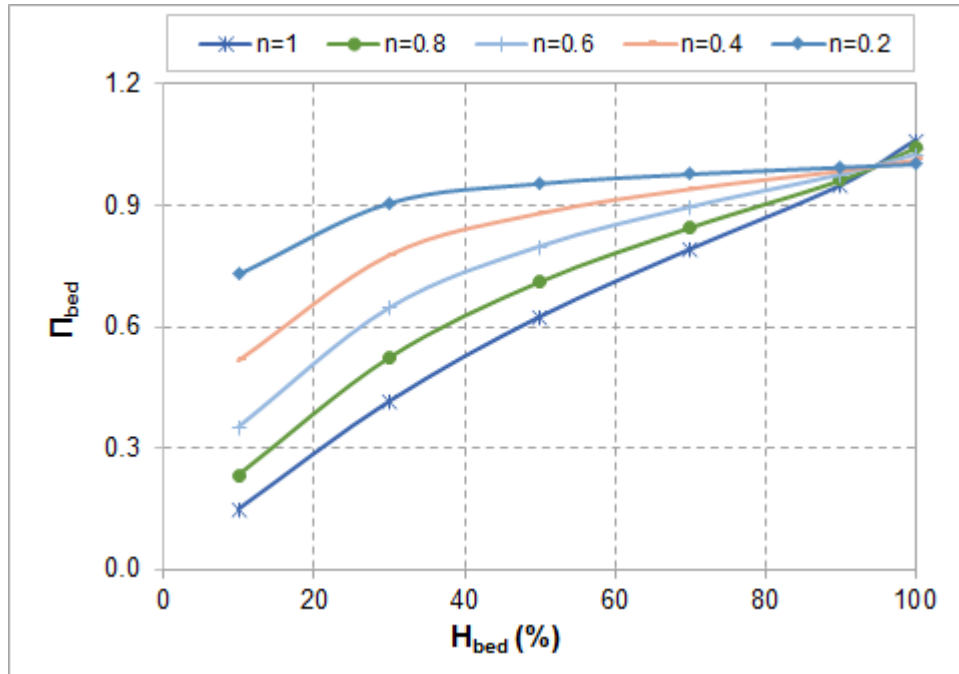


Figure 5.26 Π_{bed} vs. % H_{bed} ($e=0.9$, $\kappa=0.25$ and $Q = 5 \times 10^{-5} \text{ m}^3/\text{s}$)

Volume Flow Rate Variation Effect on Π_{bed} Parameter

As elaborated in Section 5.2.1, for the parameter fRe , the effect of the volume flowrate was also considered on the dimensionless bed shear stress profile (Fig. 5.27). The new profile of dimensionless bed shear stress is observed in Fig. 5.29, when the volume flow rate increases to $1 \times 10^{-4} \text{ m}^3/\text{s}$ for a diameter ratio of 0.5. Therefore, the dimensionless bed shear stress is a function of the geometry (diameter ratio, bed height) and the rheology of the fluid (i.e. power law index).

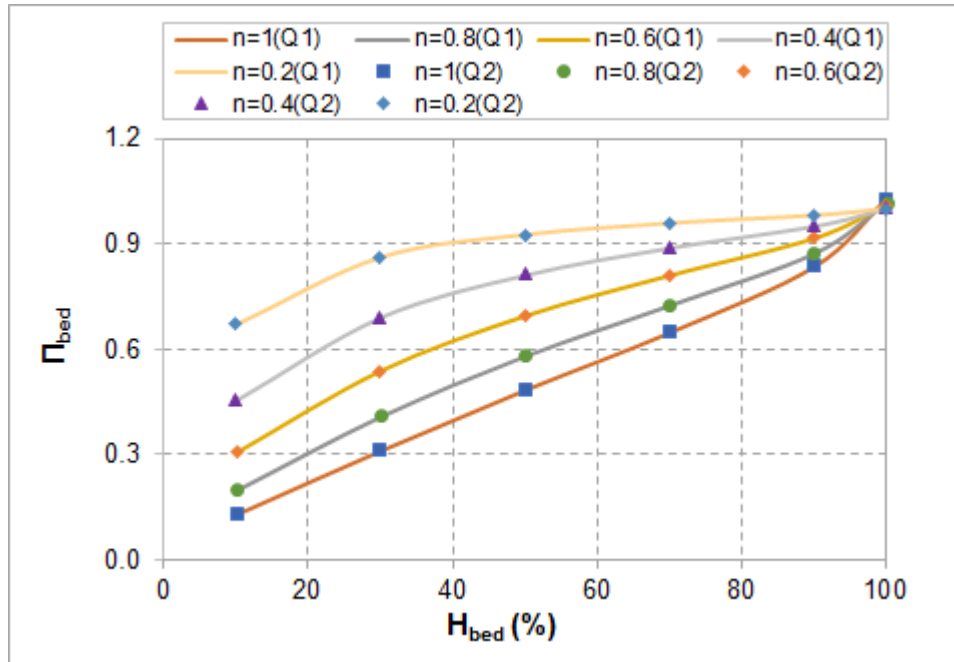


Figure 5.27 Π_{bed} vs. % H_{bed} : a) $Q1= 1 \times 10^{-5} \text{ m}^3/\text{s}$; b) $Q2= 1 \times 10^{-4} \text{ m}^3/\text{s}$ ($e=0.9$, $\kappa=0.5$)

5.3 Development of New Correlations

The simulation data obtained in the previous section are used to develop correlations of dimensionless parameters, as a function of diameter ratio (0.75, 0.5 and 0.25), eccentricity of 0.9, flow behavior index (from 0.2 to 1) and cuttings bed height (from 0 to 100%). First, correlation coefficients involved in the calculation of hydraulic parameter fRe data are used to determine the geometric constants a and b described in Section 3.5.2. Secondly, dimensionless bed shear stress data is used to develop an empirical correlation, for dimensionless bed shear stress in terms of independent variables (diameter ratio, fluid behavior index and dimensionless cuttings bed height).

5.3.1 Hydraulic Parameter fRe

As shown in Section 5.2.3, the hydraulic parameter fRe is a function of geometric constants (a and b). For partially blocked annulus, the geometric constants are evaluated adapting the procedure presented by Aworunse (2012). During the evaluation, eccentricity is kept fixed (90%) and effect of cuttings bed height on a shape factor (S) is investigated. Plots of the shape factor are generated for each geometry (i.e. each diameter ratio) and presented as a function of dimensionless parameter, $1/n$. The tendency of each cuttings bed height to form straight lines in S versus $1/n$ plot can be observed in Fig. 5.28. Thus, the slope and intercept for each straight line are determined and resulted in unique geometric constants for each wellbore geometry, regardless of fluid consistency index and flow parameters. Figure 5.28 shows straight lines used to obtain the geometric parameters, “ a ” from the slope, and “ b ” from the intercept for different cuttings bed heights.

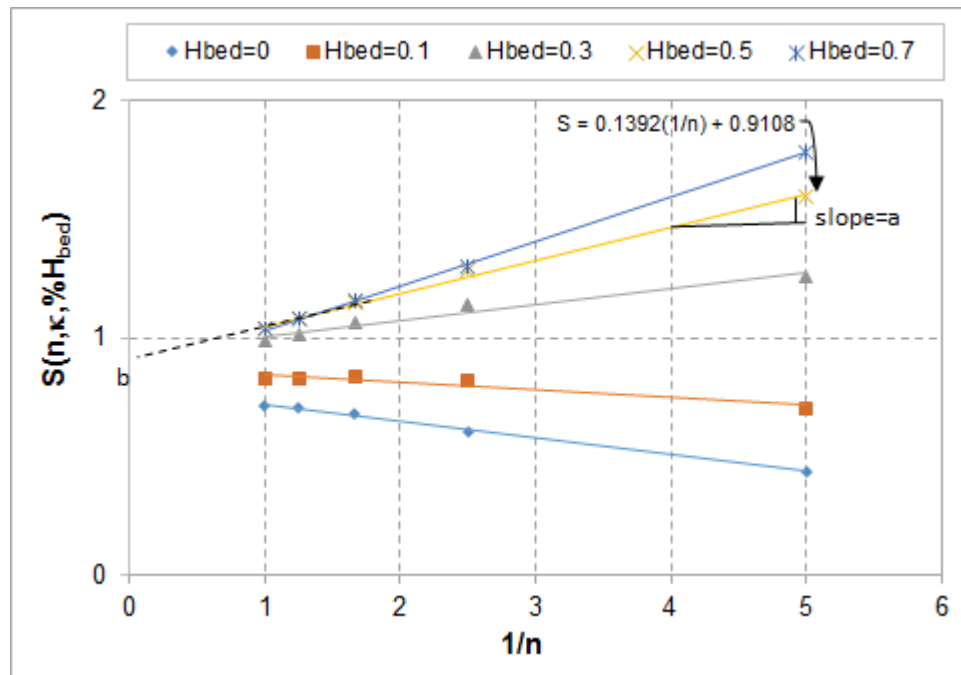


Figure 5.28 Shape Factor vs. $1/n$ ($e=0.9$). Trendline for different bed heights ($\kappa=0.5$)

Figure 5.28 corresponds to a diameter ratio of 0.5, where the R-squared is above 93%. The same procedure is repeated to obtain geometric constants for other diameter ratios (0.25 and 0.75), and they are presented in Appendix E. Figure 5.29 displays parameter constant “ a ” as a function of the dimensionless bed height for different diameter ratios. As shown, the value of constant “ a ” increases with bed height at low bed heights (less than 70%); however, the trend changes at approximately 70% of H_{bed} and the constant decreases with bed thickness. Despite strong dependency of geometric constant “ a ” with bed height, the geometry constant “ b ” is slightly affected with bed height (Fig. 5.32).

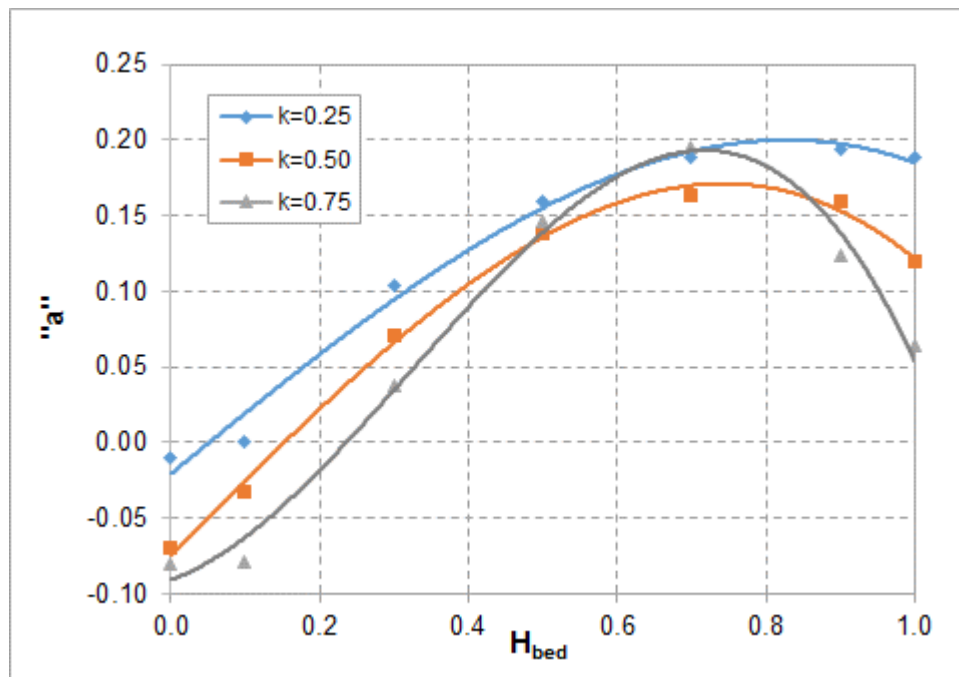


Figure 5.29 Parameter “ a ” vs. dimensionless bed height ($e=0.9$) for different κ values

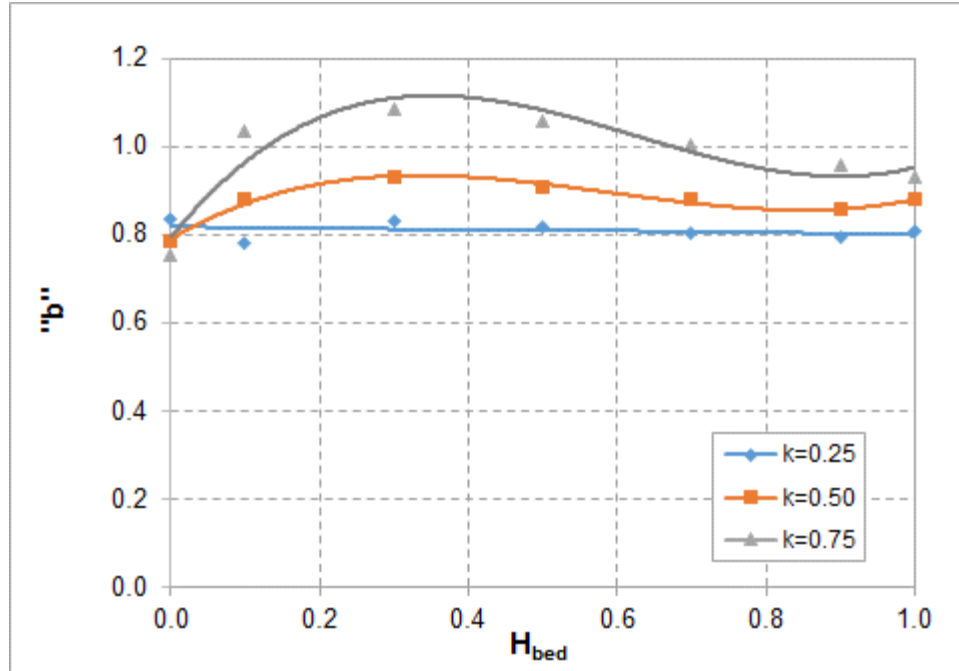


Figure 5.30 Parameter “b” vs. dimensionless bed height ($e=0.9$) for different κ values

After obtaining the geometric constants “a” and “b” from the shape factor (Fig. 5.28), correlations for the constants are developed using regression analysis. The constants are correlated with bed height as:

$$a = \lambda_0 \cdot H_{bed}^3 + \lambda_1 \cdot H_{bed}^2 + \lambda_2 \cdot H_{bed} + \lambda_3 \quad (5-1a)$$

$$b = b_0 \cdot H_{bed}^3 + b_1 \cdot H_{bed}^2 + b_2 \cdot H_{bed} + b_3 \quad (5-1b)$$

The coefficients ($\lambda_0, \lambda_1, \lambda_2, \lambda_3, b_0, b_1, b_2$ and b_3) are functions of diameter ratio. As it can be seen, the geometric constants “a” and “b” best fit a 3rd degree polynomial, with R-squared values of more than 0.96. The Table 5.1 summarizes equations used to determine these coefficients.

Table 5.1 Regression coefficient parameters developed (e=0.9)

$\lambda_0 = -6.2328\kappa^2 + 4.1994\kappa - 0.8453$	$b_0 = -0.964\kappa^2 + 5.425\kappa - 1.3217$
$\lambda_1 = 9.152\kappa^2 - 6.7796\kappa + 1.1096$	$b_1 = -0.1792\kappa^2 - 8.1756\kappa + 2.0884$
$\lambda_2 = -3.236\kappa^2 + 2.7778\kappa - 0.0881$	$b_2 = 0.836.\kappa^2 + 3.4122\kappa - 0.9325$
$\lambda_3 = 0.284\kappa^2 - 0.4266\kappa + 0.06684$	$b_3 = 0.2456\kappa^2 - 0.2934\kappa + 0.8761$

If the inner and outer annular diameters, and the cuttings bed height are known, one can determine the parameters “*a*” and “*b*” using Eqns. 5.1a and 5.1b, respectively. The predictions of the correlation are shown in Fig. 5.31 predicted values are within $\pm 5\%$ of discrepancy.

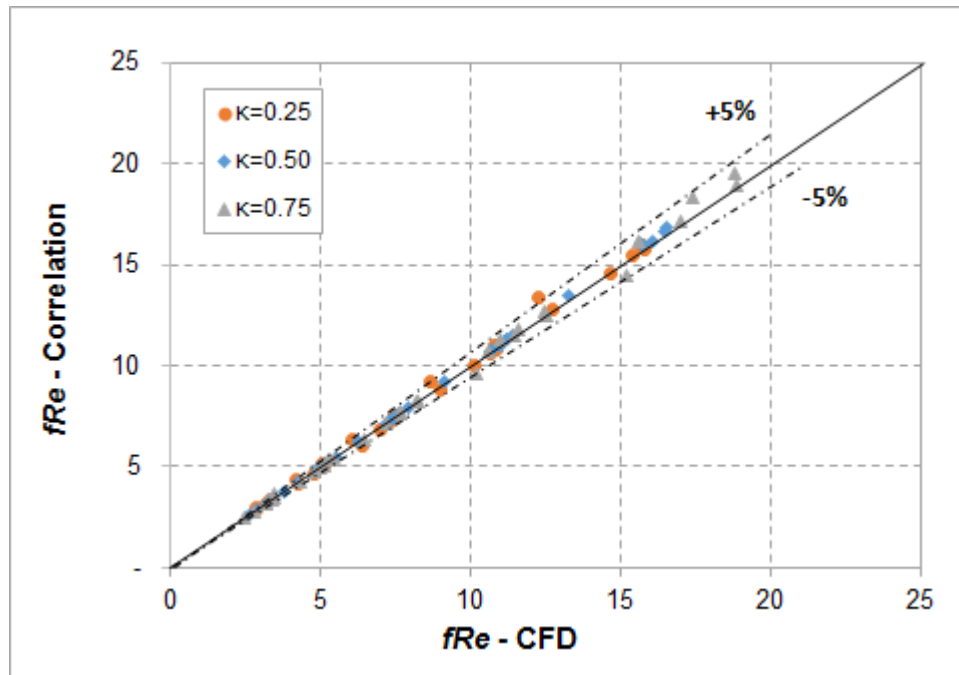


Figure 5.31 *fRe* Correlation vs. *fRe* CFD (e=0.9)

Furthermore, to validate the correlations, available experimental data is used. Table 5.2 compares measured pressure losses with simulation results and model predictions.

Table 5.2 Numerical validation based on pressure drop values ($e=0.9$)

Fluid	H_{bed} (%)	Flowrate (m³/s)	Re_{gen}	dP/dL (Pa/m) Exp	dP/dL (Pa/m) Fluent	dP/dL (Pa/m) Model
SBM	87	0.0032	433.0	840	696	770
SBM	74	0.0038	498.2	826	768	774
SBM	53	0.0044	548.0	730	855	786

For SBM fluid, it can be noted that model predictions are in good agreement with experimental results, where the predictions are within $\pm 8.37\%$ discrepancy range. This shows a better prediction when compared with simulation results, where the discrepancy can reach a value of $\pm 17\%$.

Comparison between New and Existing Models

Figures 5.32, 5.33 and 5.34 display the comparison between existing models with CFD simulation results. The model proposed by Chen (2005) for predicting pressure loss in a partially blocked concentric annulus with power-law fluid (Appendix D) is used to compare with the new CFD model in Fig. 5.32. It is evident the high discrepancy between the model and CFD data, which can reach up to $\pm 80\%$. The reason for this significant difference is that the existing model does not account for pipe eccentricity, which reduces considerably the pressure drop. In this study, a modified model (Exlog Mod. 1) has been developed by introducing a correction factor based the model developed by

Haciislamoglu and Langlinais (1990) to relate pressure loss in an eccentric annulus to that of a concentric one (Appendix D). Figure 5.33 compares predictions of Exlog Mod 1 with CFD simulation results. Mostly discrepancies are with $\pm 25\%$; however, as the diameter ratio increases ($\kappa = 0.75$), they reach up to 40%.

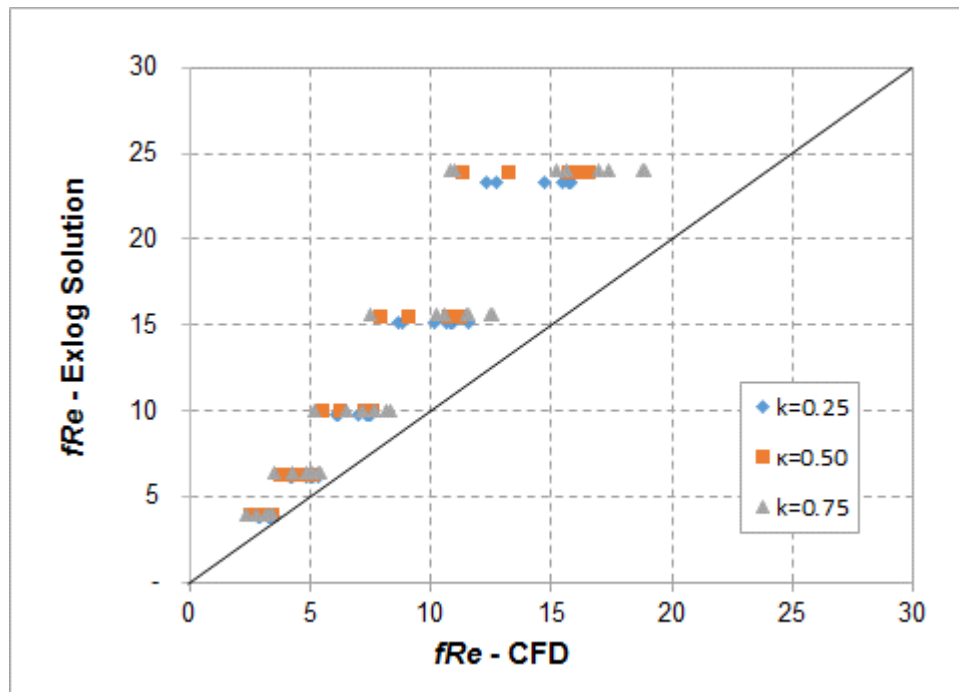


Figure 5.32 fRe Exlog Solution (Chen, 2005) vs. fRe CFD

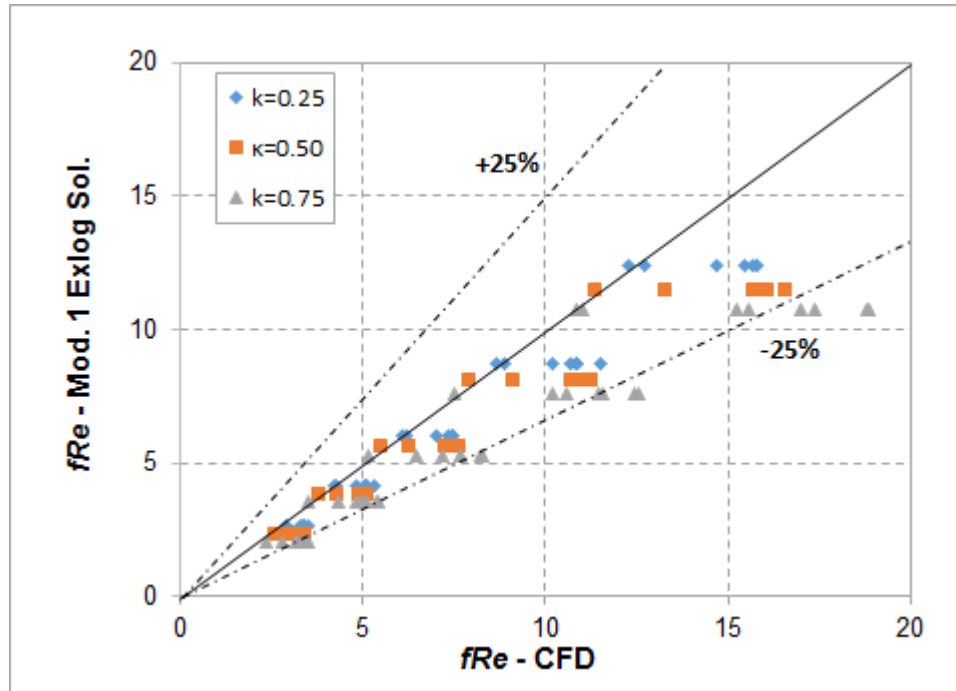


Figure 5.33 fRe Exlog solution modified 1 (Chen 2005; correction factor by Hacıislamoglu and Langlinais, 1990) vs. fRe CFD

The correction factor proposed by Hacıislamoglu and Langlinais (1990) is not valid for highly shear thinning fluids ($n \leq 0.4$). Since the new model is developed for power law index varying from 0.2 to 1.0 and, the correlations (Section 2.2.3, Eqns. 2.19 a and b) developed by Ahmed et al. (2006) is used to account for eccentricity in improved Exlog model (Exlog Mod 2) formulation. Figure 5.34 compares predictions of Exlog Mod 2 with CFD simulation results. Like Exlog Mod 1, predictions of Exlog Mod 2 predominately display discrepancies of $\pm 25\%$. Nevertheless, for annulus with narrow clearance (high diameter ratio), discrepancy can reach up to 40%.

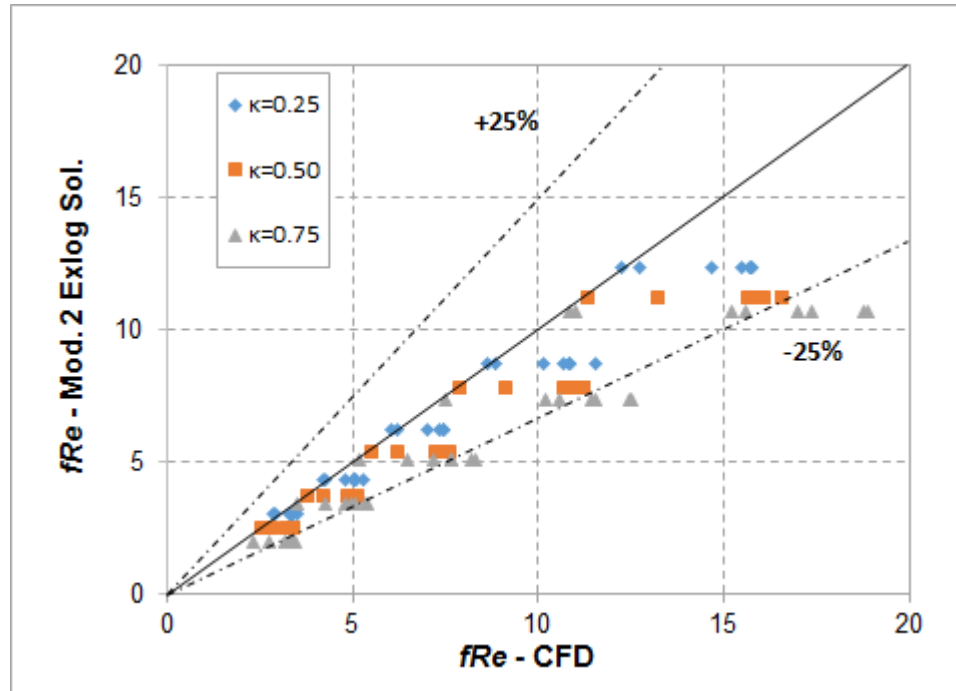


Figure 5.34 fRe Exlog Solution modified 2 (Chen, 2005; correction factor by Ahmed et al., 2006) vs. fRe CFD

Furthermore, the model developed by Aworunse (2012) for partially blocked eccentric annulus is compared with CFD simulation results. Figure 3.37 compares predictions of Aworunse's model (Appendix B) with CFD results. Model predictions are within $\pm 17\%$ error bands (the lowest discrepancy obtained with existing models). However, it should be pointed out that the model presented by Aworunse (2012) is developed for a fixed eccentricity of 80%.

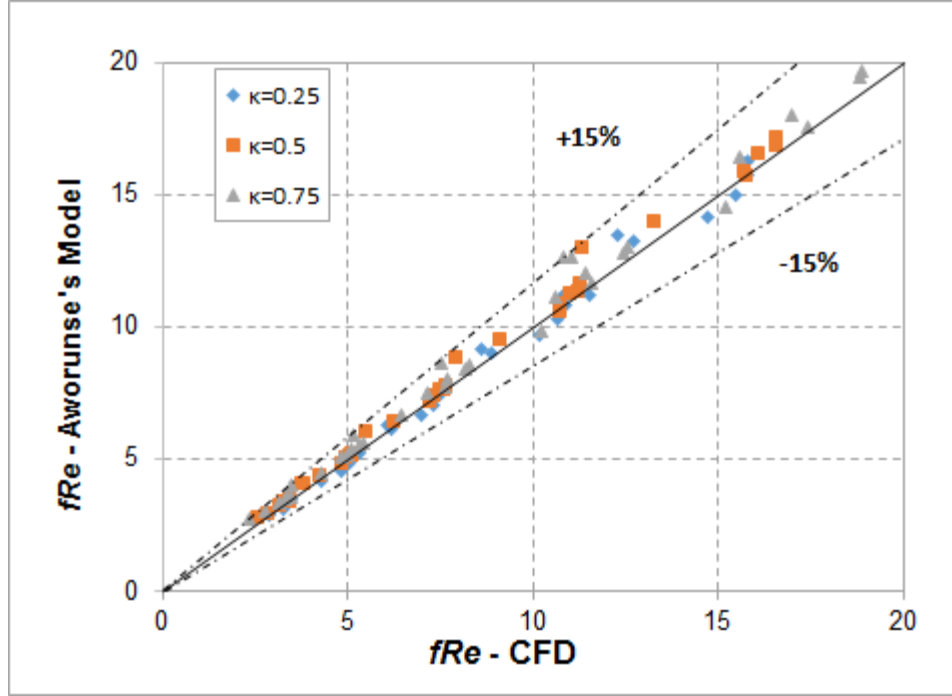


Figure 5.35 fRe Aworunse's model (Aworunse, 2012) vs. fRe CFD

5.3.2 Bed Shear Stress

In addition to the parameter fRe , an empirical correlation is developed to determine dimensionless bed shear stress. The correlation is expressed as:

$$\begin{aligned} \Pi_{bed} = & 0.4668H_{bed}^{4.511} - 0.747H_{bed}^{2.51} + 0.8957H_{bed}^{0.51} - 0.5166n\kappa^{0.51} + \\ & 0.6366(nH_{bed})^{1.431} - 0.4077n + 0.525 \end{aligned} \quad (5-2)$$

Equation 5.2 is valid for laminar flow power law fluid in partially blocked 90% eccentric annulus with different diameter ratios ($0.25 \leq \kappa \leq 0.75$), power law index ($0.2 \leq n \leq 1$) and dimensionless bed heights ($0.15 < H_{bed} \leq 1$).

A cross plot of model predicted dimensionless bed shear stress and CFD data is presented in Fig. 5.36. Model predictions are predominately within discrepancy level of

$\pm 10\%$. In general, the new model predictions show good agreement with the simulated data.

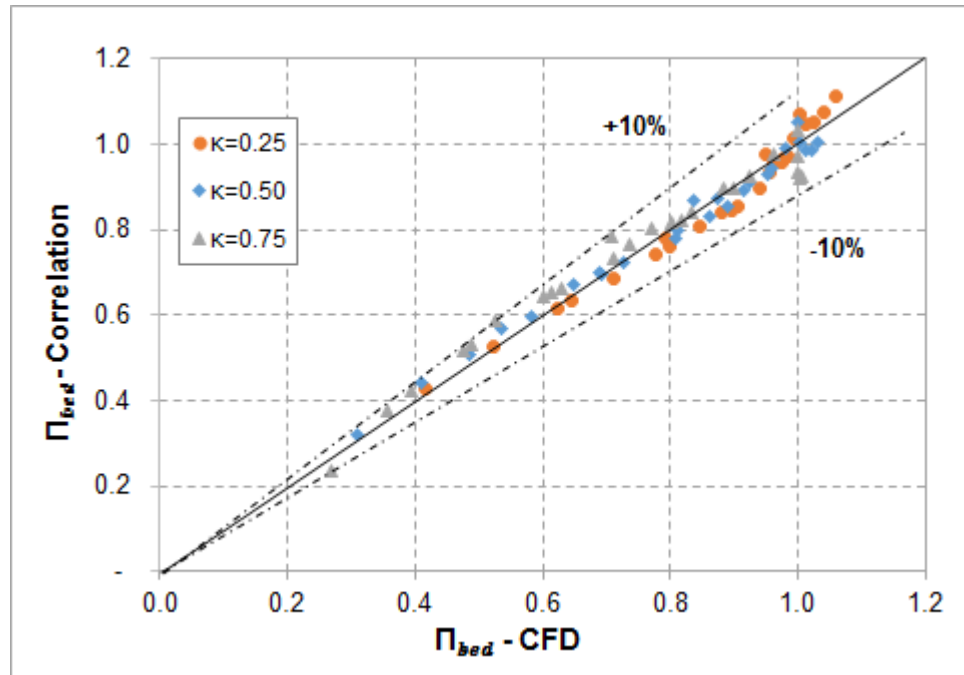


Figure 5.36 Π_{bed} computed from correlation and CFD data

Chapter 6. Conclusions and Recommendations

6.1 Conclusions

CFD simulation has been conducted to evaluate effect of partially obstruction on pressure loss of 90% eccentric annuli. Dimensionless bed height, diameter ratio and power law index are varied. Results show significant increase in pressure loss with cuttings bed growth. Based on the numerical results and theoretical analysis, the following conclusions can be made:

- The suitability of the CFD code has been verified using analytical solution, published numerical solutions and available experimental results.
- Annular pressure loss and bed shear stress significantly change with cuttings bed growth and reduce as the fluid becomes strongly shear thinning (when n value decreases). As a result, lower average wall shear stress is expected for highly shear thinning fluids as compared to fluids that do not exhibit strong shear thinning.
- For power law fluids, the hydraulic parameters fRe and dimensionless bed shear stress are dependent on the annular geometry (cuttings bed height and diameter ratio for a fixed eccentricity) and fluid behavior index. They are independent of fluid consistency index and volumetric flowrate.
- Dimensionless bed shear stress is significantly affected by cuttings bed height and power law index. It increases with shear thinning behavior of fluid (i.e. when n decreases).
- Empirical model developed for geometric parameters and dimensionless bed shear stress make reasonable predictions that show good agreement with CFD

simulation results and experimental measurements. The new model provides better predictions than existing models.

6.2 Recommendations

CFD is a powerful tool to conduct flow studies involving non-Newtonian fluids in complex geometry; hence, it is recommended to extend this study considering the following additional parameters:

- Considering the effect of yield stress on pressure loss of yield power law fluid.
- Further work is encouraged to analyze turbulent fluid flow in partially blocked eccentric annulus. CFD programs provide turbulent flow models ($k-\omega$ and $k-\epsilon$) to analyze fluid flow under turbulent flow conduction.
- Since the present study is conducted without inner tubing rotation, it is more interesting to study effects of inner pipe rotation on the pressure loss.

References

- Ahmed R., Skalle, P, Johansen, S.T., Svein, J., Saasen, A. 2001. Mechanistic model for cuttings removal from solid bed in inclined channels. *J. Pet. Sci. Eng.* 30 (3-4), 129-141.
- Ahmed, R.M., Skalle, P., and Johansen, S.T. 2002. A mechanistic Model to Determine the Critical Flow Velocity Required to Initiate the Movement of Spherical Bed Particles in Inclined Channels. *Chemical Engineering Science*, vol. 58, 2153-2163.
- Ahmed, R., Miska, S. and Miska W. 2006. Friction Pressure Loss Determination of Yield Power Law Fluid in Eccentric Annular Laminar Flow. *Wiertnictwo Nafta Gaz*, Tom 23/1.
- Ahmed, R., and Miska S. 2009. Advanced Wellbore Hydraulics-. Advanced Drilling and Well Technology. Aadnoy, B; Cooper, I; Miska, S.; Mitchell, R.F.; Payne, M.L., (Ed), Society of Petroleum Engineers. Texas, 191-217.
- Aworunse, O.A. 2012. Modeling of Power-Law Fluid Flow in Annulus with Cutting Bed Buildup. MS Thesis, the University of Oklahoma, Norman, OK.
- Azouz, I., Shirazi, S.A., Pilehvary, A., and Azar, J.J. 1993. Numerical Simulation of Laminar Flow of Yield-Power-Law Fluids in Conduits of Arbitrary Cross-Section. *Journal of Fluids Engineering-ASME*, December, Vol. 115, 710-716.

- Azouz, I. 1994. Numerical Solution of Laminar and Turbulent Flows of Wellbore fluids in annular passages of Arbitrary Cross-section. PhD Dissertation, The University of Tulsa, OK.
- Bicalho, I.C., dos Santos, D.B.L, Ataíde, C.H., and Duarte, C.R. 2016. Fluid-Dynamic Behavior of Flow in Partially Obstructed Concentric and Eccentric Annuli with Orbital Motion. *Journal of Petroleum Science and Engineering*. Brazil. 137, 202-213.
- Bird, R., Stewart, W., and Lightfoot, E. 1960. Transport Phenomena. John Wiley & Sons, Inc., 34-82.
- Bourgoyne, A.T., Millheim, K.K., Chenevert, M.E., and Young F.S. 1986. Applied Drilling Engineering. SPE Textbook Series, vol. 2, 104.
- Capobianchi, M. And Irvine, T.F. 1992. Predictions of Pressure Drop and Heat Transfer in Concentric Annular Ducts with modified Power Law Fluids. Springer-Verlag. New York, 27, 209-215
- Chen, Z. 2005. Cuttings Transport with Foam in Horizontal Concentric Annulus under Elevated Pressure and Temperature Conditions. PhD Dissertation, The University of Tulsa, OK, 190-191.
- Chin, W.C. 1992. Borehole Flow Modeling in Horizontal, Deviated, and Vertical Wells, Gulf Publishing Co. Houston, TX.

- Ebrahim, N., E-Khatib, N., and Awang, M. 2013. Numerical Solution of Power Law Fluid through Eccentric Annular Geometry. *American journal of Numerical Analysis*. Malaysia, vol.1, 1-7.
- Elgaddafi, R.M. 2011. Hole Cleaning Performance of Water-Based Fiber-Containing Sweep Fluids. M.S. Thesis, The University of Oklahoma. Norman, OK.
- Escudier, M.P., Oliveira P.J, Pinho, F.T., and Smith, S. 2002. Fully Developed Laminar Flow of Purely Viscous Non-Newtonian Liquids through Annuli, Including the Effects of Eccentricity and Inner Cylinder Rotation. *Int. Journals of Heat and Fluid Flow*, 2352-73.
- Fang, P., Manglik, R.M., and Jog, M.A. 1999. Characteristics of Laminar Viscous Shear-Thinning Fluid Flows in Eccentric Annular Channels. *J. Non-Newtonian Fluid Mech.* 84, 1-17.
- Fang, P. and Manglik, R.M. 2002. The influence of Inner cylinder rotation on laminar axial flows in eccentric annuli of drilling bore wells. *Int J. of Trans. Phenomena*, Vol. 4, pp 257-274.
- FLUENT INC, 2015. FLUENT 16.1 User's Guide, Southpointe 2600 ANSYS Drive, Canonsburg, PA, SAS IP, Inc.
- Fredrickson, A.G. and Bird, R.B. 1958. Non-Newtonian Flow in annuli. *Industrial and Engineering Chemistry*. Vol. 50, No. 1, 347-352.

- George, M. 2012. Flow Behavior and Hole Cleaning Efficiency of Synthetic-based Fiber-Containing Drilling Fluids. M.S. Thesis, The University of Oklahoma. Norman, OK.
- George, M., Elgaddafi, R., Ahmed, R., Growcock, F. 2014. Performance of Fiber-Containing Synthetic-Based Sweep Fluids. *Journal of Petroleum Science and Engineering*, vol. 119, 185-195
- Guckes, T. L. 1975. Laminar Flow of Non-Newtonian Fluids in an Eccentric Annulus, paper 74-Pet 57 presented at ASME Petroleum Mechanical Engineering Conference, Dallas, TX, September, 498-506.
- Haciislamoglu, M. 1989. Non-Newtonian Fluid Flow in Eccentric Annuli and its Application to Petroleum Engineering Problems, PhD Dissertation, Louisiana State University.
- Haciislamoglu, M and Langlinais, J. 1990. Non-Newtonian Flow in Eccentric Annuli. *Journal of Energy Resources Technology*, vol. 112,163-169.
- Hansen S.A., Rommetveit, R., Sterri N., AND Aas B. 1999. A New Hydraulic Model for Slim Hole Drilling Applications (SPE 57579). Paper SPE presented at SPE/IADC Middle East Drilling Technology Conference, Abu Dhabi, UAE, 8-10 November.
- Heyda, J. F. 1959. A green's Function Solution for the Case of Laminar Incompressible Flow between Non-Concentric Circular Cylinders. *Franklin Inst.*, vol. 267, 25-34.

- Hussain, Q. E. and Sharif, M.A. 1998. Analysis of Yield-Power-Law Fluid Flow in Irregular Eccentric Annuli. *Journal of Energy Resources Technology*, vol. 120, 201-207.
- Iyoho Q. W. and Azar, J. J. (1981). An Accurate Slot-Flow Model for Non-Newtonian Fluid Flow through Eccentric Annuli. Paper SPE 9447. *Society of Petroleum Engineers Journal*, 565- 572.
- Kozicki, W., Chou, C.H., and Tiu, C. 1966. Non-Newtonian Flow in Ducts of Arbitrary Cross-Sectional Shape. *Chem. Engi. Sci.*, 21, 665-679.
- Lamb, H. 1945. *Hydrodynamics*, 6th Edition, Dover Publications, Inc. New York City, NY
- Luo, Y. and Peden, J.M. 1987. Flow of Drilling Fluids through Eccentric Annuli. Paper SPE presented at Annual Conference and Exhibition, Dallas, TX, September 27-30, 389-396.
- IBM. 2012. Information Tehcnology Guide for ANSYS FLUENT Customers. IBM Global Services. Route 100, Somers, NY.
- Manglik, R. and Fang, P. 1995. Effect of Eccentricity and Thermal Boundary Conditions on Laminar Fully Developed Flow in Annular Ducts. *International J. Heat and Fluid Flow*, vol. 16, No. 4, 298-306.

- Mitchel, R.F. Landmark Graphics and Ravi, K. 2006. Fluid Mechanics for Drilling. Drilling Engineering, Vol. II. Mitchel R.F., and Lake, L.W. (Ed.). Society of Petroleum Engineers. Texas. 118-183.
- Mitsuishi, N. and Aoyagi, Y. 1973. Non-Newtonian Fluid Flow in an Eccentric Annulus, *Journal of Chemical Eng.*, Japan, 6, No. 5, 402-08.
- Nguyen Q.-H. and Nguyen N.-D. 2012. Incompressible Non-Newtonian Fluid Flows, Continuum Mechanics-Progress in Fundamentals and Engineering Applications, Dr. Y. Gan (Ed). InTech, 47-71.
- Nouri, J.M., Umur, H., and Whitelaw, J.H. 1993. Flow of Newtonian and non-Newtonian fluids in a concentric annulus with rotation of the inner cylinder. *J. Fluids Eng.* 116, 821-827.
- Nouri, J.M., and Whitelaw J.H.,1994. Flow of Newtonian and non-Newtonian fluids in a concentric annulus with rotation of the inner cylinder. *J. Fluids Eng.*, 116, 821-827.
- Nouri, J.M. and Whitelaw, J.H. 1997. Flow of Newtonian and non-Newtonian fluids in an eccentric annulus with rotation of the inner cylinder. *Int. J. Heat Fluid Flow.* 18, 236-246.
- Ogugbue, C.C. and Shah, S.N. 2011. Computational Fluid Dynamics Modeling of Non-Newtonian Power Law Fluids in Eccentric Annular Geometries. *International Journal of Petroleum Science and Technology.*

- Ozbayoglu, E.M. 2002. Cuttings Transport with Foam in Horizontal and Highly Inclined Wellbores. PhD Dissertation. The University of Tulsa.
- Ozbayoglu M.E, and Omurlu C. 2006. A New Mechanistic Model for Two-Phase Flow Through Eccentric Horizontal Annulus (SPE100300). Middle East Technical U. EAGE 68th Conference & Exhibition- Vienna Austria 12-15 June.
- Pereira, F.A.R., Barrozo, M.A.S., and Ataide, C.H. 2007. CFD Predictions of Drilling Fluid Velocity and Pressure Profiles in Laminar Helical flow. *Brazilian Journal of Chemical Engineering*, 24(4), 587-595.
- Piercy N.A.V, Hooper, M.S., and Winny, H.F. 1933. Viscous Flow through pipes with core. London Edinburgh Dublin Phil. Mag. *J. Sci.*, 15, 647-676
- Reed, T. and Pilehvari, A. 1993. A new Model for Laminar, Transitional, and Turbulent Flow of Drilling Muds. Paper SPE 25456, presented at the Production Operations Symposium, OKC, OK, 21-23 March.
- Redberger, P. J. and Charles, M.E. 1962. Axial laminar Flow in a Circular Pipe Containing a Fixed Eccentric Core. *Canadian Journal of Chemical Engineering*, 148-154.
- Schlichting, H. and Gersten, K. 2000. Boundary-Layer Theory, Springer-Verlag, Berlin Heidelberg.
- Silva, M.A. and Shah S. 2000. Friction Pressure Correlations of Newtonian and Non-Newtonian Fluids through Concentric and Eccentric annuli, Paper SPE 60720,

presented at 2000SPE/ICoTA Coiled Tubing Roundtable, Houston, TX, 5-6 April.

Sijun, Y. 1994. Non-Newtonian Flow in Annuli, PhD Dissertation, Mechanical Engineering, Mc. Master University, Hamilton, Ontario.

Spiegel, M.R. 1968. Mathematical Handbook of Formulas and Tables. McGraw Hill Book Co., 125-128.

Snyder, W.T. and Goldstein, G.A. 1965. An analysis of Fully Developed Laminar Flow in an Eccentric Annulus. *A. Ins. Chem. Eng. Journal.*, Vol. 11, 462-467.

Tao, L. N. and Donovan, W.F. 1955. Through Flow in Concentric and Eccentric Annuli of Fine Clearance with and without Relative Motion of the Boundaries. *Trans-ASME*, 77, 1291-1301.

Tang, M., Ahmed, R., and He, S. 2016. Modeling of Yield-Power-Law fluid flow in a partially blocked concentric annulus. *Journal of Natural Gas Sc. and Eng.* 35 pg. 555-566.

Uner, D., Ozgen, C., and Tosum, I. 1989. Flow of a Power-Law Fluid in an Eccentric Annulus. *SPE Drilling Engineering Paper 17002*, 269-272.

Vaughn, R. D. 1965. Axial Laminar Flow of Non-Newtonian fluids in Narrow Eccentric annuli. *SPE Paper 1138-PA. Society of Petroleum Engineers Journal*, 277-280.

- Volarovich and Gutkin 1946. Visco-plastic Flow between Two Plane parallel walls and in an annular Clearance between Coaxial pipes, Zh. Tekhn.Fiziki, vol. XVI, No. 3, 321-329.
- Wang, H., Su, Y., Bai, Y. and Gao, Z. 2000. Experimental Study of Slimhole Annular Pressure Loss and its Field Applications. SPE59265. IADC/SPE Drilling conference held in New Orleans, Louisiana, 23-25 February.
- Whitaker, A. 1985. Theory and Applications of Drilling Fluid Hydraulics. Springer Netherlands.
- Willenbacher, N., and Georgieva, K. 2013. Rheology of Disperse Systems. Product Design and Engineering: Formulation of Gels and Pastes. Brockel, U., Meier, W., and Wagner, G., (Ed), Wiley-VCH Verlag GmbH & Co. Germany, 7-49.
- Zamora, M., Roy, S., and Slater, K. 2005. Comparing a Basic Set of Drilling Fluid Pressure-loss Relationship to Flow Loop and Field Data. Paper AADE-05-NTCE-27 presented as the AADE National Conference and Exhibition, Houston, Texas. April 5-7.

Appendix A: Nomenclature

Symbols

A	pipe area, m ²
A_{ann}	annular area, m ²
a^*	variable
a	geometric parameter
a_0	constant
a_1	constant
a_2	constant
a_3	constant
B_0	constant
B_1	constant
B_2	constant
b	geometric parameter
b_0	constant
b_1	constant
b_2	constant
b_3	constant
C_0	constant
C_1	constant
C_2	constant
C_3	constant

D	diameter, m
D_{eff}	effective Diameter, m
D_h	parameter, m
D_{hyd}	hydraulic diameter, m
D_i	inner diameter, m
D_o	outer diameter, m
e	relative eccentricity
F	parameter (Eq. 2.6)
f	fanning friction factor
fRe	friction factor- Reynolds number
g_x	gravity in x-direction
g_y	gravity in y-direction
g_z	gravity in z-direction
G	Geometric factor
H	bed height, m
H_{bed}	dimensionless bed height
H_{max}	max. height
h	height, m
h^*	clearance between inner and outer pipes (bottom part), m
K	consistency index, pa s^n
L	third axis, m
ΔL	length, m

M	parameter
m	series variable
n	power-law index
N	flow behavior index
P	pressure, Pa
$\frac{dp}{dz}$	pressure gradient, pa/m
Q	flowrate, m ³ /s
R	radius, m
r	radial position, m
R_i	drill pipe outer radius, m
R_o	wellbore radius, m
Re	Reynolds number
Re_{gen}	generalized Reynolds number, PL fluid
S	Shape factor
S_i	bed perimeter, m
S_1	inner pipe perimeter, m
S_2	outer pipe perimeter, m
u	local axial velocity, m/s
U	mean flow velocity, m/s
v	local velocity (1 direction)
v_x	local fluid velocity on the z-axis, m/s
v_y	local fluid velocity on the y-axis, m/s

v_z	local fluid velocity on the x-axis, m/s
X	dimensionless x- axis
Y	dimensionless y- axis
Y^*	parameter
x	x-axis
y	y-axis
z	z-axis
Z	dummy variable
o	outer
i	inner
w	wall
W	width

Greek Symbols

α	parameter
α_0	constant
α_1	constant
α_2	constant
α_3	constant
β	parameter
ε	constant

ε_i	constant
ε_0	constant
ΔV	volume passing through a control volume, m ³
ΔP	pressure drop, Pa
Δt	variation in time, s
$\dot{\gamma}$	shear rate, 1/s
$\dot{\gamma}_c$	critical shear rate, 1/s
$\dot{\gamma}_w$	wall shear rate, 1/s
μ	viscosity of Newtonian fluid, Pa.s
$\mu(\dot{\gamma})$	apparent viscosity, Pa.s
η	constant
θ	θ axis
λ_0	constant
λ_1	constant
λ_2	constant
λ_3	constant
κ	diameter ratio $\kappa = \frac{R_i}{R_o}$
ρ	density, kg/m ³
τ	shear stress, Pa
τ_{wall}	wall shear stress, Pa
$\bar{\tau}_w$	average wall shear stress, Pa
$\bar{\tau}_{bed}$	average bed shear stress, Pa

τ_{bed}	bed shear stress, Pa
Π_{bed}	dimensionless bed shear stress
ψ	constant

Acronyms

ECD	Equivalent Circulating Density
PL	Power Law
SBM	Synthetic Base Mud
YPL	Yield-Power Law

Note: S.I. units were utilized throughout this study.

Appendix B: Additional Derivations

Fully Developed Laminar Flow in a Straight Tube

The simplified momentum balance equation in z direction (cylindrical coordinates) for a circular pipe expresses the relationship between radius r , shear stress τ_{rz} , and friction pressure gradient $\frac{\partial p}{\partial z}$ in the form:

$$\frac{\partial p}{\partial z} + \frac{1}{r} \frac{\partial}{\partial r} (r\tau_{rz}) = 0 \quad (\text{B-1})$$

The axial velocity in a pipe (Fig. 3.3) $v_z(r)$ of cross sectional area is determined by integrating Eqn. B.1 for a Newtonian fluid, with non-slip boundary conditions (i.e. velocity at the walls $v_z(R) = 0$, Bourgoyne et al., 1986). This yields:

$$v_z(r) = \frac{(\Delta P)R^2}{4\mu L} \left[1 - \left(\frac{r}{R} \right)^2 \right] \quad (\text{B-2})$$

where R is the radius of the pipe, μ de dynamic viscosity, and $\frac{(\Delta P)}{L}$ the pressure gradient, r is the local radius.

The volumetric flowrate through a pipe of area perpendicular to the flow of width dr is expressed in the integral form as:

$$Q = 2\pi \int_0^R r v_z(r) dr \quad (\text{B-3})$$

After substituting Eqn. B.2 into Eqn. B.3, the integration yields the volumetric flow rate of a pipe for an incompressible Newtonian fluid, known as the Hagen-Poiseuille Equation, with the form:

$$Q = \frac{(\Delta P)R^4}{8\mu L} \quad (3-10)$$

where Q is the volumetric flow rate.

A flow behavior index N , is used to simplify the Rabinowitsch-Mooney equation 3.12. N is substituted by the inverse of the gradient term: $(\frac{d \ln \tau_w}{d \ln(8U/D)})$. Thus, the simplification yields:

$$\dot{\gamma}_w = \left(\frac{8U}{D}\right) \left[\frac{3N+1}{4N}\right] \quad (\text{B-4})$$

The equation above is adopted by various researchers to develop further correlations of fluid flow for power-law fluids. Based on Metzner and Reed's work (1955), Reed and Pilehvari (1993) adapted the shear stress definition in Eqn. 3.1 for power-law fluids at the walls, with $N = n = \text{constant}$

Wall Shear Stress in Terms of Flowrate

Assuming Newtonian fluid, the Hagen-Poiseuille Eqn. 3.10 is combined with B.6 developed from the momentum Equation (B.1) to express the wall shear stress in terms of the volumetric flowrate in fully developed laminar pipe flow as in B.7.

$$\tau = \frac{(p_1 - p_2)r}{2L} \quad (\text{B-5})$$

For $r = R$, then

$$\tau_w = \frac{(p_1 - p_2)R}{2L} \quad (\text{B-6})$$

As a result:

$$\tau_w = \frac{4\mu Q}{\pi R^3} \quad (\text{B-7})$$

The simplified form of flowrate formula is expressed as:

$$Q = \pi R^2 U \quad (\text{B-8})$$

Combining Eqns. B.7 and B.8, the wall shear stress for Newtonian fluids is expressed as:

$$\tau_w = \mu \frac{8U}{D} \quad (\text{B-9})$$

Regression Model (Aworunse, 2012)

The geometric parameters are a function of the cuttings bed height, for a constant dimensionless eccentricity, in the forms:

$$a = C_0 H_{bed}^3 + C_1 H_{bed}^2 + C_2 H_{bed} + C_3 \quad (\text{B-10a})$$

$$b = B_0 H_{bed}^2 + B_1 H_{bed} + B_2 \quad (\text{B-10b})$$

where the coefficients parameters of the correlations can be observed in Table B.1, for an eccentricity of 0.8 as a function of the diameter ratio.

Table B.1 Regression coefficient parameters (Aworunse, 2012)

$C_0 = -1.6575\kappa^2 + 1.3195\kappa - 0.505$	$B_0 = -0.795\kappa^2 - 0.1645\kappa + 0.069$
$C_1 = 2.675\kappa^2 - 3.534\kappa + 1.0934$	$B_1 = 0.91\kappa^2 + 0.266\kappa - 0.1831$
$C_2 = -0.6187\kappa^2 + 1.6882\kappa - 0.2102$	$B_2 = -0.0537\kappa^2 + 0.0437\kappa + 0.841$
$C_3 = -0.0637\kappa - 0.0069$	

Appendix C: Additional Simulation Matrices

Table C.1 Matrix simulation. Diameter ratio 0.75

$D_i/D_o = 0.50$					
n H/H_{max}	0.2	0.4	0.6	0.8	1
0	Sim 36	Sim 37	Sim 38	Sim 39	Sim 40
0.1	Sim 41	Sim 42	Sim 43	Sim 44	Sim 45
0.3	Sim 46	Sim 47	Sim 48	Sim 49	Sim 50
0.5	Sim 51	Sim 52	Sim 53	Sim 54	Sim 55
0.7	Sim 56	Sim 57	Sim 58	Sim 59	Sim 60
0.9	Sim 61	Sim 62	Sim 63	Sim 64	Sim 65
1.0	Sim 66	Sim 67	Sim 68	Sim 69	Sim 70

Table C.2 Matrix simulation. Diameter ratio 0.25

$D_i/D_o = 0.25$					
n H/H_{max}	0.2	0.4	0.6	0.8	1
0	Sim 71	Sim 72	Sim 73	Sim 74	Sim 75
0.1	Sim 76	Sim 77	Sim 78	Sim 79	Sim 80
0.3	Sim 81	Sim 82	Sim 83	Sim 84	Sim 85
0.5	Sim 86	Sim 87	Sim 88	Sim 89	Sim 90
0.7	Sim 91	Sim 92	Sim 93	Sim 94	Sim 95
0.9	Sim 96	Sim 97	Sim 98	Sim 99	Sim 100
1.0	Sim 101	Sim 102	Sim 103	Sim 104	Sim 105

Appendix D: Hydraulic Diameter Calculation and Existing Correlation Model for PL Fluid in Concentric Annulus with Cuttings

Bed

Hydraulic diameter of partially blocked eccentric annulus is calculated as:

$$D_{hyd} = \frac{4 \cdot A_{ann}}{S_1 + S_2 + S_i} \quad (D-1)$$

The annular area (A_{ann}) and wetted perimeters ($S_1 + S_2 + S_i$) in Eqn. D.1 is displayed in Fig. D.1. Further details regarding the algorithm for calculating the hydraulic diameter is presented elsewhere (Chen, 2005).

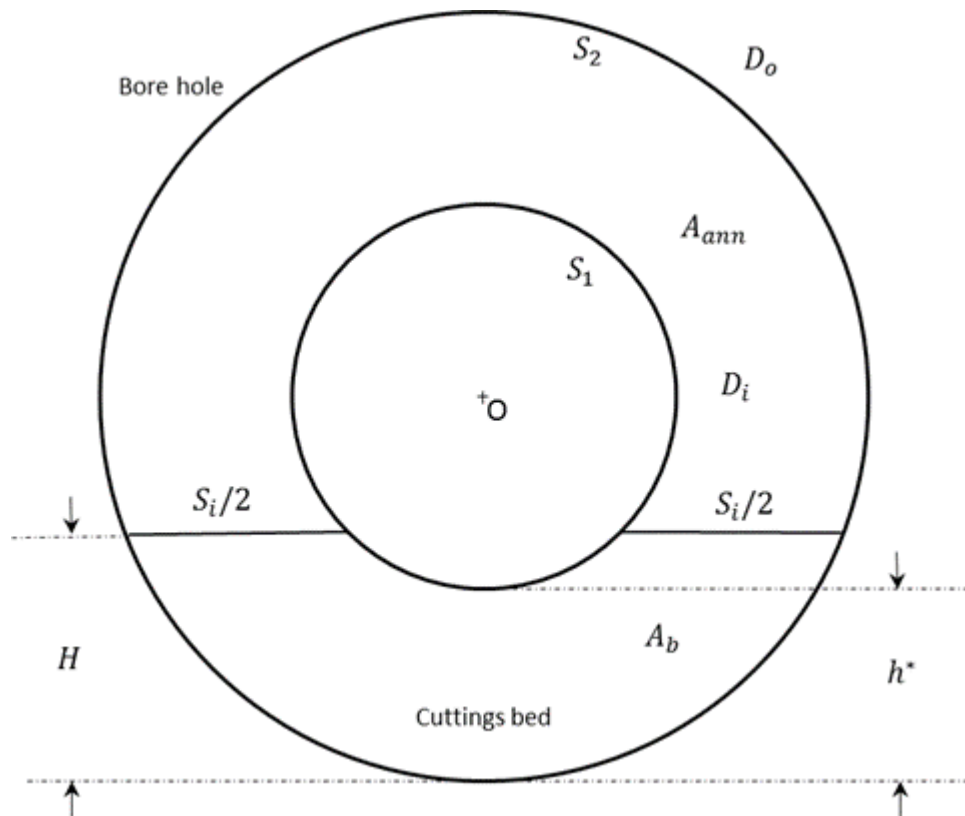


Figure D.1 Geometrical analysis (Chen, 2005)

$$D_h = (D_o - D_i)(1 - e) \quad (\text{D-2})$$

$$D_h = h^* \quad (\text{D-3})$$

$$S_1 = D_i \cdot \pi, \text{ if } H \leq 0.5 \cdot D_h \quad (\text{D-4})$$

$$S_1 = 0, \text{ if } H \geq D_i + 0.5 \cdot D_h \quad (\text{D-5})$$

$$S_1 = D_i \left(\pi - \cos^{-1} \left[1 - \frac{2(H - 0.5D_h)}{d_i} \right] \right) \text{ if } 0.5 \leq H \leq D_i + 0.5 \cdot D_h \quad (\text{D-6})$$

$$S_2 = D_o \left(\pi - \cos^{-1} \left(1 - \frac{2H}{D_o} \right) \right) \quad (\text{D-7})$$

$$S_i = 2\sqrt{H(D_o - H)} \text{ if } 0 \leq H \leq 0.5 \cdot D_h \quad (\text{D-8})$$

$$S_i = 2\sqrt{H(D_o - H)} - 2\sqrt{(H - 0.5D_h)(D_i - H + 0.5D_h)} \quad \text{if} \\ 0.5D_h \leq H \leq 0.5 \cdot D_h + D_i \quad (\text{D-9})$$

$$S_i = 2\sqrt{H(D_o - H)} \quad \text{if } 0.5 \cdot D_h + D_i \leq H \leq D_o \quad (\text{D-10})$$

$$L = S_1 + S_2 + S_i \quad (\text{D-11})$$

$$f(d, h) = \frac{d^2}{4} \left[\cos^{-1} \left(1 - \frac{2h}{d} \right) - 2 \left(1 - \frac{2h}{d} \right) \sqrt{\frac{h}{d} \left(1 - \frac{h}{d} \right)} \right] \quad (\text{D-12})$$

$$A_b = f(D_o, H) \quad \text{if } 0 \leq H \leq 0.5D_h \quad (\text{D-13})$$

$$A_b = f(D_o, H) - f(D_i, H - 0.5D_h) \quad \text{if } 0.5D_h \leq H \leq D_i + 0.5D_h \quad (\text{D-14})$$

$$A_b = f(D_o, H) - \frac{\pi}{4} D_i^2 \quad \text{if } D_i + 0.5D_h \leq H \leq D_o \quad (\text{D-15})$$

The Annular area is defined as:

$$A_{ann} = \frac{\pi}{4} (D_o^2 - D_i^2) - A_b \quad (\text{D-16})$$

**Existing correlation model for PL fluid in concentric annulus with cuttings bed
(Exlog Solution)**

The existing correlation is based on the widely accepted model known as Exlog solution (Whitaker, 1985). The model predicts pressure loss in a partially blocked concentric annulus for PL fluids. Hence, the pressure loss is determined from Eqn. D-17 (Chen, 2005):

$$\frac{D_{hyd}}{4} \frac{dP}{dL} = K(G(Z, n))^n \tau_w \quad (D-17)$$

Where the wall shear stress for PL fluid is calculated from the constitutive equation:

$$\tau_w = K \left(\frac{8U}{D_{hyd}} \right)^n \quad (D-18)$$

G is a Geometric factor, which is a function of parameters Z and n :

$$G = \frac{(3-Z)n+1}{(4-Z)n} \left(1 + \frac{Z}{2} \right) \quad (D-19)$$

Z is a dummy variable defined as:

$$Z = 1 - (1 - \kappa^{Y^*})^{1/Y^*} \quad (D-20)$$

where Y^* is expressed as:

$$Y^* = 0.37n^{-0.14} \quad (D-21)$$

Chen (2005) introduced an effective diameter, which is related to the hydraulic diameter and the geometric factor G as:

$$D_{eff} = \frac{D_{hyd}}{G} \quad (D-22)$$

In this study, in order to account for eccentricity, the Exlog model pressure-loss predictions are corrected using a model developed by Hacıislamoglu and Langlinais (1990), which related pressure loss in concentric annulus to that of eccentric annulus.

Thus:

$$\left(\frac{dP}{dL}\right)_e = \left(1 - 0.072\kappa^{0.8454}\frac{e}{n} - 1.5e^2\kappa^{0.1852}\sqrt{n} + 0.96e^3\sqrt{n}\right)\left(\frac{dP}{dL}\right)_c \quad (\text{D-23})$$

Equation (D-23) is valid for wide ranges of power law indexes (0.4 and 1.0), eccentricities (0 to 0.95) and diameter ratios (0.3 to 0.9).

Appendix E: Bed Shear Stress and Velocity Profiles

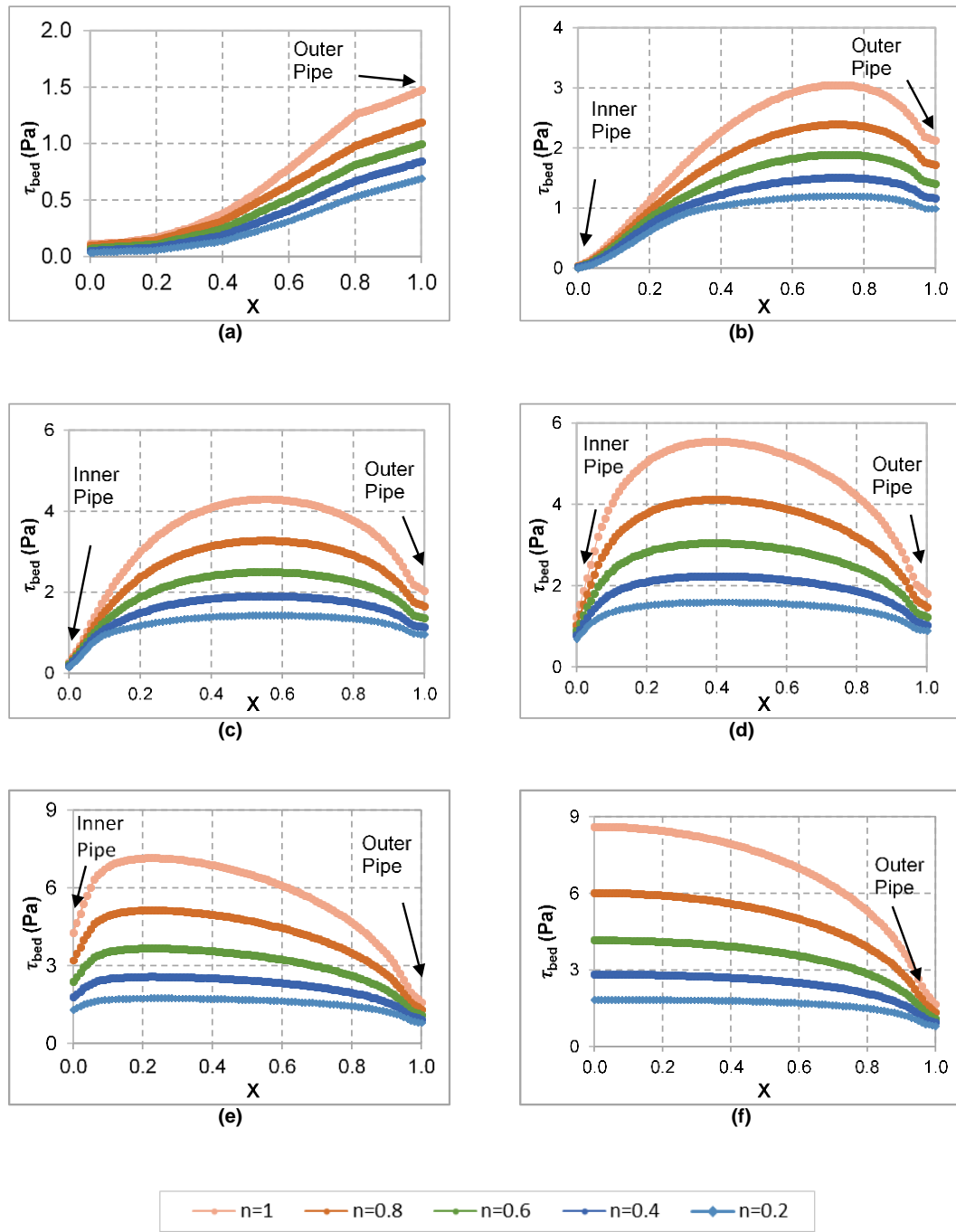


Figure E.1 τ_{bed} vs. X . a) $H_{bed}=10\%$; b) $H_{bed}=30\%$; c) $H_{bed}=50\%$; d) $H_{bed}=70\%$; e) $H_{bed}=90\%$; f) $H_{bed}=100\%$ ($e=0.9, \kappa=0.25$)

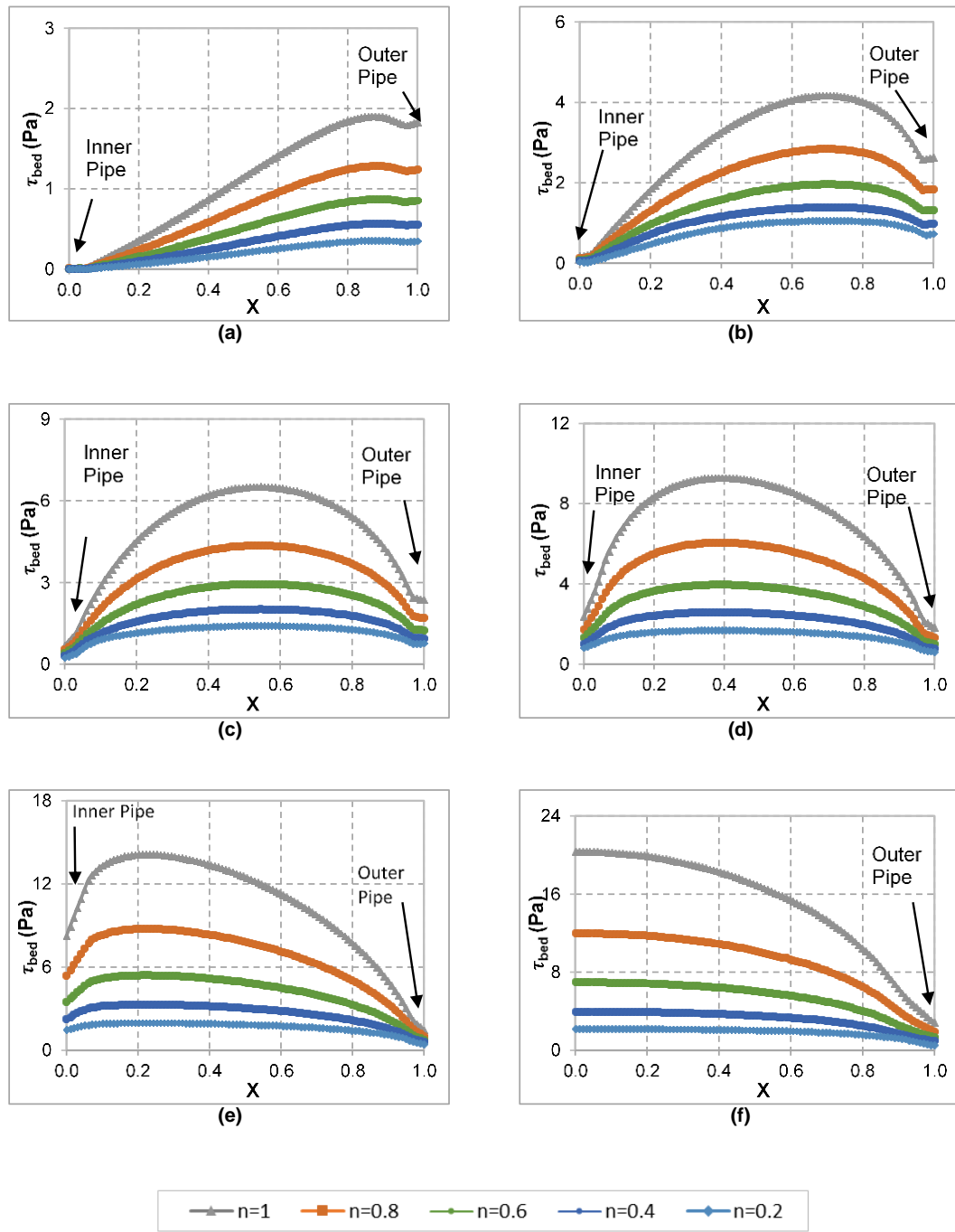


Figure E.2 τ_{bed} vs. X . a) $H_{bed} = 10\%$; b) $H_{bed} = 30\%$; c) $H_{bed} = 50\%$; d) $H_{bed} = 70\%$; e) $H_{bed} = 90\%$; f) $H_{bed} = 100\%$ ($\epsilon = 0.9, \kappa = 0.50$)

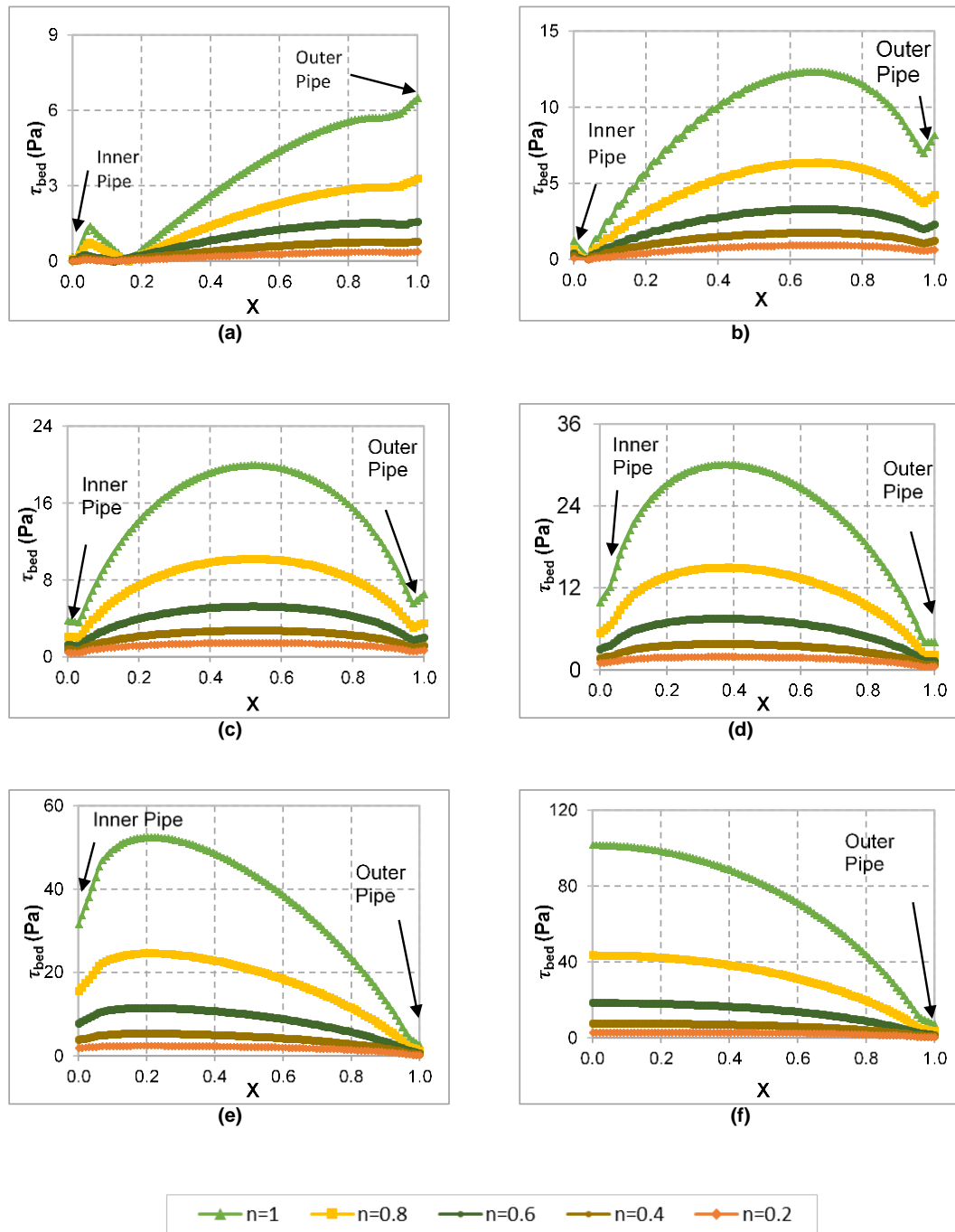


Figure E.3 τ_{bed} vs. X . a) $H_{bed}=10\%$; b) $H_{bed}=30\%$; c) $H_{bed}=50\%$; d) $H_{bed}=70\%$; e) $H_{bed}=90\%$; f) $H_{bed}=100\%$ ($e=0.9$, $\kappa=0.75$)

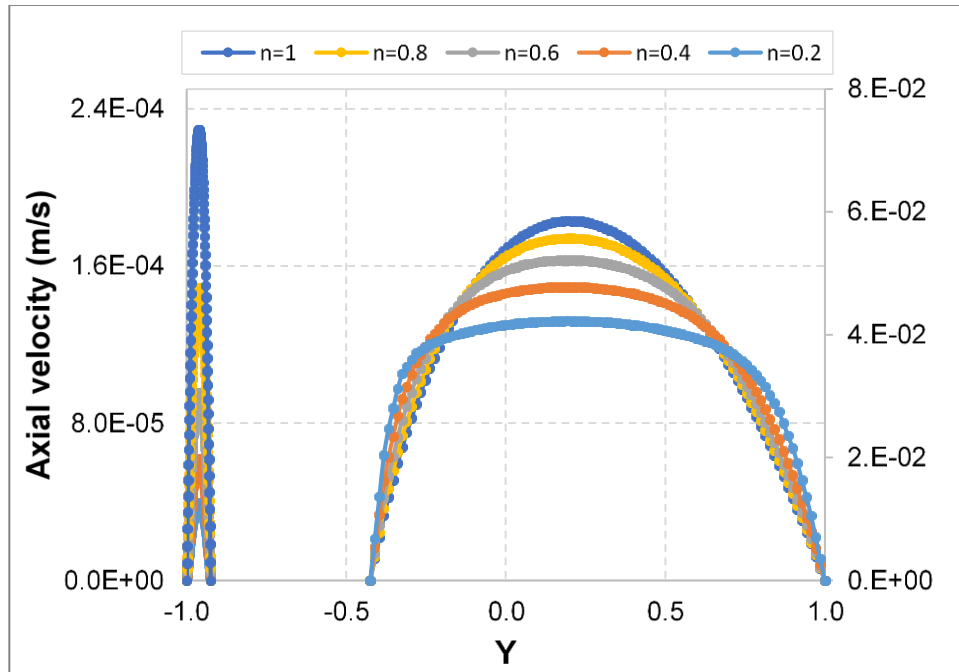


Figure E.4 Axial velocity vs. Y . a) $H_{bed} = 0\%$ ($e=0.90$, $\kappa=0.25$)

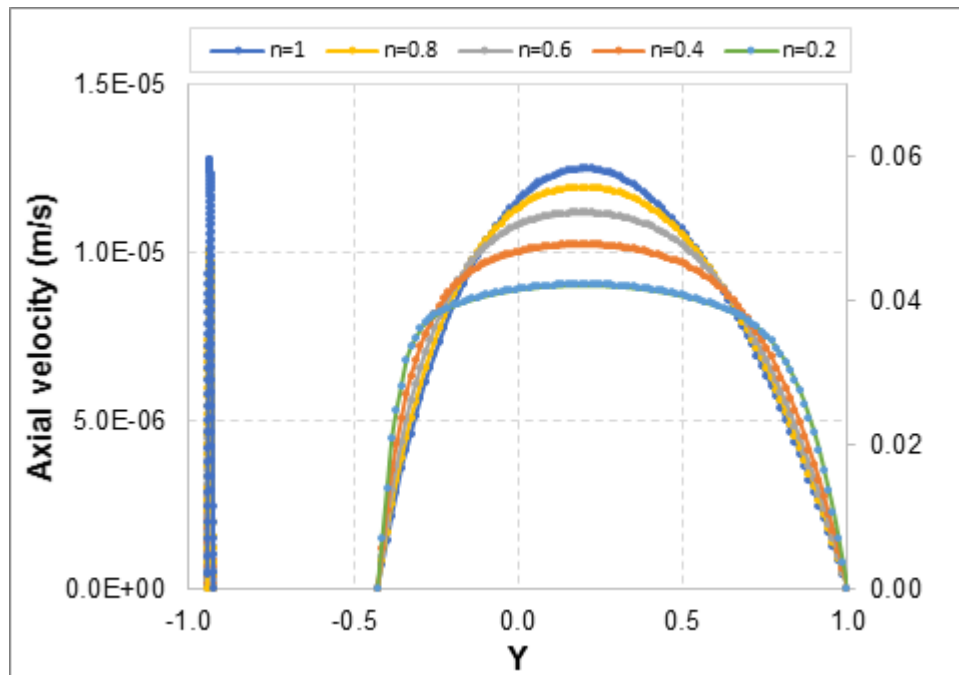


Figure E.5 Axial velocity vs. Y . a) $H_{bed} = 10\%$ ($e=0.9$, $\kappa=0.25$)

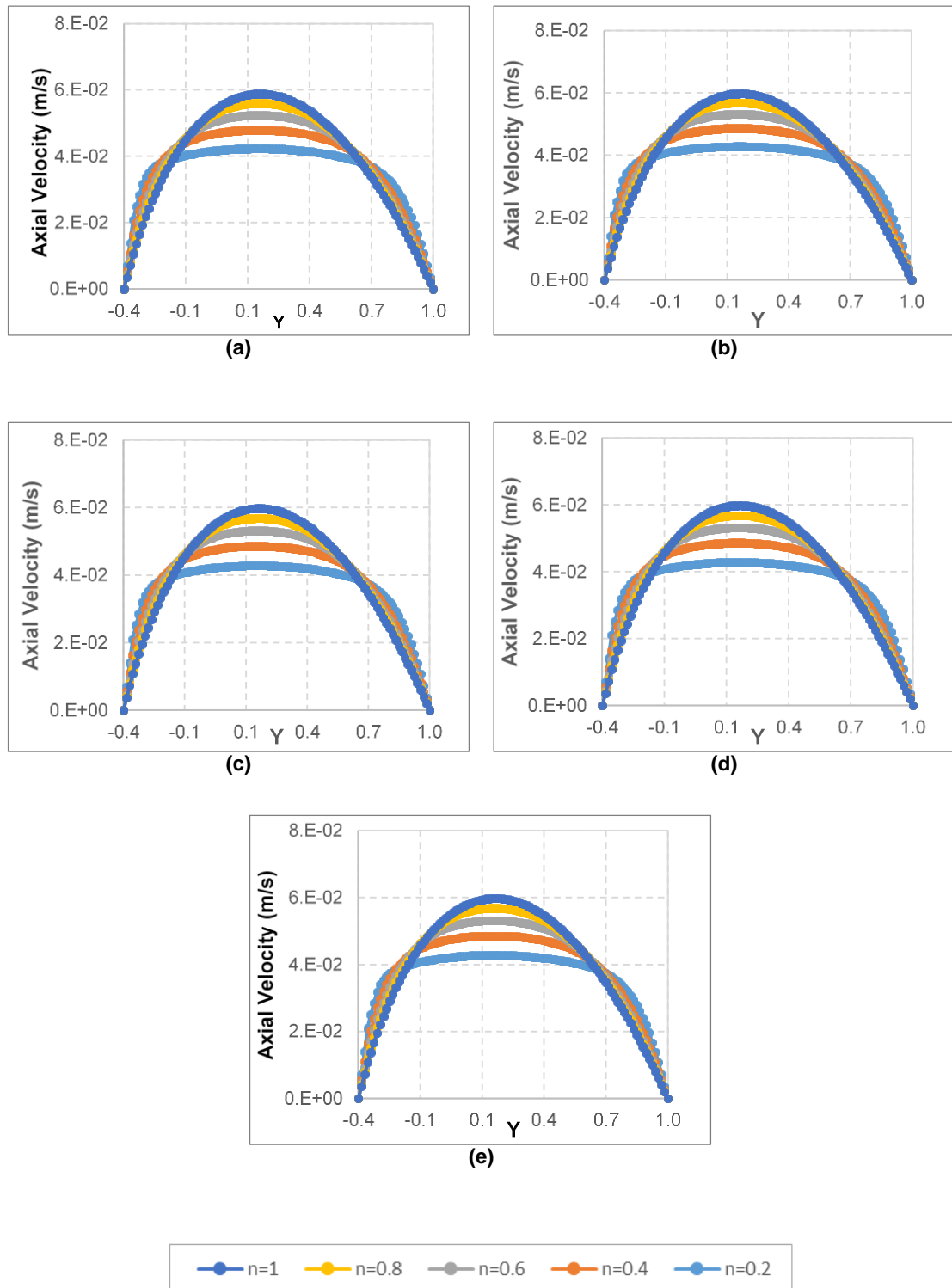


Figure E.6 Axial velocity vs. Y . a) $H_{bed} = 30\%$; b) $H_{bed} = 50\%$; c) $H_{bed} = 70\%$; d) $H_{bed} = 90\%$; e) $H_{bed} = 100\%$ ($e=0.9, \kappa=0.25$)

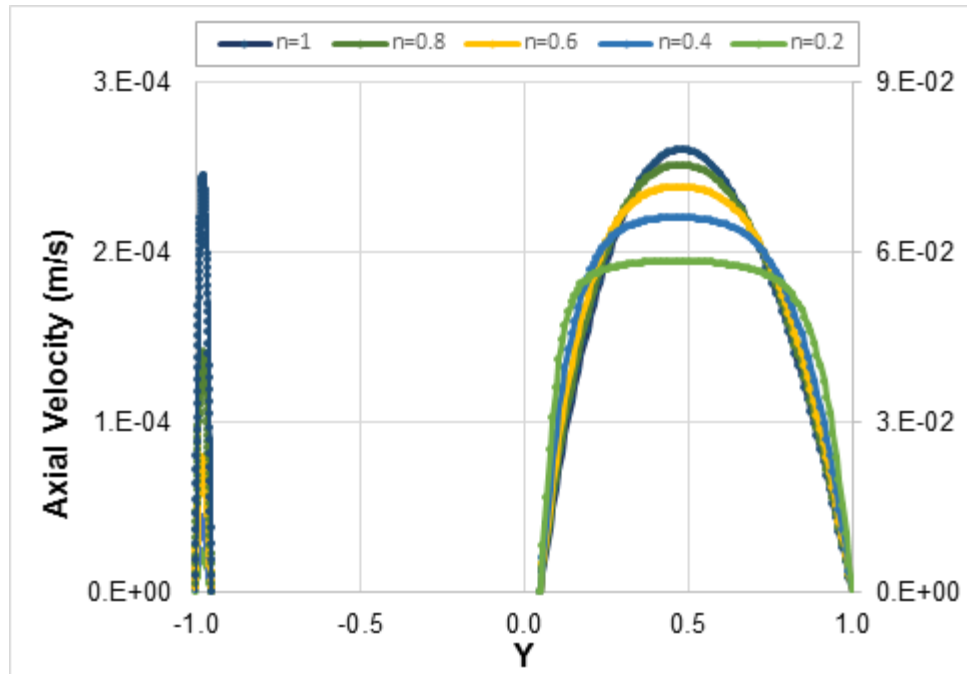


Figure E.7 Axial velocity vs. Y . a) $H_{bed} = 0$ ($e=0.9$, $\kappa=0.50$)

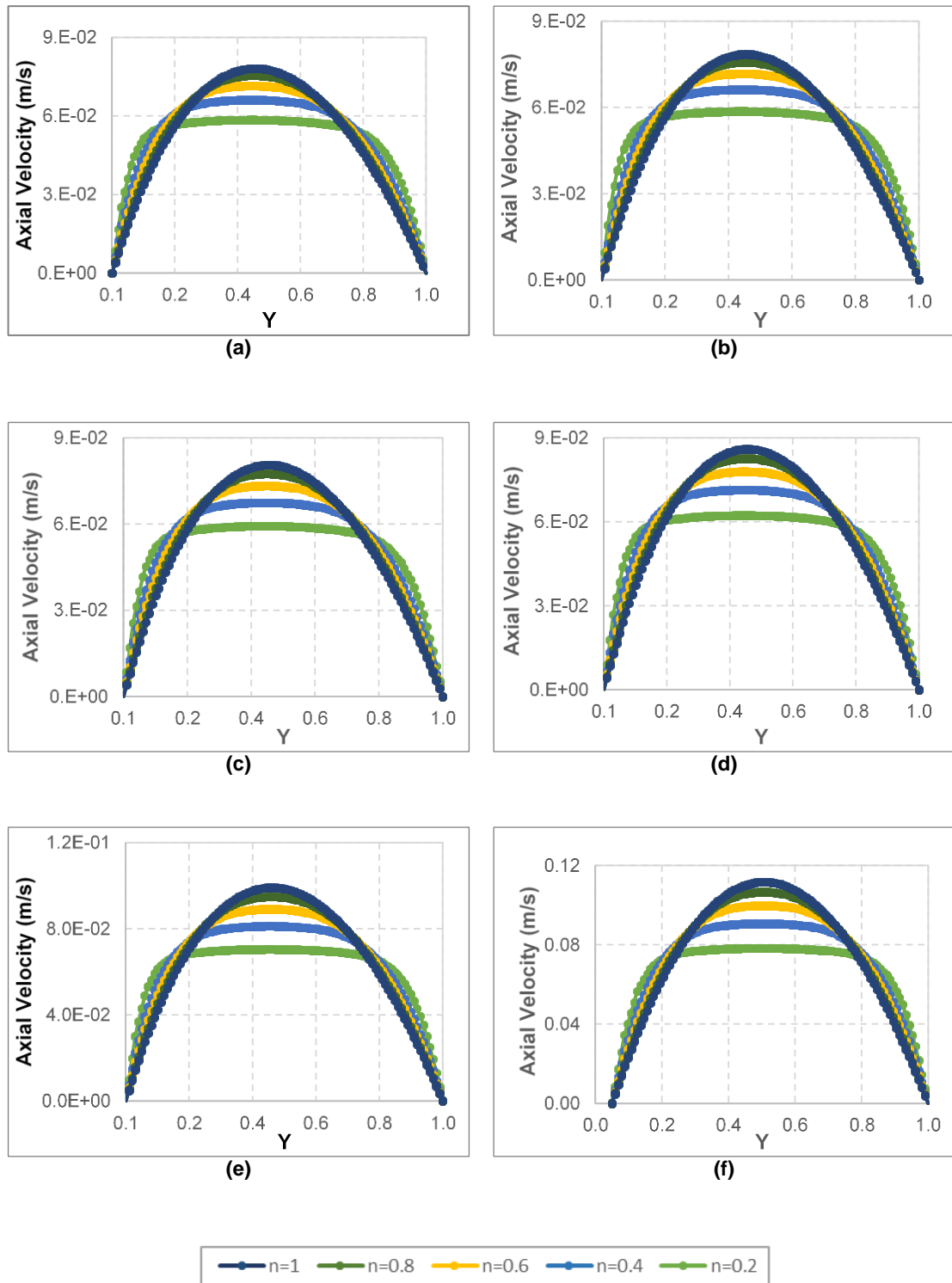


Figure E.8 Axial velocity vs. Y . a) $H_{bed} = 10\%$; b) $H_{bed} = 30\%$; c) $H_{bed} = 50\%$; d) $H_{bed} = 70\%$; e) $H_{bed} = 90\%$; f) $H_{bed} = 100\%$ ($e=0.9$, $\kappa=0.50$)

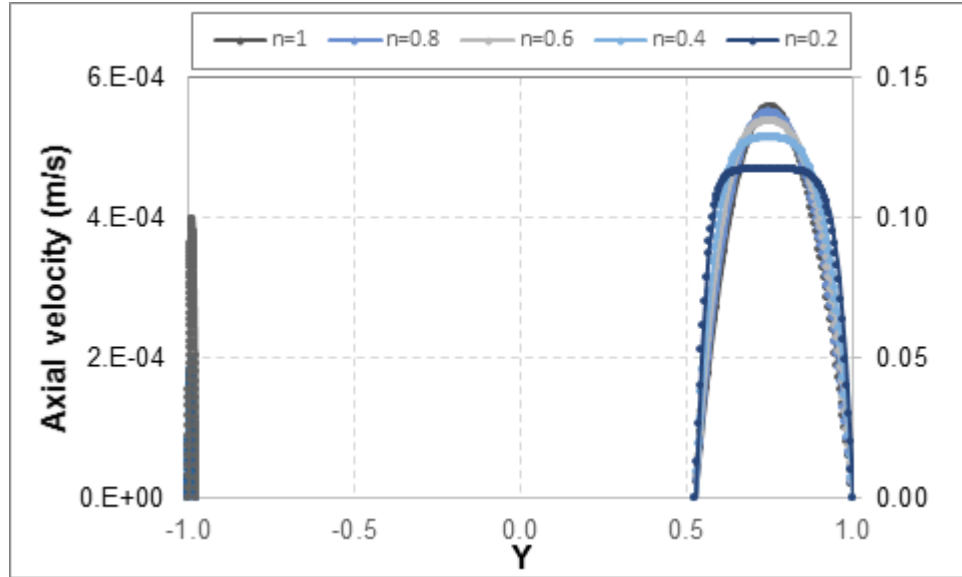


Figure E.9 Axial velocity vs. Y . a) $H_{bed} = 0\%$ ($e=0.9$, $\kappa=0.75$)

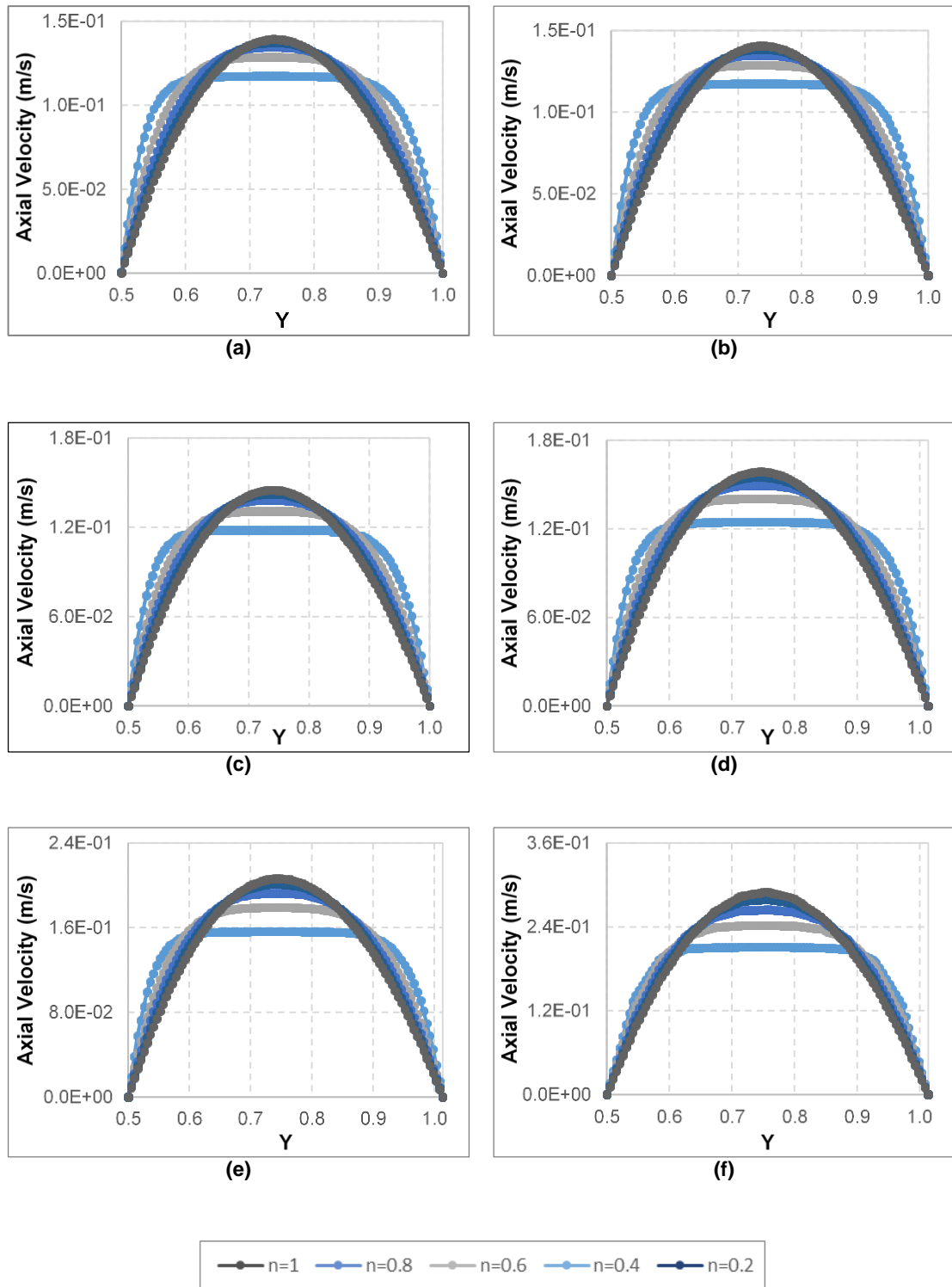


Figure E.10 Axial velocity vs. Y. a) $H_{bed} = 10\%$; b) $H_{bed} = 30\%$; c) $H_{bed} = 50\%$; d) $H_{bed} = 70\%$; e) $H_{bed} = 90\%$; f) $H_{bed} = 100\%$ ($e=0.9$, $\kappa=0.75$)

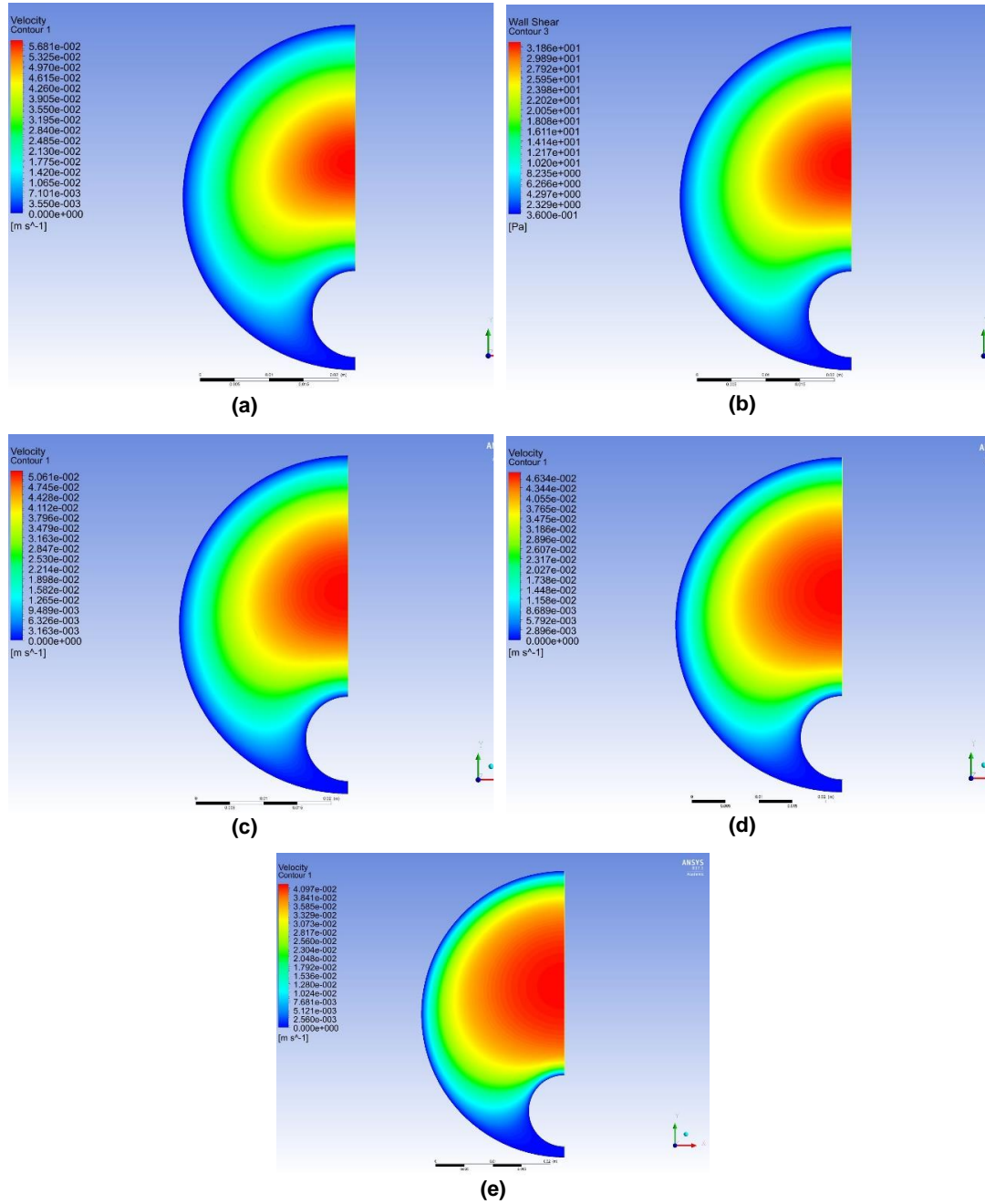
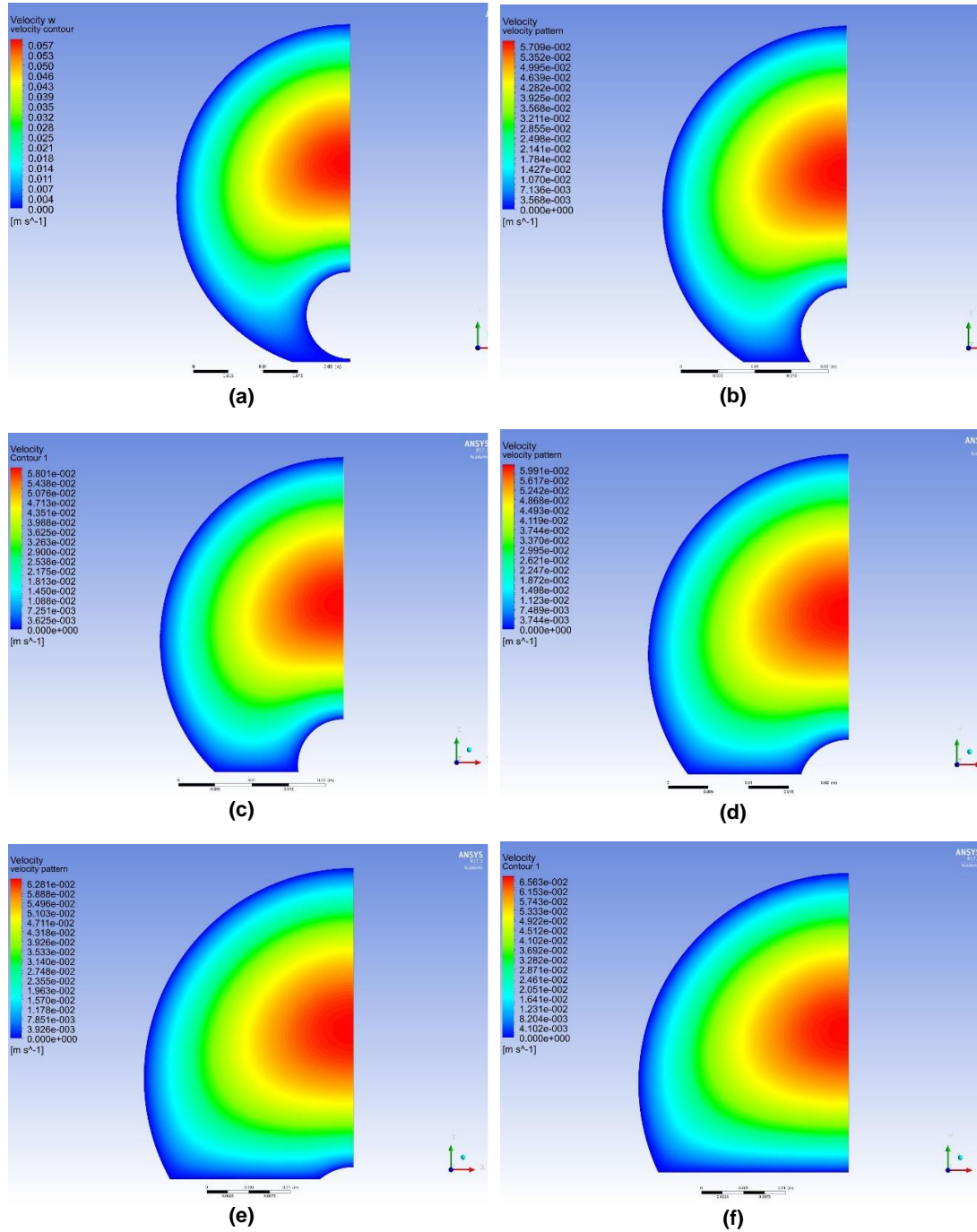
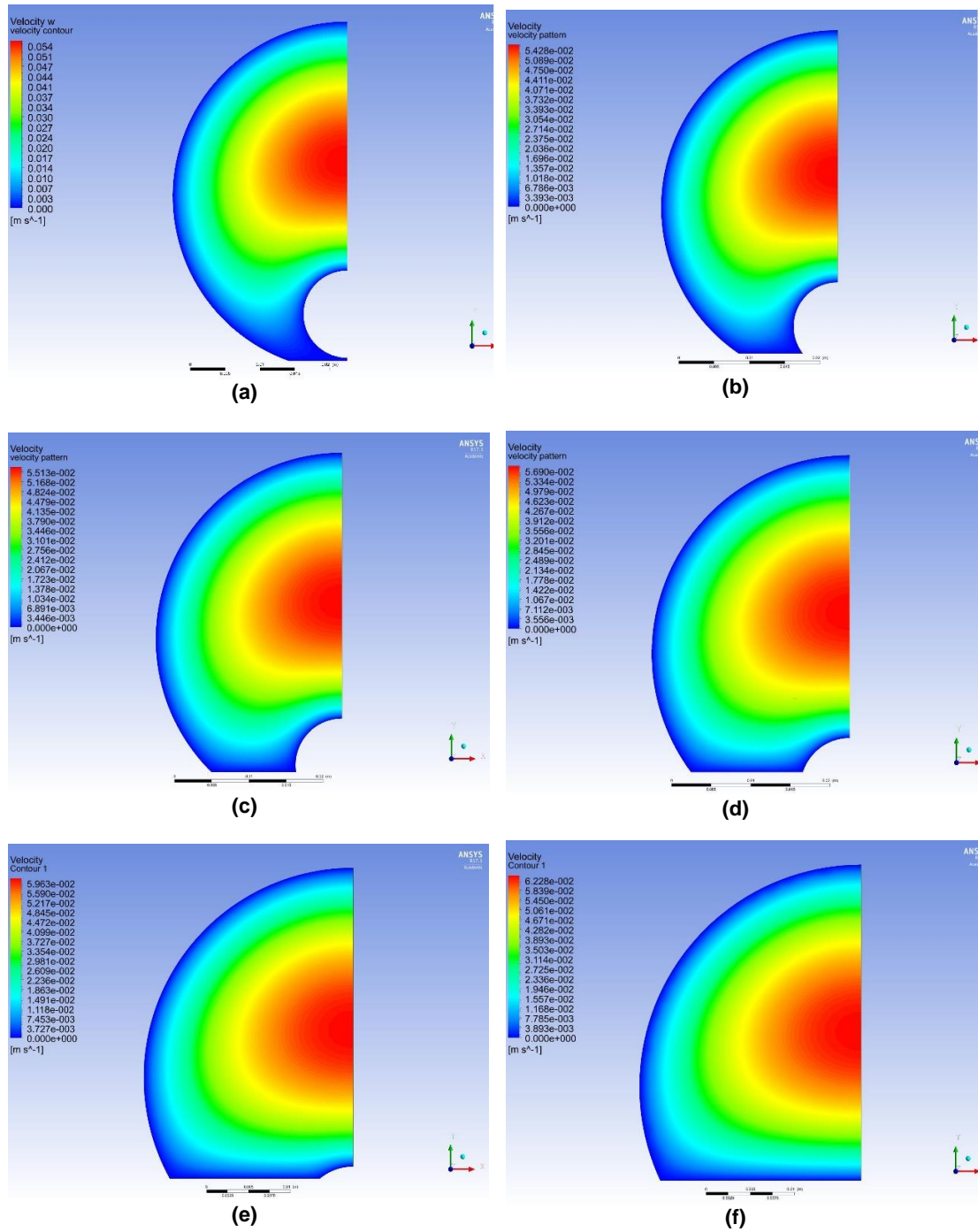


Figure E.11 Velocity Contour: a) $n=1$; b) $n=0.8$; c) $n=0.6$; d) $n=0.4$; e) $n=0.2$ ($e=0.9$, $H_{\text{bed}}=0\%$, $\kappa=0.25$)



**Figure E.12 Velocity contour: a) $H_{bed} = 10\%$; b) $H_{bed} = 30\%$; c) $H_{bed} = 50\%$; d) $H_{bed} = 70\%$;
 e) $H_{bed} = 90\%$; f) $H_{bed} = 100\%$ ($e=0.9$, $n=1$, $\kappa=0.25$)**



**Figure E.13 Velocity contour: a) $H_{bed}=10\%$; b) $H_{bed}=30\%$; c) $H_{bed}=50\%$; d) $H_{bed}=70\%$;
 e) $H_{bed}=90\%$; f) $H_{bed}=100\%$ ($e=0.9$, $n=0.8$, $\kappa=0.25$)**

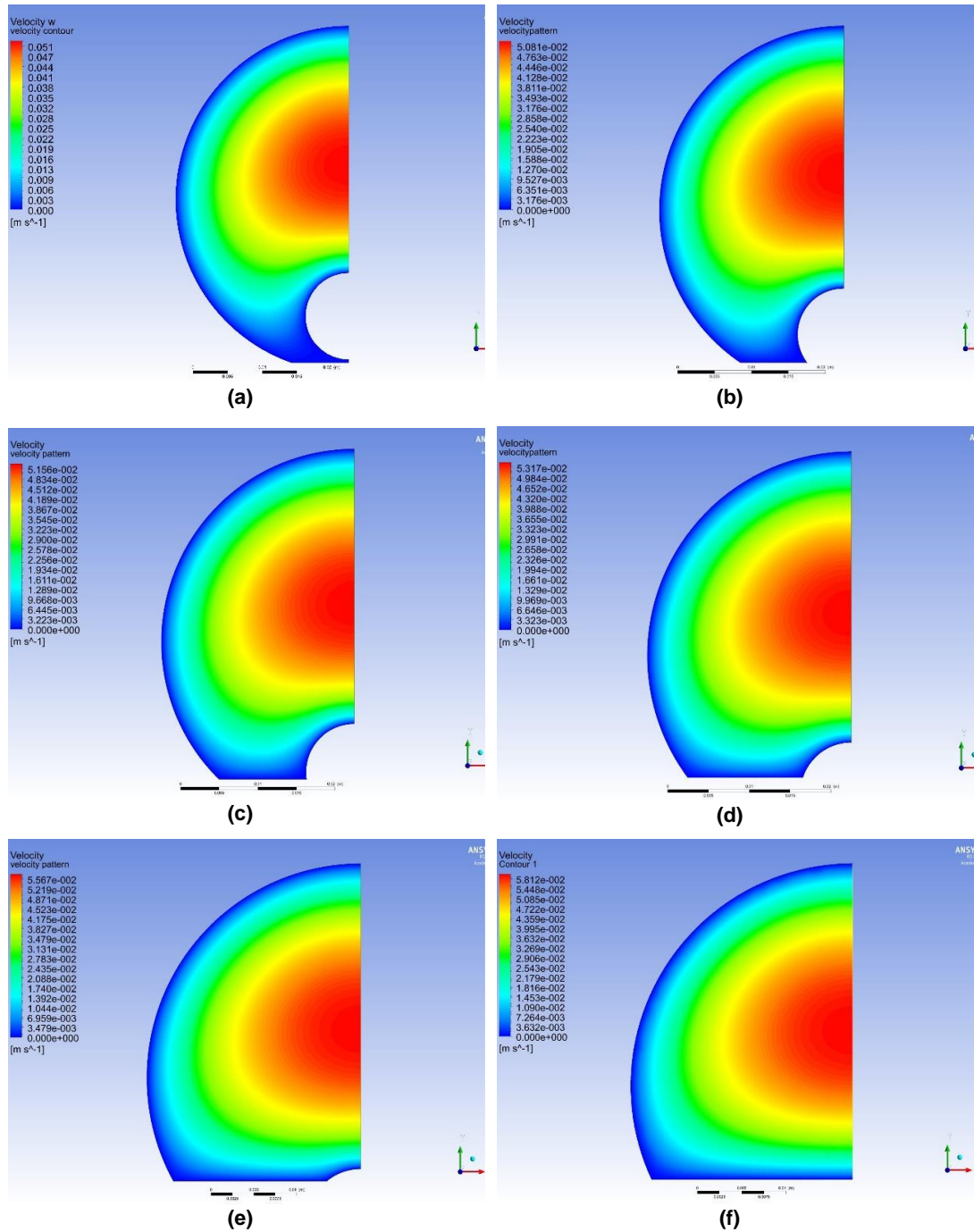


**Figure E.14 Velocity contour: a) $H_{bed}=10\%$; b) $H_{bed}=30\%$; c) $H_{bed}=50\%$; d) $H_{bed}=70\%$;
 e) $H_{bed}=90\%$; f) $H_{bed}=100\%$ ($e=0.9$, $n=0.6$, $\kappa=0.25$)**

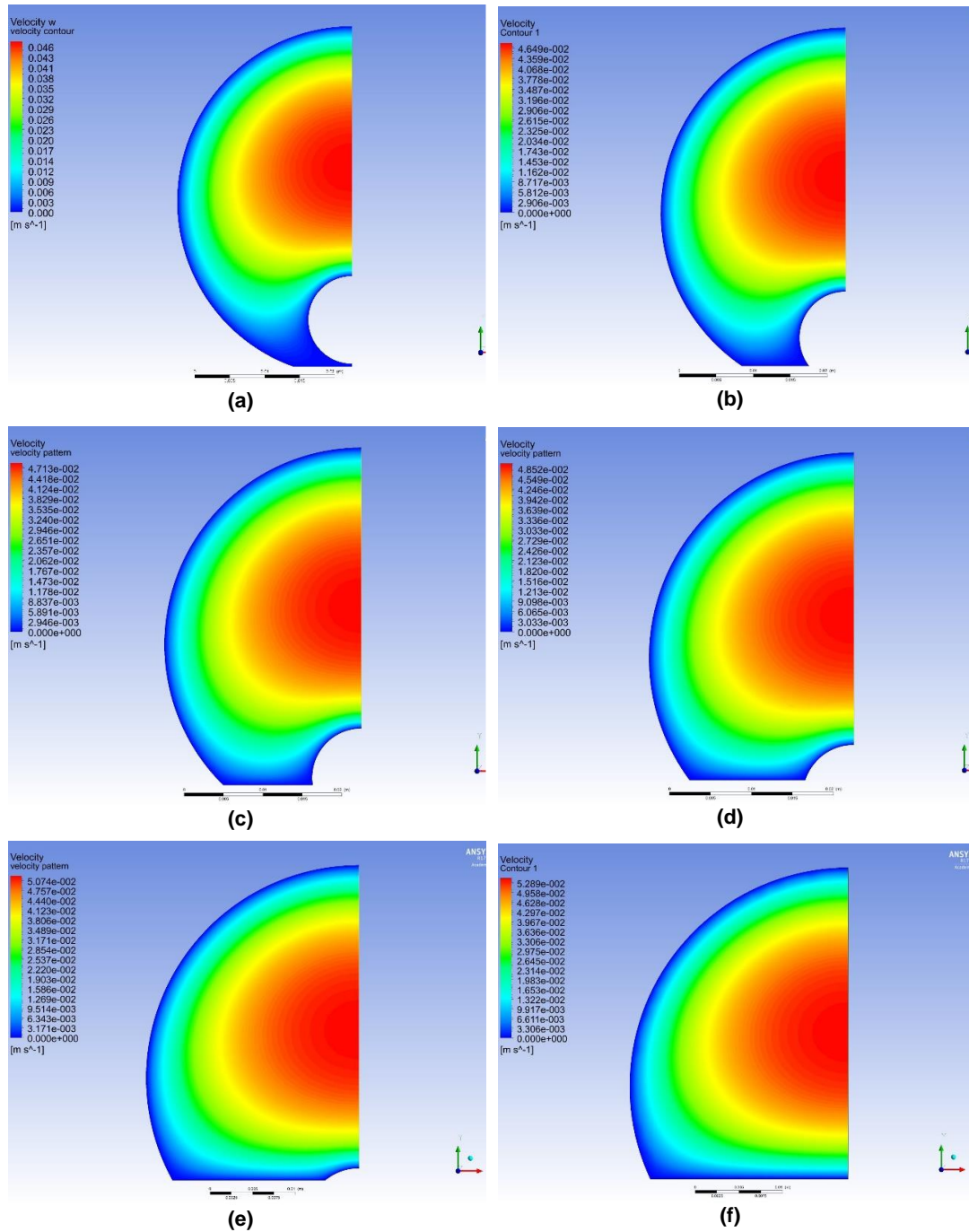


**Figure E.15 Velocity contour: a) $H_{bed} = 10\%$; b) $H_{bed} = 30\%$; c) $H_{bed} = 50\%$; d) $H_{bed} = 70\%$;
 e) $H_{bed} = 90\%$; f) $H_{bed} = 100\%$ ($e=0.9$, $n=0.4$, $\kappa=0.25$)**

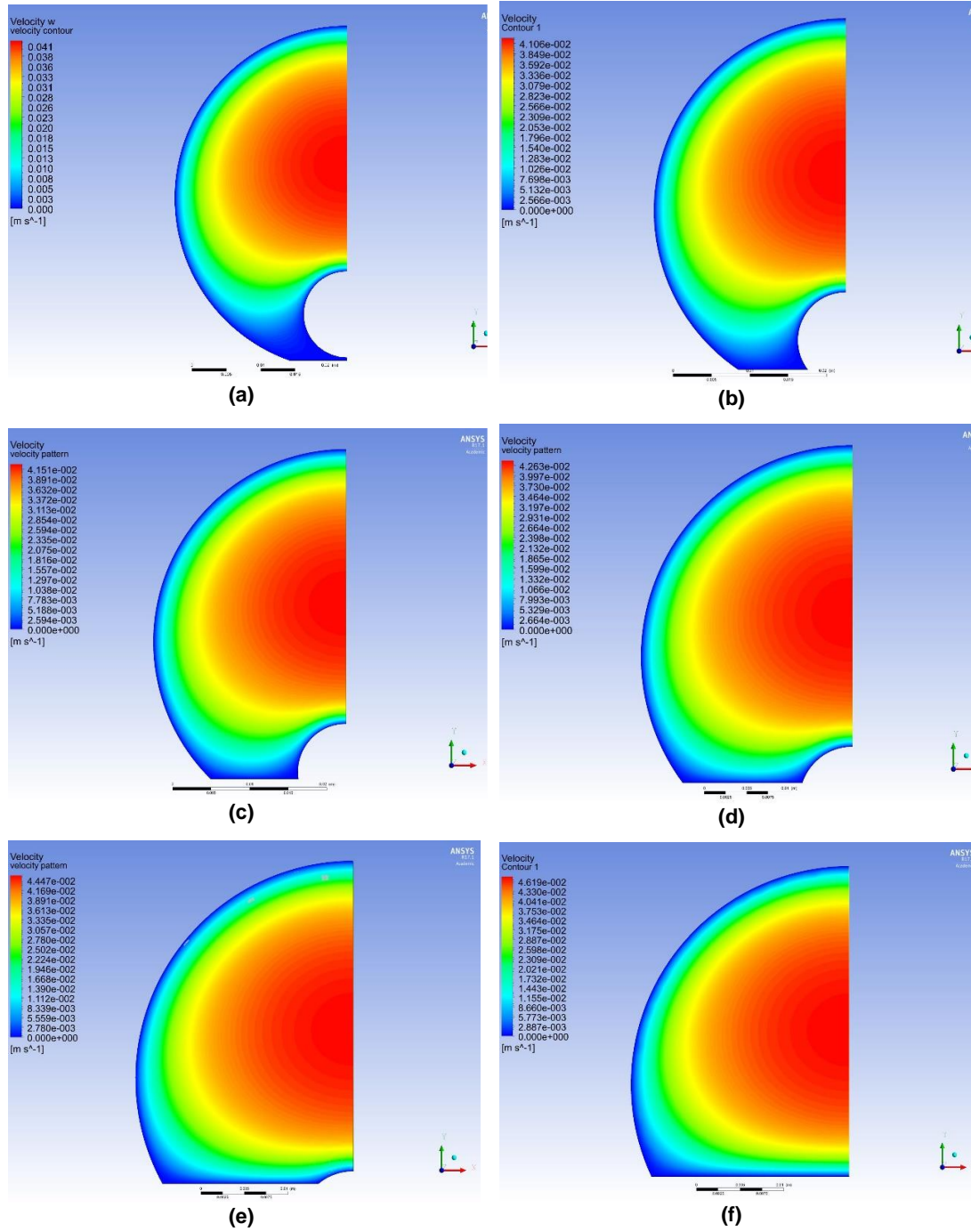


Figure E.16 Velocity contour: a) $H_{bed} = 10\%$; b) $H_{bed} = 30\%$; c) $H_{bed} = 50\%$; d) $H_{bed} = 70\%$;

e) $H_{bed} = 90\%$; f) $H_{bed} = 100\%$ ($e=0.9$, $n=0.2$, $\kappa=0.25$)

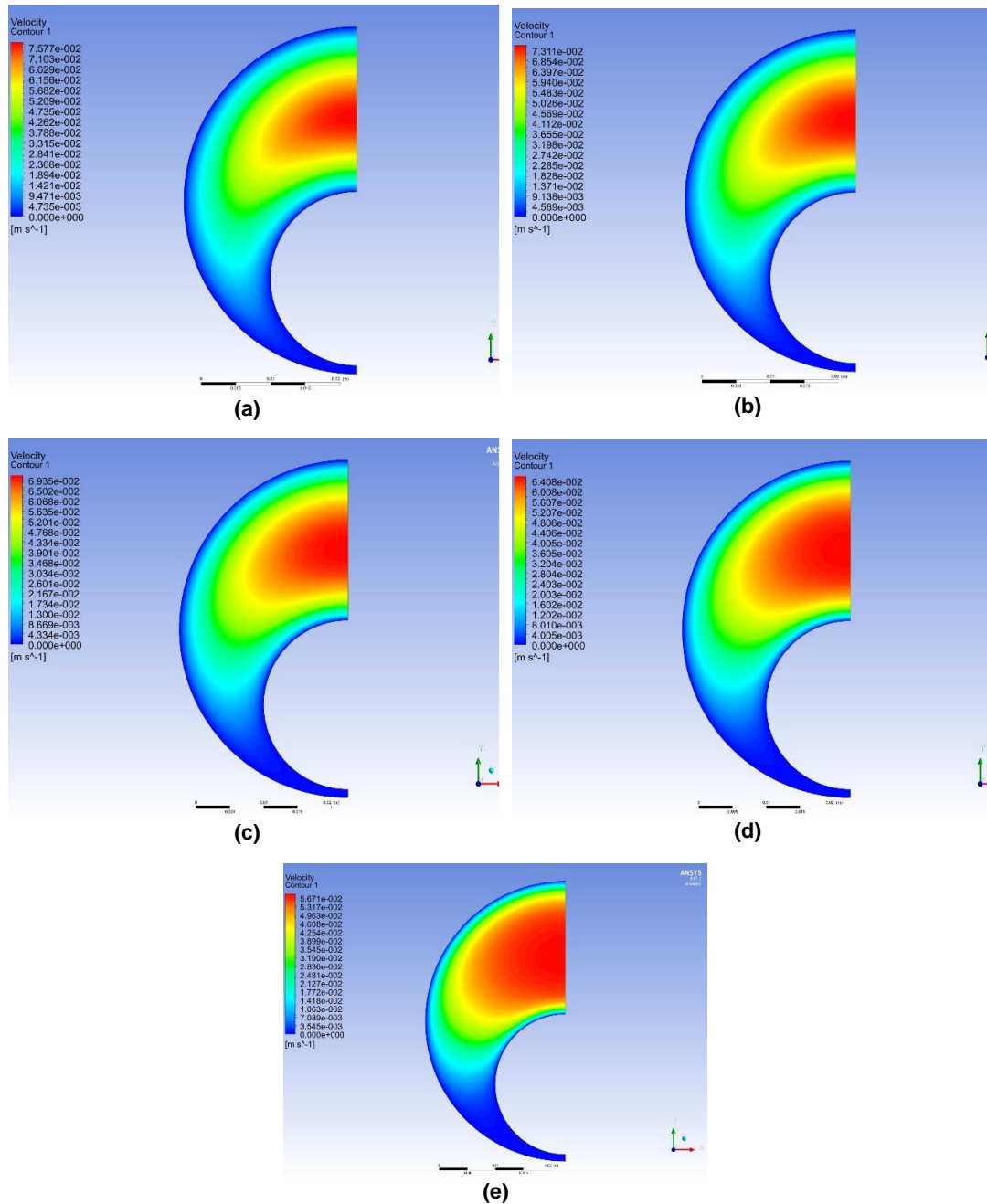


Figure E.17 Velocity Contour: a) $n=1$; b) $n=0.8$; c) $n=0.6$; d) $n=0.4$; e) $n=0.2$ ($e=0.9$, $H_{bed} = 0\%$, $\kappa=0.5$)

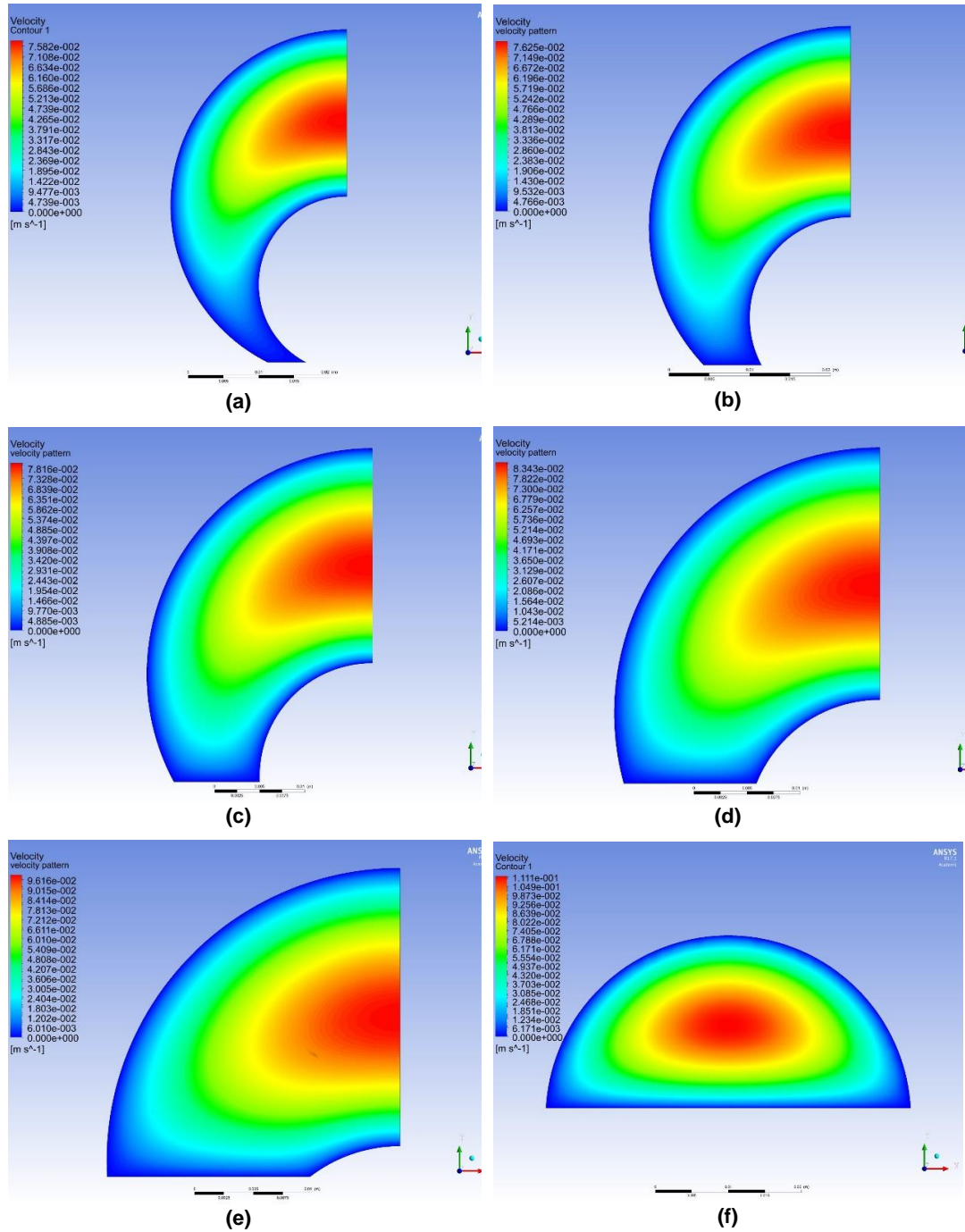


Figure E.18 Velocity Contour: a) $H_{bed}=10\%$; b) $H_{bed} = 30\%$; c) $H_{bed} = 50\%$; d) $H_{bed} = 70\%$; e) $H_{bed}= 90\%$; f) $H_{bed} =100\%$ ($e=0.9$, $n=1$, $\kappa=0.5$)

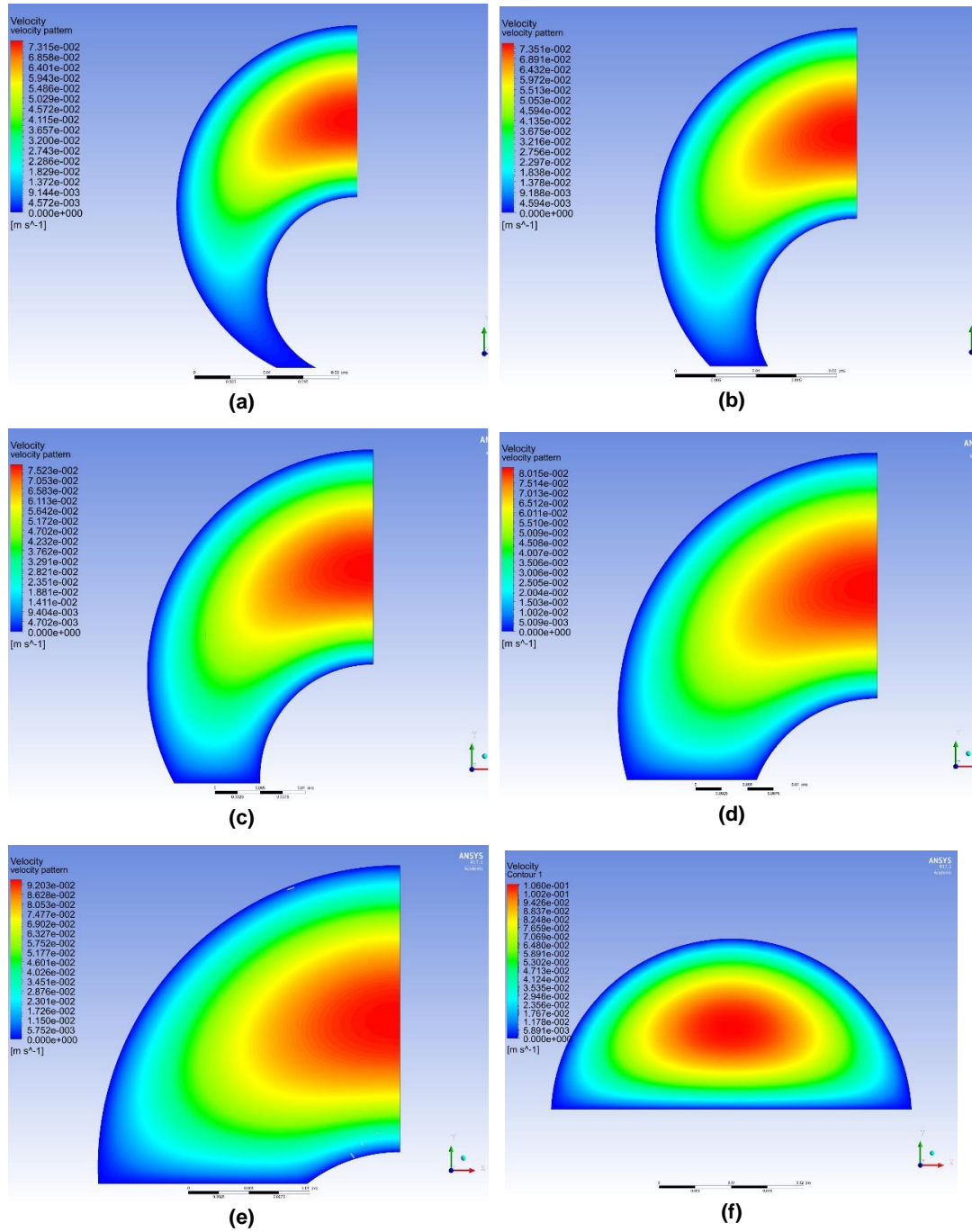


Figure E.19 Velocity Contour: a) $H_{bed} = 10\%$; b) $H_{bed} = 30\%$; c) $H_{bed} = 50\%$; d) $H_{bed} = 70\%$; e) $H_{bed} = 90\%$; f) $H_{bed} = 100\%$ ($e=0.9$, $n=0.8$, $\kappa=0.5$)

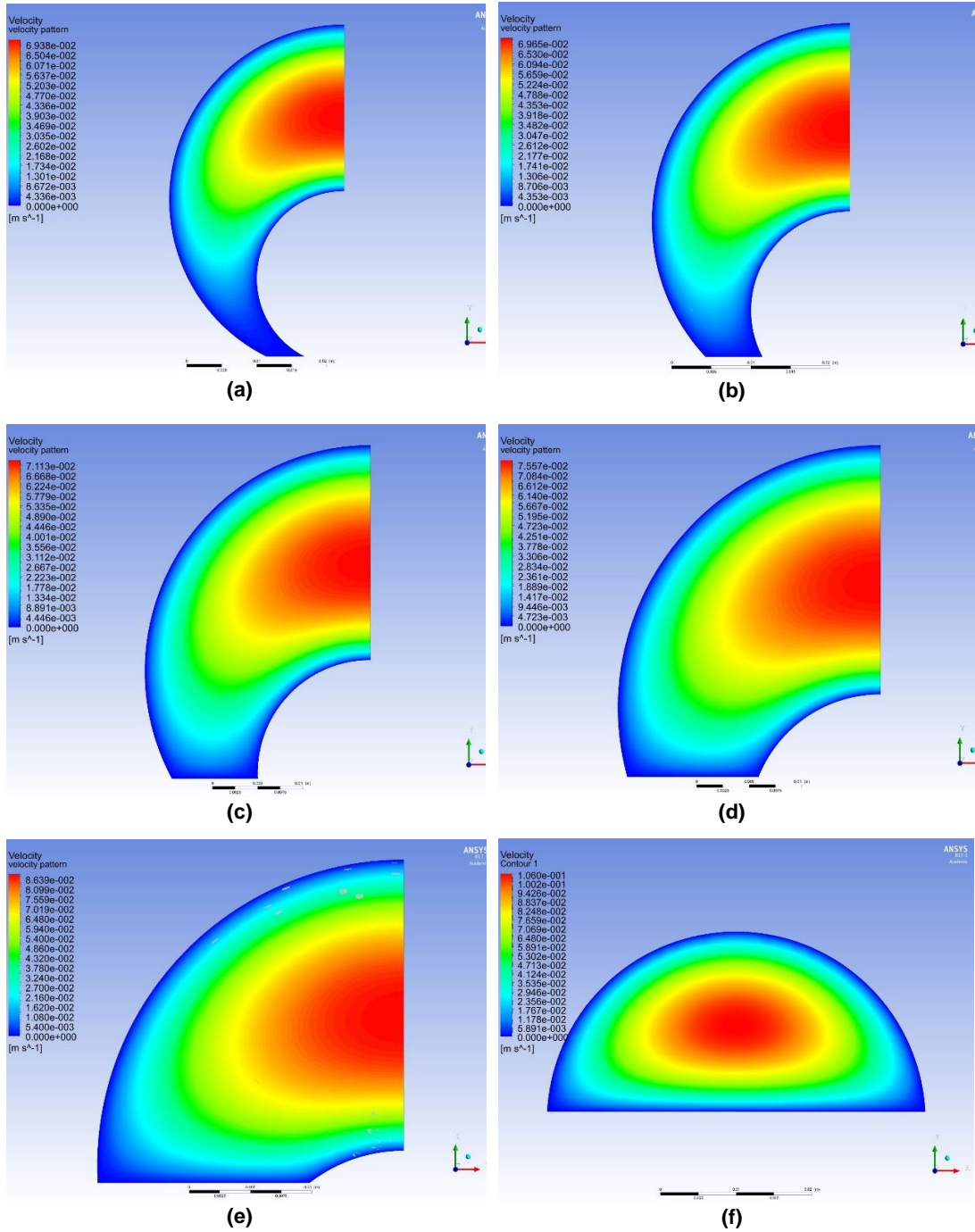


Figure E.20 Velocity Contour: a) $H_{bed} = 10\%$; b) $H_{bed} = 30\%$; c) $H_{bed} = 50\%$; d) $H_{bed} = 70\%$; e) $H_{bed} = 90\%$; f) $H_{bed} = 100\%$ ($e=0.9$, $n=0.6$, $\kappa=0.5$)

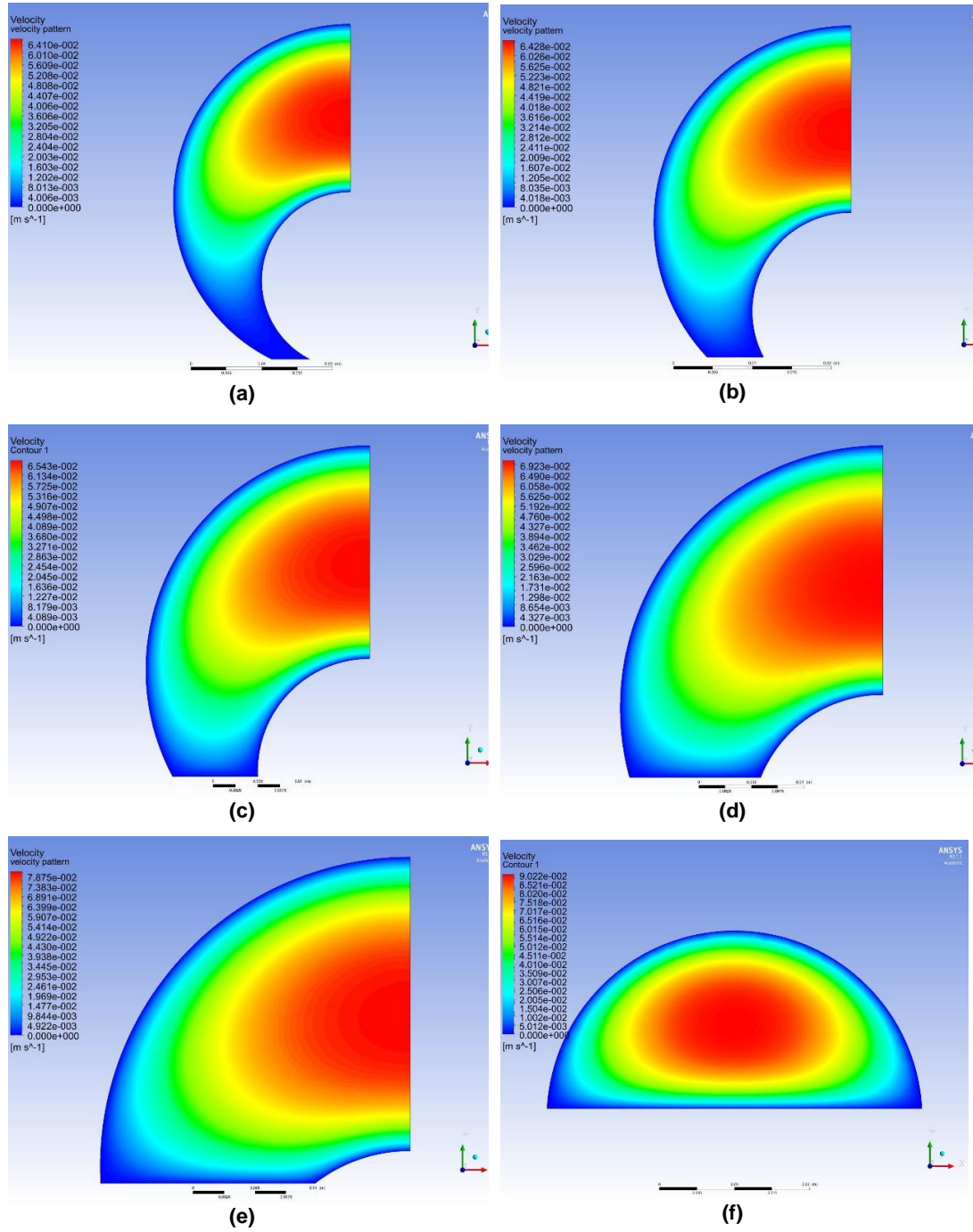
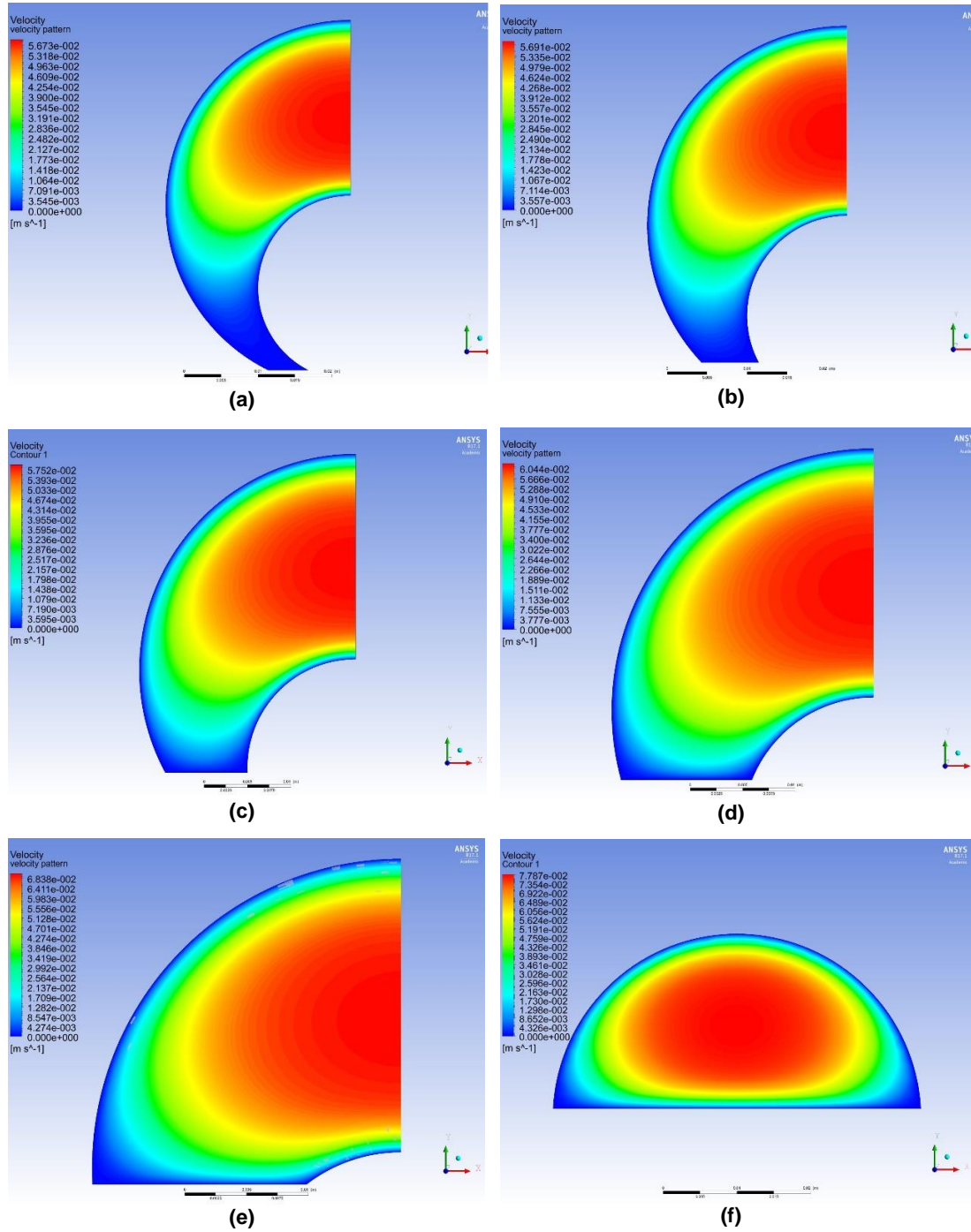


Figure E.21 Velocity Contour: a) $H_{bed} = 10\%$; b) $H_{bed} = 30\%$; c) $H_{bed} = 50\%$; d) $H_{bed} = 70\%$;

e) $H_{bed} = 90\%$; f) $H_{bed} = 100\%$ ($e=0.9$, $n=0.4$, $\kappa=0.5$)



**Figure E.22 Velocity Contour: a) $H_{bed}=10\%$; b) $H_{bed}=30\%$; c) $H_{bed}=50\%$; d) $H_{bed}=70\%$;
 e) $H_{bed}=90\%$; f) $H_{bed}=100\%$ ($e=0.9$, $n=0.2$, $\kappa=0.5$)**

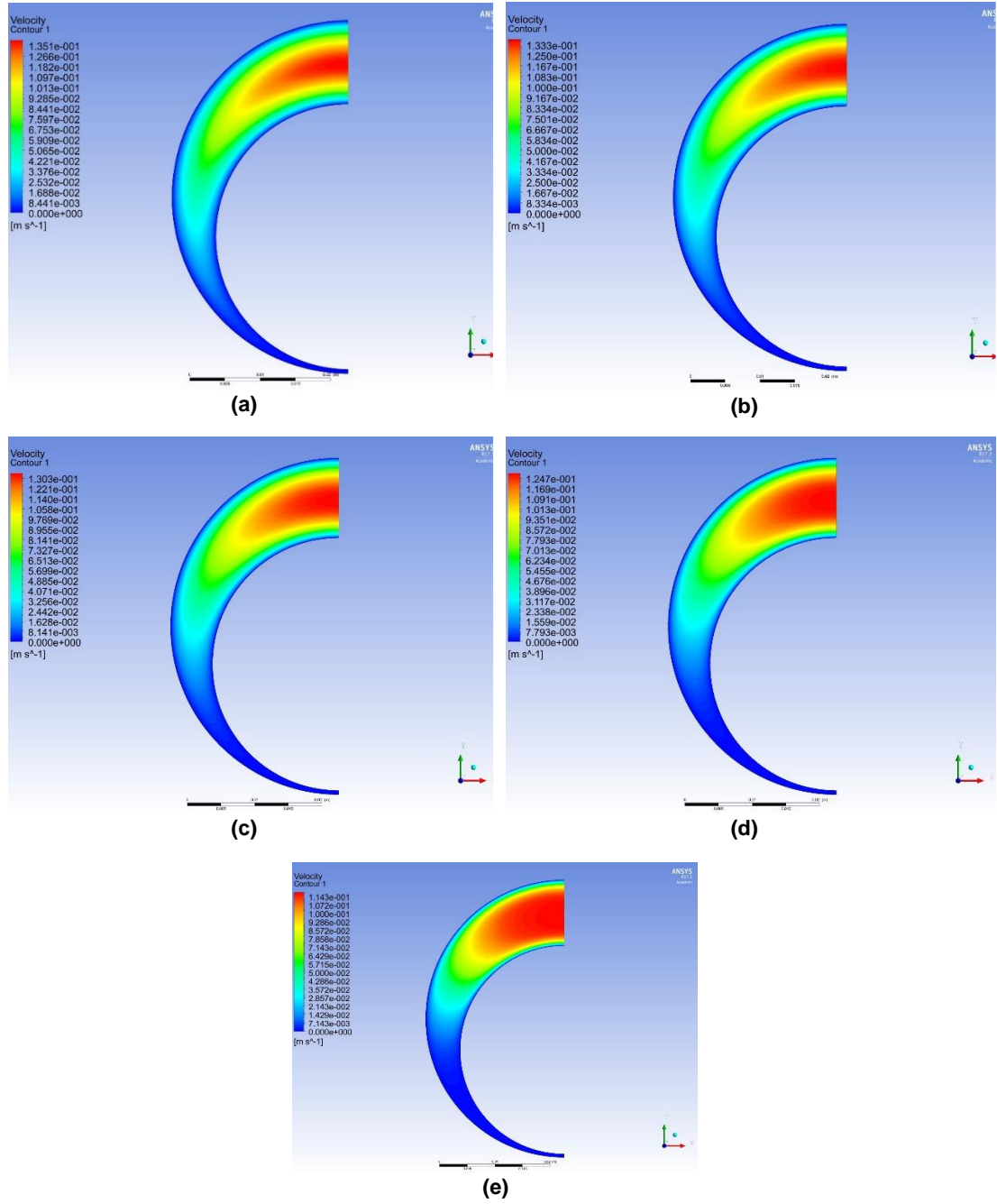


Figure E.23 Velocity Contour: a) $n=1$; b) $n=0.8$; c) $n=0.6$; d) $n=0.4$; e) $n=0.2$ ($e=0.9$, $H_{bed} = 0\%$, $\kappa=0.75$)

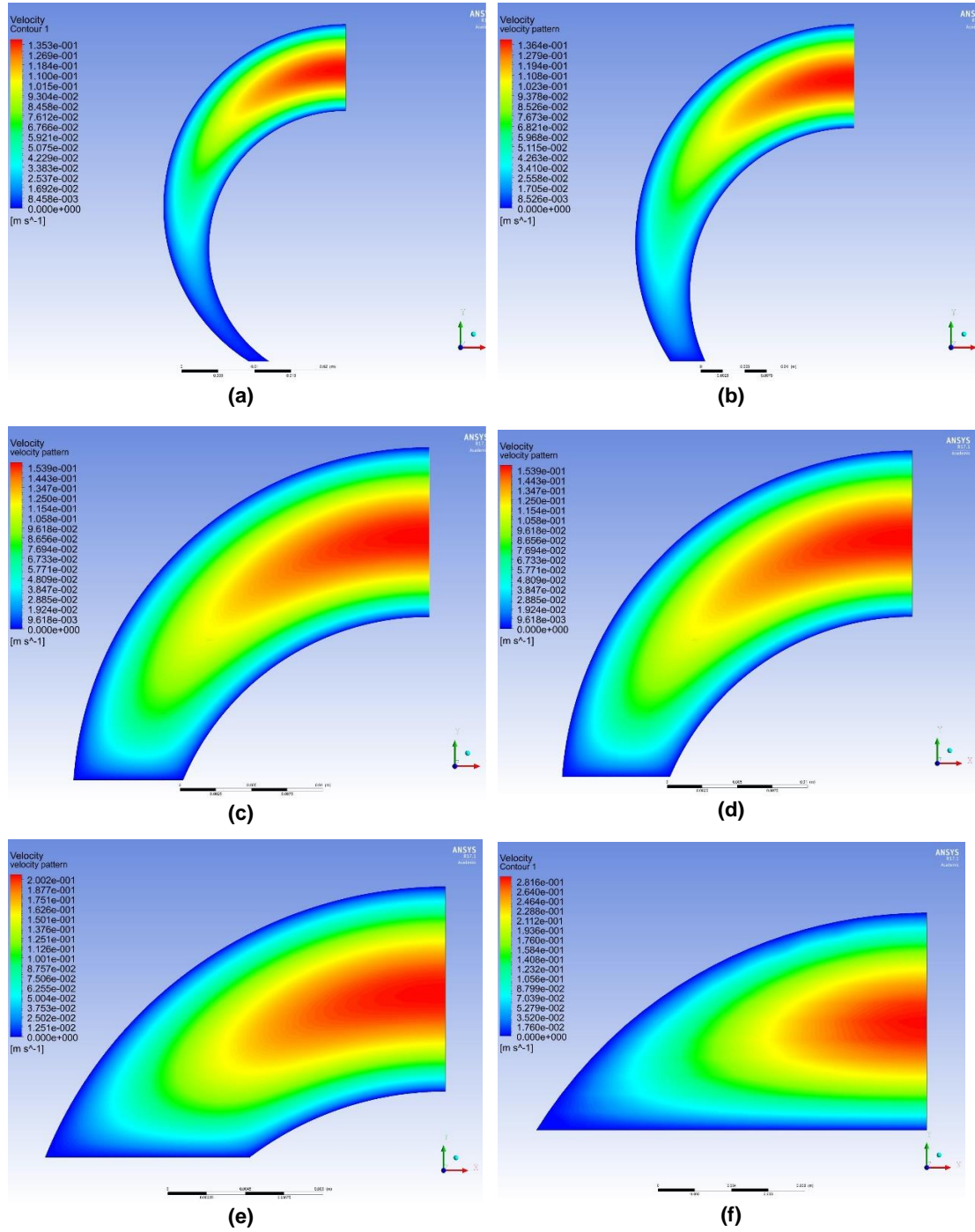


Figure E.24 Velocity Contour: a) $H_{bed} = 10\%$; b) $H_{bed} = 30\%$; c) $H_{bed} = 50\%$; d) $H_{bed} = 70\%$; e) $H_{bed} = 90\%$; f) $H_{bed} = 100\%$ ($e=0.9$, $n=1$, $\kappa = 0.75$)

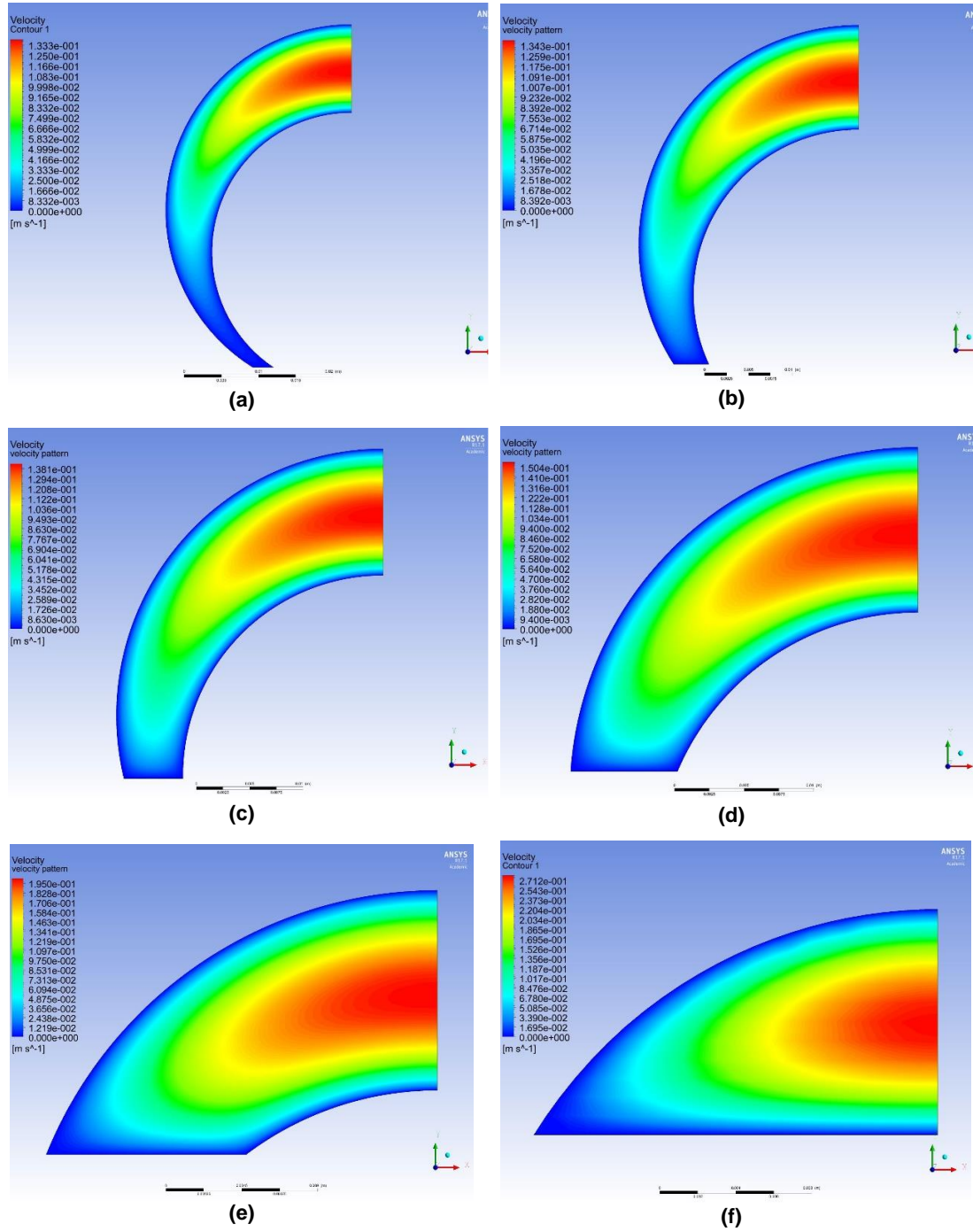


Figure E.25 Velocity Contour: a) $H_{bed} = 10\%$; b) $H_{bed} = 30\%$; c) $H_{bed} = 50\%$; d) $H_{bed} = 70\%$; e) $H_{bed} = 90\%$; f) $H_{bed} = 100\%$ ($e=0.9$, $n=0.8$, $\kappa=0.75$)

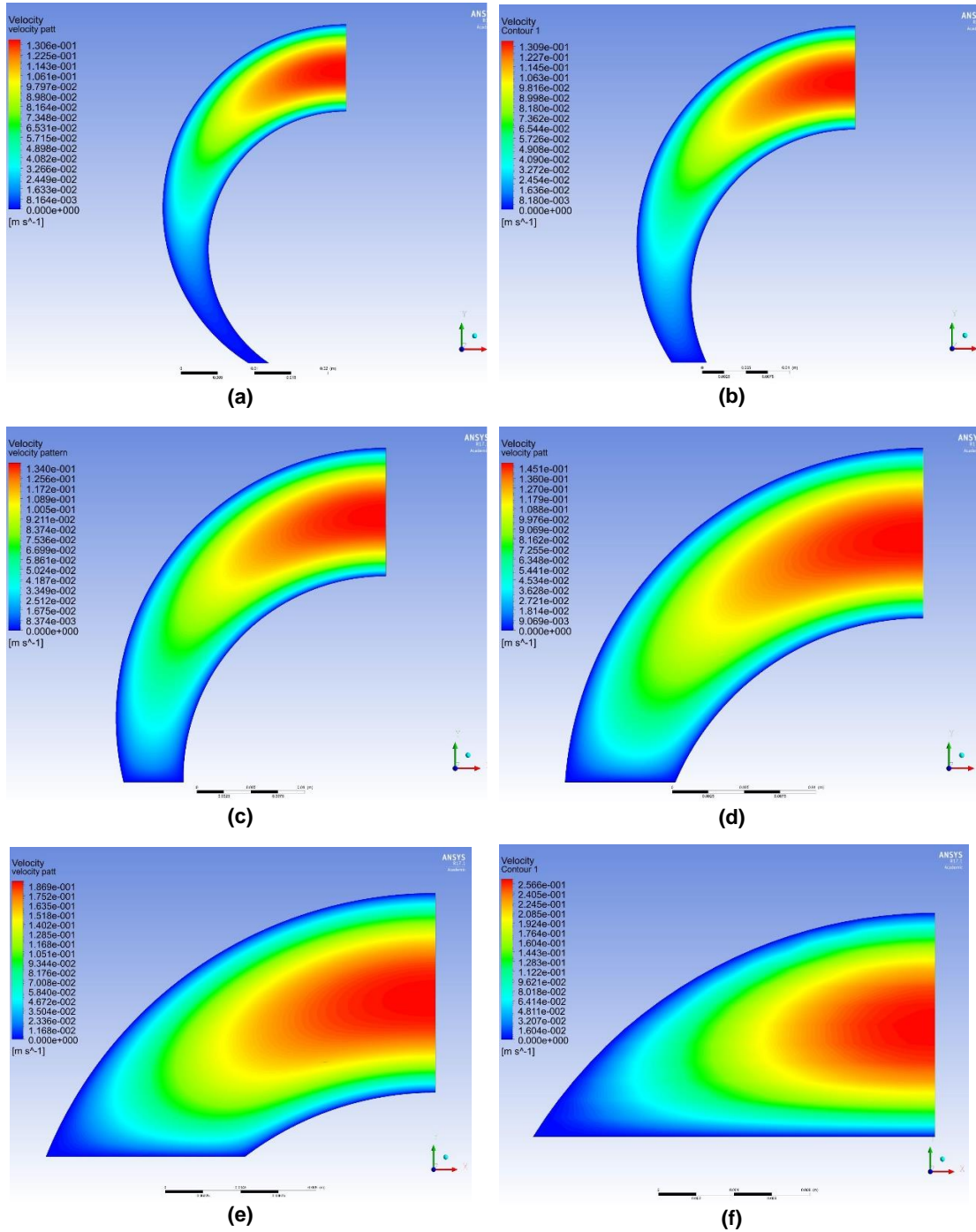


Figure E.26 Velocity Contour: a) $H_{bed} = 10\%$; b) $H_{bed} = 30\%$; c) $H_{bed} = 50\%$; d) $H_{bed} = 70\%$; e) $H_{bed} = 90\%$; f) $H_{bed} = 100\%$ ($e=0.9$, $n=0.6$, $\kappa=0.75$)

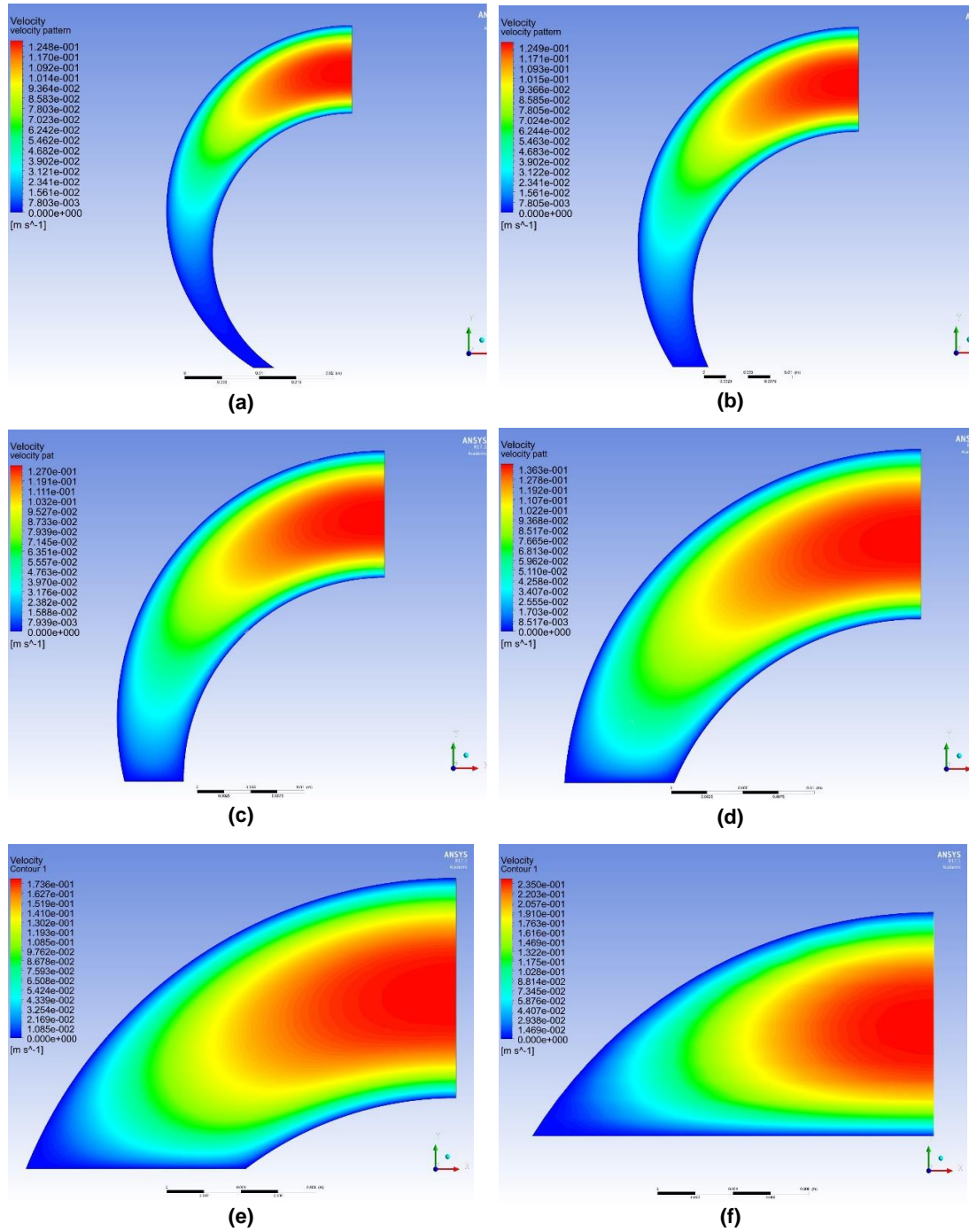


Figure E.27 Velocity Contour: a) $H_{bed} = 10\%$; b) $H_{bed} = 30\%$; c) $H_{bed} = 50\%$; d) $H_{bed} = 70\%$; e) $H_{bed} = 90\%$; f) $H_{bed} = 100\%$ ($e=0.9$, $n=0.4$, $\kappa=0.75$)

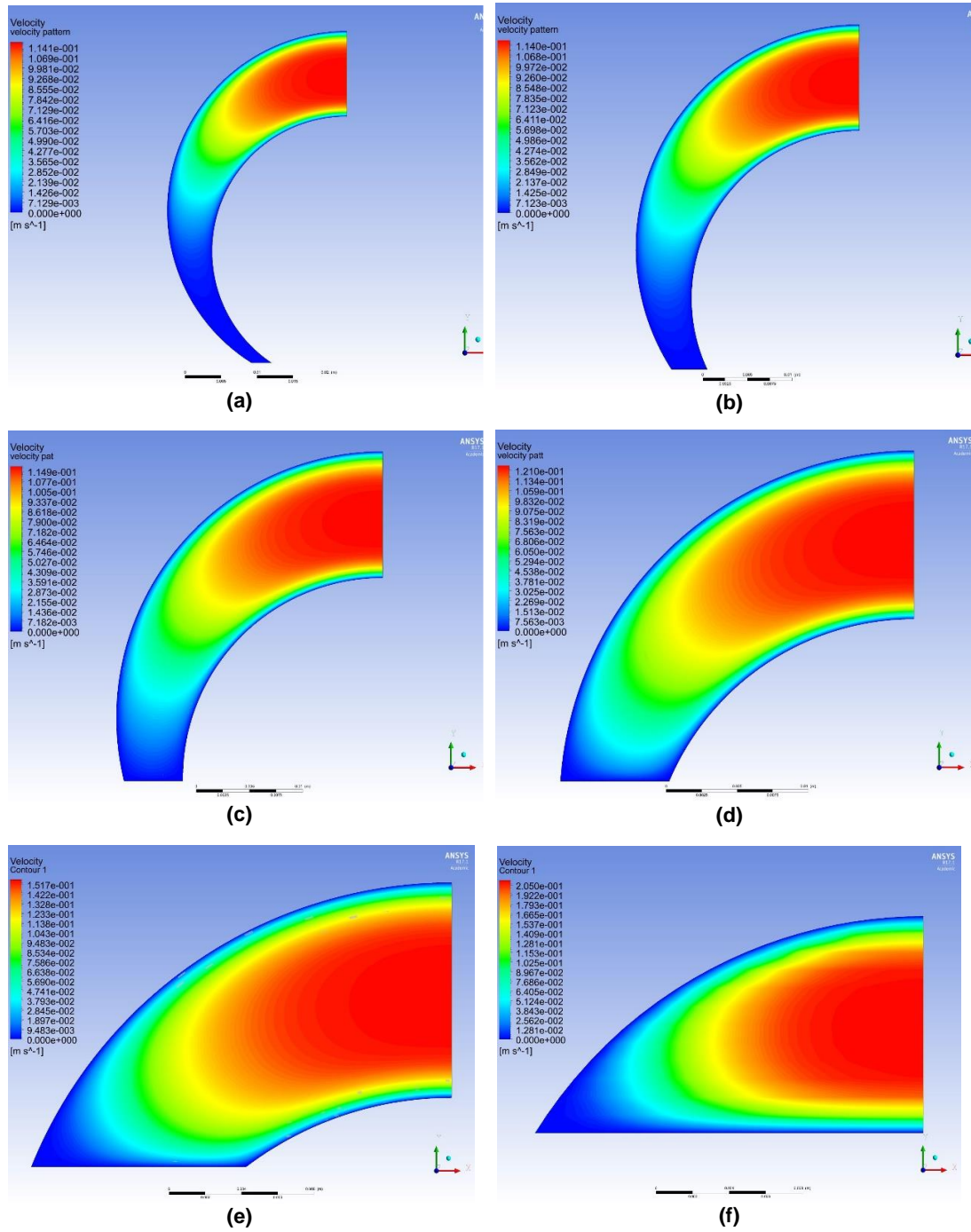


Figure E.28 Velocity Contour: a) $H_{bed} = 10\%$; b) $H_{bed} = 30\%$; c) $H_{bed} = 50\%$; d) $H_{bed} = 70\%$; e) $H_{bed} = 90\%$; f) $H_{bed} = 100\%$ ($e=0.9$, $n=0.2$, $\kappa=0.75$)

Shape Factor Figures

The shape factor function was developed for the three different diameter ratios used during this present study. Figures E-29 and E-30 illustrate the behavior of the shape factor for the remaining diameter ratios 0.75 and 0.25.

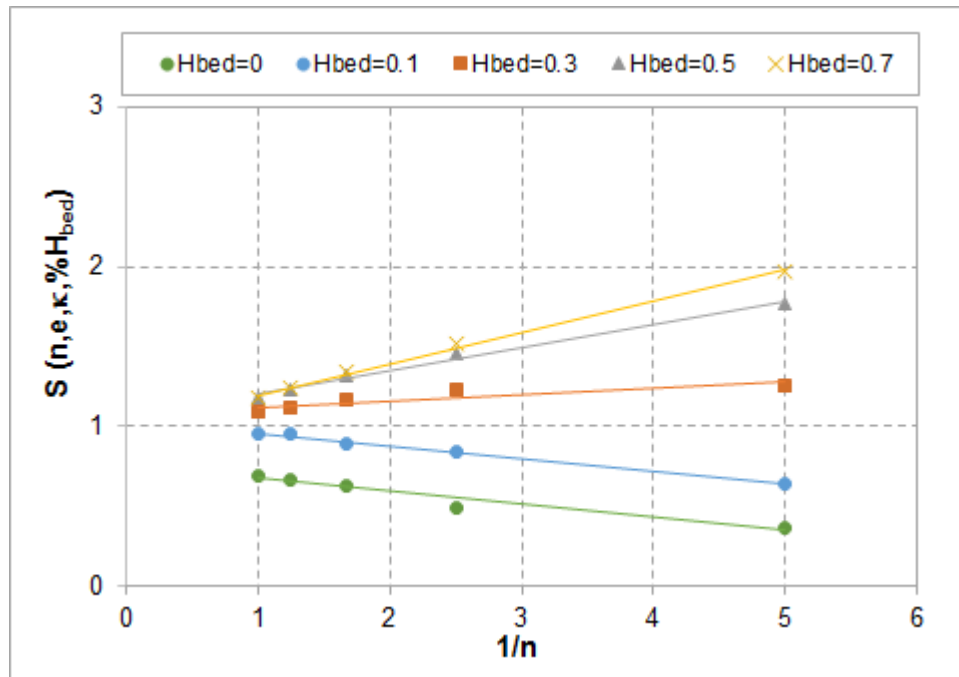


Figure E.29 Shape Factor vs. $1/n$ ($e=0.9$) for different bed heights ($\kappa=0.75$)

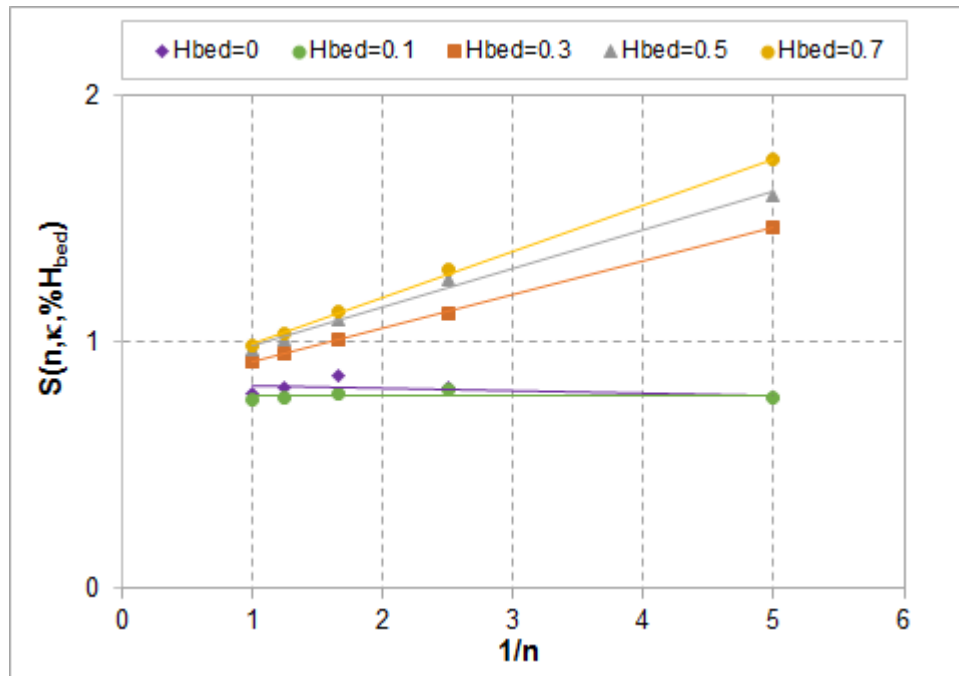


Figure E.30 Shape Factor vs. $1/n$ ($e=0.9$) for different bed heights ($\kappa=0.25$)